

Dy₂ScNbO₇: the magnetism of a mixed *B*-site
pyrochlore

Dy₂ScNbO₇: a study of the effect of a disordered *B*-site on the spin
ice magnetism typically seen in dysprosium pyrochlores

BY

MEGAN RAE RUTHERFORD, B.Sc.

A THESIS

SUBMITTED TO THE DEPARTMENT OF PHYSICS AND ASTRONOMY

AND THE SCHOOL OF GRADUATE STUDIES

OF MCMASTER UNIVERSITY

IN PARTIAL FULFILMENT OF THE REQUIREMENTS

FOR THE DEGREE OF

MASTER OF SCIENCE

© Copyright by Megan Rae Rutherford, June 2021

All Rights Reserved

Master of Science (2021)
(Physics and Astronomy)

McMaster University
Hamilton, Ontario, Canada

TITLE: Dy₂ScNbO₇: a study of the effect of a disordered *B*-site
on the spin ice magnetism typically seen in dysprosium
pyrochlores

AUTHOR: Megan Rae Rutherford
B. Sc. Honours (Physics and Chemistry)
The University of Winnipeg, Winnipeg, Canada

SUPERVISOR: Prof. Christopher Wiebe and Prof. Graeme Luke

NUMBER OF PAGES: [xiv](#), [112](#)

Abstract

The thermodynamics of disorder have been studied for hundreds of years, with physicists using entropy to quantitatively connect the macroscopic properties of a system to its microscopic multiplicity (disorder). Here, we consider the effect of disorder in magnetic materials. The pyrochlore oxides ($A_2B_2O_7$), comprised of a bipartite lattice of corner-sharing tetrahedra, have been central to the study of geometric frustration for the past several decades. Pyrochlores, in which the A -site is occupied by the magnetic cation dysprosium, tend to exhibit spin ice ordering down to low temperatures, in spite of chemical perturbations to the B -site lattice. With the motivation of this study being the investigation of how adding B -site disorder to the traditional $Dy_2B_2O_7$ form of Dy-pyrochlores, a stoichiometric mixture of Sc^{3+} and Nb^{5+} was used to synthesize Dy_2ScNbO_7 , the pyrochlore material that is central to this thesis work. We show using magnetometry, heat capacity, muon spin relaxation, and inelastic neutron scattering that the mixed B -site pyrochlore Dy_2ScNbO_7 , does not adopt the spin ice ground state. The low temperature spin dynamics are much faster than other analogous dysprosium pyrochlores, the residual entropy is significantly smaller than that predicted for a spin ice and there are low-lying crystal field excitations. These results all indicate that the B -site disorder appears to destroy the predicted Ising anisotropy of dysprosium.

*To my mother Diane, who told me that it was okay to quit and supported me
through every step so that I didn't.*

Acknowledgements

This thesis was written during the COVID-19 pandemic. In a time with so much uncertainty I am endlessly grateful to each and every person that I am about to mention. Those that took the time to hold out their hand when each of us struggled with our own battles are special.

I would like to thank my supervisor Christopher Wiebe. I do not have words to describe the ways in which you supported me throughout this degree. I can only hope that I am able to mentor with the same amount of compassion and grace that you have shown me over the past six years. I would not be the scientist that I am today had I not taken a summer research position with you during my undergrad.

Thank you to my McMaster supervisor Graeme Luke for introducing me to μ sr, and showing me how weeks at TRIUMF can fly by with Chinese food, good Netflix recommendations, and staying 3 hours ahead of the curve by refusing to adjust to the Pacific time zone. Thank you for encouraging me to follow my interests and being supportive of the ideas that I wanted to pursue. And for always laughing at my jokes.

I was fortunate to have two research groups. To my McMaster people, thank you Zach Cronkwright for being an excellent desk-mate and co-worrier. Thank you Sudarshan Sharma for being a wonderful group-mate and friend, you are the best grad student. Thank you to Evan Smith for helping me when I sprained my ankle and

anti-thank you for stealing my crutches when you sprained yours. Thanks Mathew Pula for keeping office spirits up and for reminding me whenever it was butter chicken day (Wednesday?). From Winnipeg I would like to thank Cole Mauws for teaching me everything that I knew before I started this degree, and a little bit after. Brooke Richtik deserves much more thanks than the few sentences here, but thank you for every phone call, every anxiety, every rant that you listened to. You made me feel less alone when I struggled, and were such a good friend that you will never be rid of me.

I would also like to thank the collaborators that have helped me the many experiments over the years. Whether the work made its way into this thesis or not, I am grateful for each of these experiences. Thank you to Sarah Dunsiger at TRIUMF, Adam Aczel at Oakridge National Lab, Yixi Su at FRM-II, and Chris Stock at the University of Edinburgh.

One of the minor consequences of the pandemic is that I had no office space. I must therefore thank every person who gave me a place to write and the opportunity to escape the purgatory that is Work From Home. Thank you to Tammy and Alan Bloomfield for not minding the hours I spent in their basement getting my first words down on the page. Thank you to the Ahronsons for making me one of their “designated visitors” so that I could I finish my first chapter. Thank you to Wayne for giving me the work space in which I finally finished my first draft.

I would never have finished any of this work were it not for my incredible friends. Hannah Bloomfield and Jake Blackner could probably have entire books written if I were to include every way in which they supported me over the last three years (and the four before that). I suppose “thank you” will have to do, but these words do not

capture the depth of my gratitude. I am so incredibly lucky to have both of you.

Thank you to Connor Buhariwalla for being there for me during some incredibly hard times. Irregardless of each and everything else, I am very glad to have boldly ventured to the city of Hamilton and met you.

Of course I need to thank my family. Thanks to my dad, for listening when I would talk about my research. Thank you to my Aunty Daph, who remembers her thesis writing experience and made me feel better about my own struggles. Thanks to my brother Riley, and to my cousins Brock and Jake. Thank you Darian, for all of the video chats when I was lonely and for being the only one other than my mother to come and visit me.

Finally, thank you so so much to my mom Diane. We lived together for the entirety of the pandemic and I am not sure I would have survived without her. She has read every word of this thesis, and for that alone I will be eternally grateful.

Contents

Abstract	iii
Acknowledgements	v
1 Introduction	1
1.1 Disorder and Entropy	2
1.1.1 Pauling's Entropy	5
1.2 Magnetism	8
1.2.1 The Quantum Mechanical Origin of Magnetism	8
Atomic Magnetism	9
Cooperative Magnetism	12
1.2.2 Magnetic Frustration	15
1.3 Pyrochlore Oxides	17
1.3.1 The Pyrochlore Lattice	22
1.3.2 Competing Interactions Within the Pyrochlore Lattice	27
1.4 Dysprosium Pyrochlores	30
1.4.1 Spin Ice	31
1.4.2 Project Motivation	32

2	Experimental Techniques	34
2.1	Sample Preparation	34
2.1.1	Synthesis	34
2.1.2	Crystal Growth	35
2.2	Structural Characterization	36
2.2.1	The Principles of Diffraction	37
2.2.2	X-ray Diffraction	41
2.3	Neutron Scattering	44
2.3.1	Inelastic neutron scattering	46
2.4	Magnetization measurements	47
2.4.1	DC Susceptibility	48
2.4.2	AC Susceptibility	49
2.5	Heat Capacity	53
2.6	Muon Spin Relaxation, Rotation, and Resonance	57
2.6.1	Muon Properties and Production	58
2.6.2	Experimental Setup	63
3	Bulk Property Measurements	67
3.1	Previous work	67
3.2	Bulk properties and Phase Diagram Construction	75
3.2.1	AC Susceptibility	76
	Real Susceptibility	76
	Imaginary Susceptibility	78
3.2.2	Heat Capacity	81
3.3	Muon Spin Relaxation Measurements	88

3.4	General Remarks	92
4	Preliminary Neutron Scattering and Future Work	95
4.1	Crystal Electric Field Measurements	95
4.2	Future Work	98
5	Conclusion	100

List of Figures

1.1	Proton arrangement in water ice as predicted by Pauling's ice rules	6
1.2	Antiferromagnetic and ferromagnetic ordering	14
1.3	Example of geometric frustration in 2-dimensions and 3-dimensions on a triangle and a tetrahedron	16
1.4	Periodic table showing which cations of 3+/4+ valence are known to form pyrochlores	18
1.5	The rare-earth stability field of pyrochlore oxides	20
1.6	Representation of the corner-sharing tetrahedral pyrochlore lattice.	22
1.7	Coordination of the <i>B</i> -site cation with respect to the <i>A</i> -site	24
1.8	The $\langle 100 \rangle$, $\langle 110 \rangle$, and $\langle 111 \rangle$ crystallographic directions on a cubic lattice.	25
1.9	The pyrochlore lattice from the $\langle 111 \rangle$ perspective	26
1.10	The pyrochlore lattice from the $\langle 110 \rangle$ perspective	27
1.11	Representation of Ising, XY, and Heisenberg anisotropy.	28
1.12	Ferromagnetic and Antiferromagnetic interaction on the corner-sharing tetrahedra.	29
2.1	Schematic of the floating zone crystal growth technique	36
2.2	Representation of Bragg's Law for a single set of atomic planes.	37

2.3	Geometry of the \mathbf{Q} -scattering vector via the from vector addition of incident and refracted wave vectors.	40
2.4	Geometry of an X-ray scattering experimental setup.	43
2.5	Schematic diagram of a SQUID magnetometer	52
2.6	Schematic of sample mounting for heat capacity measurements	56
2.7	Angular distribution and geometry of the positrons that result from muon decay.	62
2.8	Geometry of the positron detectors surrounding the sample in a muon relaxation experiment with no applied magnetic field	64
3.1	Image of the single crystal of $\text{Dy}_2\text{ScNbO}_7$ investigated throughout this thesis	68
3.2	Refined powder X-ray diffraction pattern that confirms a pyrochlore crystal structure.	69
3.3	DC susceptibility of polycrystalline $\text{Dy}_2\text{ScNbO}_7$ with Curie-Weiss fit.	71
3.4	Zero field cooled (ZFC) and field cooled (FC) DC susceptibility	72
3.5	Magnetic diffuse neutron scattering of $\text{Dy}_2\text{ScNbO}_7$, taken on C2 at Chalk River	74
3.6	Temperature dependence of χ' of a single crystal $\text{Dy}_2\text{ScNbO}_7$	77
3.7	Frequency dependence of χ'' of a single crystal of $\text{Dy}_2\text{ScNbO}_7$	79
3.8	Low temperature heat capacity with an external magnetic field applied along the $\langle 111 \rangle$ and $\langle 110 \rangle$ directions.	82
3.9	Phase diagram of the maximum heat capacities measured as a function of field and temperature along both the $\langle 111 \rangle$ and $\langle 110 \rangle$ crystallographic direction.	84

3.10	The heat capacity of $\text{Dy}_2\text{ScNbO}_7$ in zero applied magnetic field, plotted with analogous measurements for $\text{Dy}_2\text{Ti}_2\text{O}_7$ and $\text{Dy}_2\text{Zr}_2\text{O}_7$	85
3.11	The magnetic entropy external magnetic fields applied along the $\langle 111 \rangle$ and $\langle 110 \rangle$ directions.	87
3.12	The magnetic entropy of $\text{Dy}_2\text{ScNbO}_7$ plotted with magnetic entropies of $\text{Dy}_2\text{Ti}_2\text{O}_7$ and $\text{Dy}_2\text{Zr}_2\text{O}_7$	88
3.13	Muon spin relaxation data taken at 0.027 K and 2 K in the absence of an applied external magnetic field	90
3.14	Muon spin relaxation data taken from 3-100 K in a 4 kG external applied magnetic field.	91
4.1	Inelastic neutron spectrum of $\text{Dy}_2\text{Ti}_2\text{O}_7$ at $T = 5$ K.	97
4.2	Inelastic neutron scattering data of $^{162}\text{Dy}_2\text{ScNbO}_7$ at $T = 5$ K	98

List of Tables

1.1	Summary of the symmetry and crystallographic coordinates of the four distinct atoms in the pyrochlore lattice. The Wyckoff position is a labelling convention that relates to the space group of the lattice. . . .	23
1.2	Summary of dysprosium pyrochlores with varying B -site transition metals with their lattice parameters and transition temperatures. Experimental evidence that the dysprosium titanate [1], stannate [2], and germanate [3] all adopt the spin ice ground state exists in the literature.	33
2.1	Comparison of selected properties of μ^+ with those of the electron and proton ([4], [5]).	60

Chapter 1

Introduction

“The universe tends toward disorder.” This statement seems to appear in every thermodynamics textbook written since the 1920s in an effort to introduce the concept of entropy with respect to the second law of thermodynamics. In reality, it is a misquote from Rudolf Clausius’ initial work developing the Laws of Thermodynamics. In his book entitled “The Mechanical Theory of Heat,” Clausius stated that the “entropy of the universe tends to a maximum,” in an effort to summarize the second of these laws [6]. In any study involving disorder, the entropy of the system of interest is key in relating the microscopic state of the disordered system to the macroscopic thermodynamic properties that we can experimentally measure and vice versa.

Clausius’ earliest description of entropy was as an “equivalence-value” to describe the passage of heat Q from temperature T_1 to T_2 , giving the first mathematical description of entropy S , or the equivalence value to be:

$$\Delta S = Q \left(\frac{1}{T_2} - \frac{1}{T_1} \right). \quad (1.0.1)$$

Clausius expanded from this initial definition to include the path dependence of the heat transferred by defining the heat exchanged as an inexact differential:

$$\Delta S(a, b) = \int_a^b \frac{\delta Q_{rev}}{T}, \quad (1.0.2)$$

where a and b are arbitrary starting and end points and Q_{rev} is the heat transferred in a reversible process. There are many different ways to express the second law of thermodynamics, one of them being:

$$\Delta S = \int \frac{\delta Q_{rev}}{T} \geq 0. \quad (1.0.3)$$

A detailed derivation of the second law from Equation 1.0.2 can be found in reference [7]. All of these are to say that, for an isolated system, the entropy is always increasing. If the system is not isolated, then the sum of the entropy of the system and its surroundings is increasing [8], giving us another expression for the second law that states:

$$\Delta S_{universe} = \Delta S_{system} + \Delta S_{surroundings} \geq 0. \quad (1.0.4)$$

The inclusion of the entropy being equal to zero, rather than solely greater than zero, is in reference to the third law of thermodynamics, which is elaborated upon in Section 1.1.1.

1.1 Disorder and Entropy

Hitherto, the physical meaning of entropy has been somewhat nebulous. At the beginning of Chapter One, entropy was defined as the measure of a system's thermal

energy per unit temperature that is unavailable for doing useful work (as seen in Equation 1.0.2). The idea of entropy is often introduced as the amount of “disorder,” or “randomness” in a system. While this is a vague description, particularly as we are currently without any definition of “randomness,” or “disorder,” it can be useful in qualitatively predicting whether a process will be spontaneous or not. In fact, many introductory thermodynamics books describe entropy as the state function that predicts the “direction of natural, or spontaneous, change” [8].

In 1877, Ludwig Boltzmann was able to develop a definition of entropy that served to connect the macroscopic observations that had been made to the microscopic state of a system. This statistical mechanical description of entropy lead to the expression:

$$S = k_B \ln \Omega, \quad (1.1.1)$$

where k_B is the Boltzmann constant ($k_B = 1.380662 \times 10^{-23} \text{J}\cdot\text{K}^{-1}$), and Ω is the multiplicity, or the microscopic degrees of freedom of a system [9]. This expression is historically the foundation of statistical mechanics. Combining some of these different descriptions of entropy, we arrive at the idea that a system will preferentially tend towards their state(s) of maximum multiplicity. Simply put, the multiplicity of events is the total number of ways in which different outcomes can occur [9]. For example, if there are N states that can adopt one of two outcomes (spin up/spin down, heads/tails, success/failure), then the multiplicity would be given by:

$$\Omega(n, N) = \binom{N}{n} = \frac{N!}{n!(N-n)!}, \quad (1.1.2)$$

where n is the number of states that adopted one outcome, and $(N-n)$ is the number

of states which adopted the other. We often think of multiplicity in terms of probabilities, achieved by dividing Ω by the total number of states. The mathematical treatment of multiplicity as it pertains to different types of probabilities is elaborated upon in references [9], and [10].

We can also describe the entropy in terms of probabilities:

$$\frac{S}{k_B} = - \sum_{i=1}^t p_i \ln p_i, \quad (1.1.3)$$

where p_i is the probability of event i occurring. It can be shown that this is equivalent to equation 1.1.1 by writing out the multiplicity as

$$\Omega = \frac{N!}{n_1!n_2! \cdots n_t!}, \quad (1.1.4)$$

where N is the total number of objects with t categories, of which n_i objects in each category are indistinguishable from each other, but are distinguishable from the the objects in the other $t-1$ categories. Using Stirling's approximation ($x! = (x/e)^x$), and some algebra gives:

$$\frac{1}{N} \ln \Omega = - \sum_{i=1}^t p_i \ln p_i = \frac{S_N}{Nk_B}, \quad (1.1.5)$$

with S_N being the entropy per object (event). Boltzmann's constant allows for the conversion of energy from microscopic (per atom) scales to macroscopic (per mole) scales. This is accomplished using the relationship $R = \mathcal{N}k_B$ (R defines the ideal gas constant and \mathcal{N} is Avogadro's constant).

The relevance of this in-depth explanation and derivation of the probability dependence of entropy lies in our overarching goal of mathematically defining “randomness.” The probability distribution that will give a maximum multiplicity and therefore a

maximum entropy is that in which each possible state occurs with equal probability. Specifically, the multiplicity is greatest with a random probability distribution. We therefore arrive at a mathematical description of the initial statement of “The entropy of the universe tends to a maximum;” that is, the processes will occur spontaneously in a manner such that their entropy is maximized thereby favouring an increase in disorder.

1.1.1 Pauling’s Entropy

We can intuit many different examples in which a system tends towards disorder in our daily lives - wood burns, popcorn pops, and sugar dissolves in water. On the microscopic scale, the entropy of a system is not so obvious and requires careful consideration of the degrees of freedom and use of Boltzmann’s equation. One famous success of the experimental entropy being used to elucidate the ordering of a system was in water ice.

In the 1930s, many scientists were investigating the entropy of substances down to low temperatures in order to further their understanding of various crystalline systems. Linus Pauling contributed to this in his study of water ice [11]. His intention was to determine the nature of how water molecules order in its crystalline form. While it was known from X-ray studies that oxygen atoms tetrahedrally coordinate to four other oxygen atoms in an open lattice, the position of the hydrogen atoms remained a mystery. Pauling was well aware of hydrogen bonding and postulated that the hydrogens would lie between the oxygen atoms. The question remains - where along these oxygen-oxygen bonds does the hydrogen atom sit? Is it equidistant between the two oxygens? Is there some preference for the hydrogen to sit closer to

one atom than another?

To accomplish this, Pauling made several assumptions, one being that there are two hydrogens that are bonded to the central oxygen atom, forming a water molecule. The second assumption was that each water molecule is oriented so that these two “bonded” hydrogens point towards two of the other four oxygen atoms that surround the central oxygen atoms. He then assumed that hydrogen bonds were formed between these hydrogens and the surrounding oxygens (a schematic of this can be seen in Figure 1.1 below). From these assumptions, it follows that there are many different configurations in which an ice crystal can exist. One of the key findings of Pauling’s investigation was that upon cooling, water molecules adopt a crystal structure in one of these configurations. However, the configuration (whichever it may be) does not turn over into a perfect crystal completely free of disorder, making this one of the first experimental realizations of residual entropy.

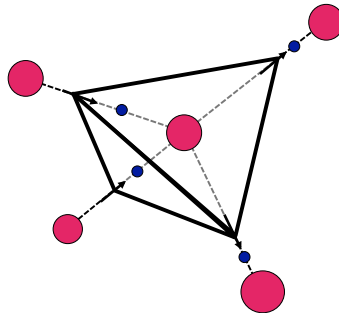


Figure 1.1: Hydrogen atoms (blue circles) arranged about oxygen atoms (red circles) in ice. Two hydrogen atoms are bonded (they are closer) to the central oxygen atom while two of them are hydrogen bonded (they are further) to the central atom within a tetrahedral arrangement of oxygens. Figure adapted from Gardner *et al.* [12].

In order to determine which of the many available configurations the water molecules adopt in its crystal form, Pauling calculated the predicted entropy of some of the possible states using statistical mechanics. The multiplicity of the system comes from

the possible orientations of the hydrogens around a central oxygen atom. The multiplicity, Ω , of the system was reasoned via the following logic: If we initially ignore the assumptions made above, there are 2^{2N} configurations where a hydrogen exists between adjacent oxygens. There are then sixteen possible ways for 4 H atoms to occupy 4 possible sites (4^4). However, taking the first assumption into account (that there are two “short” and two “long” hydrogen bonds), there are six possible ways to orient the hydrogens given this constraint giving $6/16 = 3/8$ possible configurations. The multiplicity is therefore given by:

$$\Omega = 2^{2N} \left(\frac{3}{8}\right)^N = \left(\frac{3}{2}\right)^N, \quad (1.1.6)$$

which gives a residual entropy of water ice to be:

$$S = R \ln \left(\frac{3}{2}\right). \quad (1.1.7)$$

This was then confirmed via low temperature heat capacity measurements and can be found in Pauling’s seminal work [11].

While we are discussing residual entropy, this is not in violation of the third law of thermodynamics. The third law states that as the temperature of a perfect crystalline solid goes to absolute zero, the entropy of that solid will also go to zero [8],[9]. The key phrase in this definition is that this law refers to a “perfect crystalline solid.” In water ice, the residual entropy arises due to the disorder of the system originating from the equivalent, but distinct, orientations of hydrogen bond lengths surrounding a central oxygen atom. That is, that the entropy of crystalline ice does not equal zero when the temperature is zero, but this is not in violation of the third law as it is not

a perfect crystalline solid without any disorder.

1.2 Magnetism

In a study of how a disordered crystalline lattice affects the magnetic properties of the system, it is prudent to give a description of this phenomenon in general, before moving into more nuanced aspects of magnetism directly relevant to this thesis. Humans have known of the existence of magnetism since antiquity, where ancient Greek philosophers wrote on the attraction of iron to lodestone [13]. While a great deal of progress had been made regarding the properties of magnetic fields, the atomic origin of magnetism in materials was impossible to understand until the paradigm shifting discovery of quantum mechanics in the early 20th century. The origin of magnetism in materials is inherently quantum mechanical, and the application of the tools developed through the theory of quantum physics research resulted in a great deal of forward progress in the study and understanding of magnetic materials [14], [15].

1.2.1 The Quantum Mechanical Origin of Magnetism

Maxwell's equations define classical electromagnetism, and specifically the way in which a moving electric charge produces a magnetic field [16]. The orbital contribution to magnetism due to the movement of an electron about its nucleus in an atom can be explained as a consequence of this property (although the manifestation departs significantly from this simple starting point).

Atomic Magnetism

Consider an electron, with elementary charge e ($e = 1.602 \times 10^{19}$ C), that orbits a much heavier nucleus to give rise to an orbital angular momentum \mathbf{L} . The angular momentum results in a magnetic moment $\boldsymbol{\mu}_L$, given by:

$$\boldsymbol{\mu}_L = \frac{-e}{2m_e} \mathbf{L}, \quad (1.2.1)$$

where m_e is the mass of an electron, and the magnitude of \mathbf{L} is given by:

$$|\mathbf{L}| = \sqrt{l(l+1)}\hbar \quad \text{and} \quad l = 0, 1, \dots, n-1. \quad (1.2.2)$$

With n , and l being quantum numbers.

In 1922, the Stern-Gerlach experiment showed a departure from classical mechanics when Otto Stern and Walther Gerlach determined that there was an atomic source of angular momentum that was not due to its orbit about the nucleus [17]. Rather, there was some component of the angular momentum that was intrinsic to the electron, and behaved as if the particle itself was rotating about some axis. For this reason, Stern and Gerlach coined the term “spin,” denoted as \mathbf{S} , to describe this quantity. While spin has no classical analogue, it can be defined similarly to the orbital angular momentum \mathbf{L} above, with a moment arising due to the spin given by:

$$\boldsymbol{\mu}_S = \frac{-e}{2m_e} \mathbf{S}, \quad (1.2.3)$$

where m_e is the mass of an electron and the magnitude of \mathbf{S} is given by:

$$|\mathbf{S}| = \sqrt{s(s+1)}\hbar \quad \text{and} \quad s = 1/2. \quad (1.2.4)$$

The quantum number $s = 1/2$ given above is a property inherent to the electron due to its nature as a fermionic particle. The final two quantum numbers that are used to denote the quantization of both the orbital and spin angular momenta are m_l , and m_s respectively. These quantum numbers take on the values $m_l = -l, -l+1, \dots, l-1, l$, and $m_s = -s, -s+1, \dots, s-1, (s = -1/2, \text{ and } +1/2 \text{ for the electron})$.

The total angular momentum is given by summing the orbital and spin angular momenta:

$$\mathbf{J} = \mathbf{L} + \mathbf{S}, \quad (1.2.5)$$

where the magnitude of \mathbf{J} is given by:

$$J = L \pm S, \quad (1.2.6)$$

which will minimize energy in the following way:

$$J = \begin{cases} L + S, & \text{if valence shell } > \text{ half full} \\ |L - S|, & \text{valence shell } < \text{ half full} \end{cases} \quad (1.2.7)$$

Putting this all together, we have an expression for the effective magnetic moment of the atom:

$$\mu_{eff} = g\sqrt{j(j+1)}\mu_B, \quad (1.2.8)$$

where μ_B is the Bohr magneton, which is calculated according to:

$$\mu_B = \frac{e\hbar}{2m_e} = 5.788 \times 10^{-5} \text{eV/T} = 9.27 \times 10^{-27} \text{J/T}, \quad (1.2.9)$$

and g is the Landé g factor:

$$g = 1 + \frac{j(j+1) + s(s+1) - l(l+1)}{2j(j+1)}. \quad (1.2.10)$$

The g -factor is a first order perturbation term that relates the magnetic moment to its corresponding generating angular momentum. A more detailed derivation and explanation of this can be found in Griffiths [18].

It is important to note that, while the nucleus of the atom possess a magnetic moment of its own, the magnitude of the moment is inversely proportional to the mass of the particle. Therefore, the hydrogen nucleus, with a mass ≈ 1800 times that of the electron, has a moment that in most cases is negligible in comparison to that of the electron. As such, we can consider the atomic magnetic moment to be a result of the electronic angular momenta.

The number of valence electrons that orbit the nucleus is important to the type of magnetism that an atom of any element will exhibit. From the Pauli exclusion principle - where no two electrons can have the same set of identical n , l , m_l , and m_s quantum numbers, we know that no two electrons can spatially occupy the same orbital if they have the same spin. Additionally, from Hund's first rule, which states that, "the state with the highest spin will have the lowest energy," we know that each available orbital in a given subshell will be occupied by one electron before any orbital is occupied by two electrons. It then follows that, for a "pair" of electrons,

where electrons that occupy the same spatial coordinates will be anti-parallel, and their net moment will cancel. A detailed description of Hund’s rules, and their uses can be found in reference [18]. A net magnetic moment will arise when the system has unpaired valence electrons and is referred to as paramagnetic. In contrast, if all valence electrons are paired, the system is referred to as diamagnetic. In an applied magnetic field diamagnetic materials will produce an internal field in the direction opposite to the applied field. This internal field vanishes as the applied field approaches zero. Paramagnetic materials will respond to a applied magnetic field by aligning along the field direction with net magnetization persisting as the applied field approaches zero.

Cooperative Magnetism

Where the magnetic moment of an isolated atom was the focus of the above section, we now shift our attention to bulk magnetism, or how a large collection of magnetic ions will behave within a solid. For convenience, the total angular momentum of a magnetic ion will now be referred to as its “spin.” The magnetism that is observed in a crystalline system (the object of this thesis) cannot be explained by considering a collection of isolated magnetic cations, but rather by determining the way in which their magnetic moments interact with each other. It is these interactions that describe the cooperative behaviour of magnetic moments in a solid.

From the quantum mechanical description of spin given above, we can effectively treat the magnetic moment of an atom as a magnetic dipole. Therefore, within a solid, there will be a large collection of dipoles interacting with one another. These

dipole-dipole interactions can be described by once again, turning to classical electromagnetism. While we may naively expect that bulk magnetization is a result of these interaction, this is not the case. The dipolar interaction energy can be determined from the following equation:

$$U = \frac{\mu_0}{4\pi r_{ij}^3} [\mathbf{m}_i \cdot \mathbf{m}_j - 3(\mathbf{m}_i \cdot \mathbf{r}_{ij})(\mathbf{m}_j \cdot \mathbf{r}_{ij})], \quad (1.2.11)$$

where \mathbf{m}_i and \mathbf{m}_j are magnetic dipole vectors, and \mathbf{r}_{ij} is vector connecting the two dipoles via the shortest possible path. It becomes obvious that, since $U \propto 1/r_{ij}^3$, dipolar interactions are relatively weak, but are long-range in comparison to other interactions that are more predominate within the system.

While dipolar interactions can be described through classical mechanics, the other dominant type of magnetic interaction that occurs between magnetic moments is the quantum mechanical exchange interaction. As electrons are indistinguishable particles, the wavefunction of the system must obey certain symmetries when we exchange an electron in one state with another [18]. As spin 1/2 particles, the wavefunctions of electrons are antisymmetric with respect to exchange and therefore cannot occupy the same state. Cooperative paramagnetism arises due to the net effect of exchange interactions between nearby atomic orbitals. The exchange interaction energy (E) can be seen in the following equation:

$$E = -2J_{ex}(\mathbf{S}_i \cdot \mathbf{S}_j), \quad (1.2.12)$$

where \mathbf{S}_i and \mathbf{S}_j are the values of individual spins, and J_{ex} is the exchange integral

given by:

$$J_{ex} = \frac{e^2}{4\pi\epsilon_0} \int \psi_A^*(\mathbf{r}_i)\psi_B^*(\mathbf{r}_j) \left(\frac{1}{r_{AB}} + \frac{1}{r_{ij}} - \frac{1}{r_{Aj}} - \frac{1}{r_{Bi}} \right) \psi_A(\mathbf{r}_j)\psi_B(\mathbf{r}_i) d\mathbf{r}_i d\mathbf{r}_j \quad (1.2.13)$$

with e being the elementary charge, and ϵ_0 being the permittivity of free space. The subscripts A and B label two distinct atoms, while i and j label two individual electrons. The radial position of each electron is given by $\mathbf{r}_{i/j}$ and the distance between each of the four particles is given by $r_{A/B,i/j}$ with the subscript labelling which of the particles are considered. Finally, ψ and ψ^* denote the real and imaginary wavefunctions of the atoms with respect to electron exchange respectively. In equation 1.2.12, the $-2J_{ex}$ corresponds to the exchange energy. From this, we can deduce that if the exchange integral J_{ex} , is negative, an antiparallel spin arrangement (seen on the left in Figure 1.2) will be favoured and antiferromagnetic order will occur. On the other hand, if J_{ex} , is positive, a parallel spin arrangement (seen on the right in Figure 1.2) will be favoured and ferromagnetic order will occur.

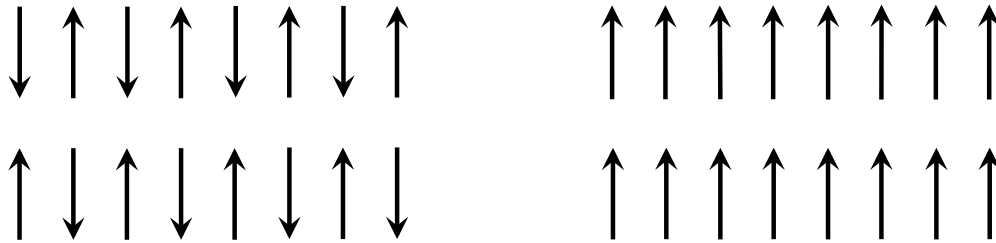


Figure 1.2: Magnetic moments ordered with antiparallel alignment i.e. antiferromagnetically (left) and with parallel alignment i.e. ferromagnetically (right).

As mentioned above, there are many different mechanisms by which exchange can occur, (anti)ferromagnetism being one of the most straightforward. Here, adjacent magnetic species have overlapping orbitals via what is called “direct exchange.” Also

worth mentioning is superexchange, in which exchange occurs via an intermediate ions. More details regarding different types of exchange can be found in references [14] and [19].

A magnetically ordered state is a stable state of the system where some repeating spin structure (or non-macroscopic set of structures) minimizes the energy from the above magnetic terms.

1.2.2 Magnetic Frustration

Some materials fail to adopt a magnetically ordered state. A subset of these materials exhibit a phenomenon known as “frustration.” One of several definitions of magnetic frustration is that the Hamiltonian of the system has competing magnetic interactions which contribute to the energy in a way that the energy of interactions cannot be minimized simultaneously.

While frustration can originate from various constraints present within a magnetic system, the focus of this thesis is geometrical frustration. For geometrical frustration, the local constraints cannot be simultaneously satisfied due to the geometry of the crystalline lattice. The simplest way to describe this by considering a two-dimensional triangular model with antiferromagnetic exchange interactions. This can be seen in Figure 1.3. If the spin occupying one lattice point is spin up, and the spin on the other lattice point is spin down, antiferromagnetic interactions with respect to either lattice point cannot be simultaneously satisfied at the third lattice site.

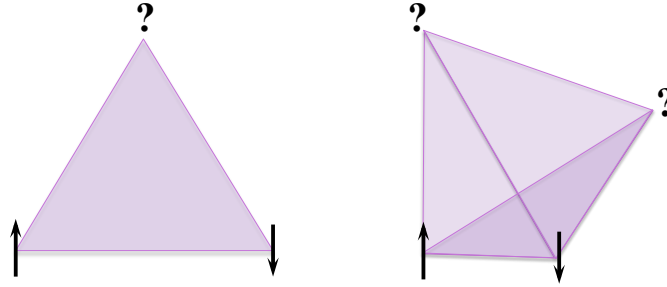


Figure 1.3: Antiferromagnetically coupled spins are placed on a two-dimensional triangular lattice (left), and a three-dimensional tetrahedral lattice (right). In 2D, nearest neighbour antiferromagnetic interactions at the third lattice point cannot be simultaneously satisfied and frustration occurs. The same can be seen in 3D where there are now two frustrated lattice points.

This can easily be extended to a three-dimensional model system of a tetrahedron with antiferromagnetic interactions. If spins are antiparallel at two of the four possible lattice sites, the remaining two lattice sites (as seen on the right of Figure 1.3 above) cannot have a spin that satisfies both of the existing exchange interactions. The realization of geometric frustration is often seen in materials with crystalline lattices containing triangular motifs, a famous example of which is the pyrochlore lattice, which will be described in detail in Section 1.3.

There are several reasons as to why frustrated systems have garnered so much attention in the condensed matter community over the past several decades. Since some of these systems tend to have difficulty ordering in conventional ways, energetic compromises are often made to achieve the lowest energy ground state. In classical models of highly frustrated materials, the ground state is macroscopically degenerate. This degeneracy does not (always) result from symmetry, but rather arises accidentally, due to degeneracies in the ground state spin orientation [20]. These energetic compromises can result in the absence of long order as well as a reduced ordered

moment in frustrated systems. In fact, the primary motivation of studying magnetic frustration is that, as the system attempts to minimize its energy but is unable to simultaneously satisfy competing interactions, exotic ground states have been known to emerge.

Several of these so-called “exotic” ground states have been studied in depth for the last several decades and exhibit a wealth of interesting physics. For example, spin glasses are materials which, at low temperatures, adopt a random orientation of spins as they are “frozen out.” Spin glasses are named for the analogy of random spin orientation to silicon dioxide chemical bonds that vary randomly throughout silicate glasses [21]. Another interesting (and most relevant to this thesis work) possible ground state spin configuration is that of the spin ice. This class of materials will be discussed at length in Section 1.4.1. Finally, the focus of a great deal of research regarding frustrated magnetism is the possible realization of the quantum spin liquid state, where the system remains dynamic down to the lowest temperatures without ordering [22].

1.3 Pyrochlore Oxides

The pyrochlore lattice is isostructural to the naturally occurring mineral pyrochlore $(\text{Na,Ca})_2\text{Nb}_2\text{O}_6(\text{OH,F})$, for which it is named. Pyrochlore oxides have been the canonical structure in which three-dimensional geometric frustration has been observed and studied since the 1950s [23]. With the chemical formula $\text{A}_2\text{B}_2\text{O}_7$, the pyrochlore crystal structure consists of two interpenetrating, corner-sharing, tetrahedral lattices that are referred to as the “*A*-site,” and the “*B*-site.” Aside from the tetrahedral motif of its crystal structure, the appeal of studying materials that adopt the pyrochlore

structure lies in the wide variety of different element combinations that are able to sit on the *A*- and *B*-sites. Typically, the *A*-site is occupied by a trivalent rare-earth cation, and the *B*-site is occupied by a tetravalent transition metal - referred to as the (3+,4+)-type pyrochlores. It is possible however, to have (2+,5+)-type pyrochlores but discussion of this charge distribution is outside of the scope of this thesis and from here on discussion will focus solely on (3+,4+)-pyrochlores. It is typical in magnetic studies for the *A*-site to be occupied by a magnetic cation, and a non-magnetic cation to occupy the *B*-site. Elements that are commonly combined to form pyrochlores are shown in Figure 1.4 below.

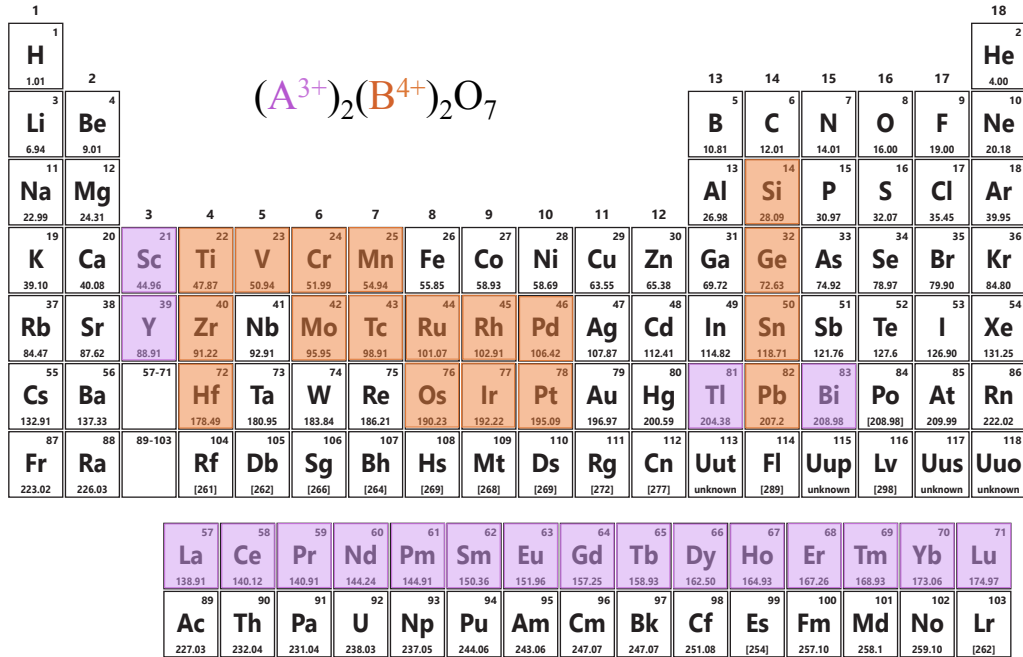


Figure 1.4: Schematic of the periodic table of elements highlighting cations of 3+ (purple)/4+ (orange) valence that are known to form the pyrochlore structure in various possible combinations. *Figure adapted with permission from Hallas et al. [3].*

From the above figure, there is a large number of possible pyrochlore candidates from the permutations of elements that can be combined to achieve charge neutrality.

However, not every possible combination of elements indicated above will adopt the pyrochlore structure. Typically, the factor of stability of pyrochlore oxides is the relative ionic radii of the A - and B -sites,

$$RR = \frac{r_A^{3+}}{r_B^{4+}}. \quad (1.3.1)$$

A pyrochlore lattice will typically form where $1.38 < RR < 1.71$ [12]. The compositional stability of pyrochlores lends very well to systematic studies of materials in which the effects of changing one element in the pyrochlore lattice can be investigated. This provides a means to probe the effects of lattice size, magnetic moment, anisotropy, etc, on different pyrochlore systems. The pyrochlore field of stability can be seen in Figure 1.5, and is extended as high pressure synthesis techniques are used [24].

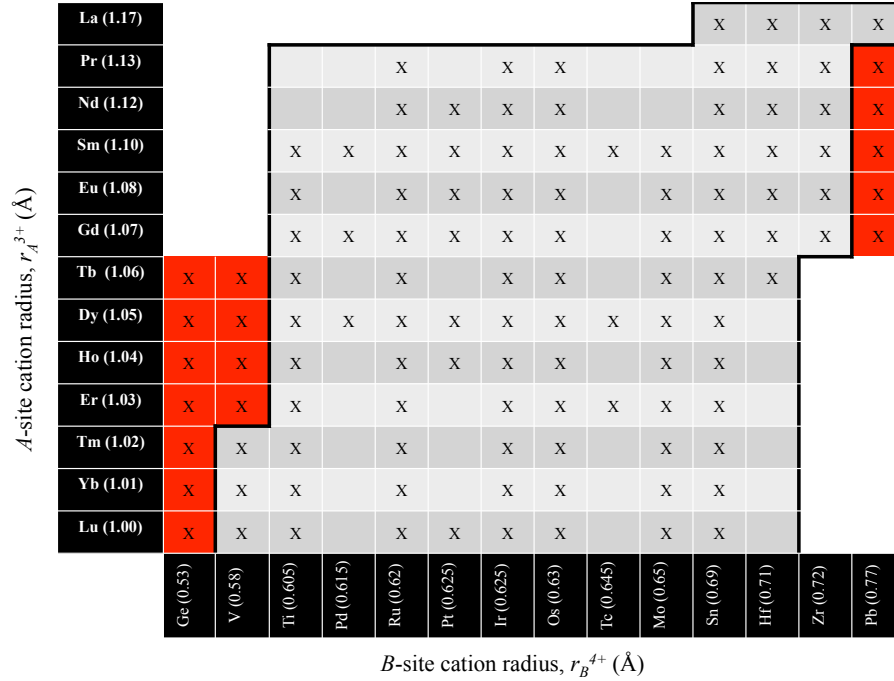


Figure 1.5: The rare-earth stability field of pyrochlore oxides. The X’s denote that the combination of the rare-earth cation on the y-axis with the transition metal on the x-axis adopts the pyrochlore lattice that have been reported in the literature [12]. The region of stability is indicated by the black line, while species prepared under high pressure conditions are highlighted in red. *Figure adapted with permission from Hallas et al. [3].*

While the ratio of ionic radii is a good guiding factor as to whether or not a material will adopt the pyrochlore structure, it is not strictly obeyed. This is particularly true near the upper limit of RR , where some materials technically lie within the field of stability, but may form a metastable structure, or not adopt the pyrochlore structure at all.

The corner sharing tetrahedral network of the pyrochlore lattice allows for a high degree of frustration. This has been studied systematically over the last several decades and been fruitful in the realization of many different magnetic ground states. These include long range ordered magnetic states [25], amorphous spin glasses [26],

[27], and short range ordered states including the spin ice [28], [29], [30], [31], as well as spin liquid [32],[33] states where there is no short or long range order.

Another avenue that is available in the expansion of the pyrochlore family is to add chemical disorder as an additional degree of freedom. There have been few disordered pyrochlores that have successfully been synthesized and even fewer that are well understood. Some ways in which disorder has been applied to the pyrochlore lattice include oxygen non-stoichiometry, stuffing (where more of the magnetic A -site cation is “stuffed” onto the non-magnetic B -site), and solid solutions (a family of materials in which one site will be split into a range of compositions of the form X_aY_{1-a} but still adopt the same structure). Another type of disorder is charge disorder. An example is the disordered A -site pyrochlores that take the form NaXY_2F_7 . These materials are not oxides, and have $X = \text{Ca}$ or Sr and $Y = \text{Fe}$ or Mn [34]. More relevant to this thesis work are pyrochlores with a stoichiometrically disordered B -site. Where pyrochlores are usually of the form $(\text{A}^{3+})_2(\text{B}^{4+})_2\text{O}_7$, one can theoretically split the B -site so that there is a 1:1 stoichiometric mixture of a 3+ and 5+ charged cation - where the charge averages to 4+ to maintain charge neutrality and the average radius still gives a ratio that lies within the pyrochlore field of stability. The disordered B -site pyrochlore structure is difficult to achieve as there is a tendency to adopt the defect fluorite structure (in which there is not a well-defined A - or B -site). To date, some of the only successfully synthesized pyrochlores with a disordered B -site are $\text{RE}_2\text{ScNbO}_7$, where $\text{RE} = \text{rare-earth element}$ (the subject of this work, following the work of Zouari *et al.* [35]), and $\text{RE}_2\text{GaSbO}_7$ [36], [37].

1.3.1 The Pyrochlore Lattice

It is important to pay special attention to several different features of the pyrochlore lattice in order to properly investigate the effect of a disordered B -site sublattice on the low temperature physics of pyrochlore oxides. It is not enough to merely consider the sublattice containing magnetic cations. We must consider the crystal lattice from several different perspectives when investigating the pyrochlore lattice. As mentioned above, pyrochlores are comprised of a bipartite lattice where each network of corner shared tetrahedra adopt a face centered cubic structure. Pyrochlores belong to the space group $Fd\bar{3}m$ [38], and have four distinct atoms per unit cell. With the chemical formula $A_2B_2O_6O'$ these atoms are labelled as A (for the purposes of this study is a trivalent lanthanide), B (a tetravalent transition metal), and two distinct oxygen environments denoted as O and O' (which can be seen in Figure 1.6 below).

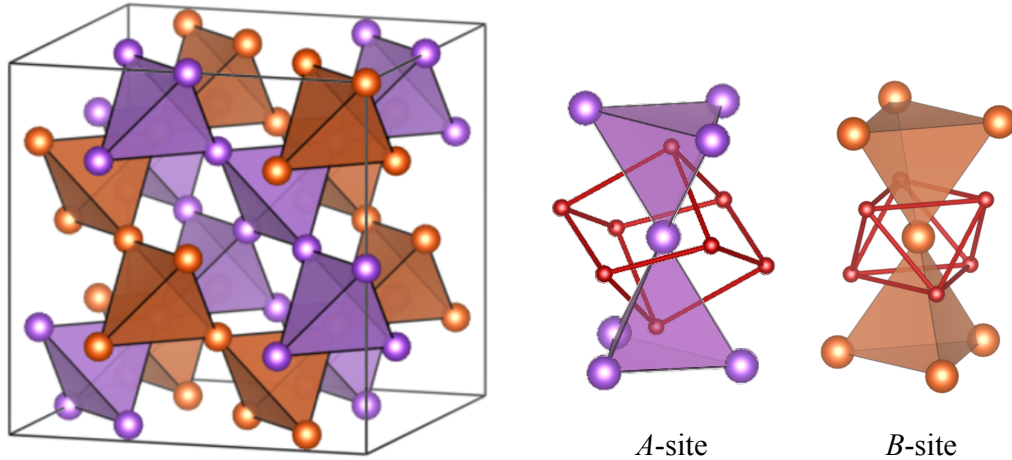


Figure 1.6: Representation of the corner-sharing tetrahedral pyrochlore lattice with the bipartite lattice shown on the left. The A - (purple) and B - (orange) sites are shown with their respective oxygen coordination on the right.

Notice that the A - and B -sites have different oxygen environments. The A -site has

8-fold oxygen coordination forming a distorted cube. On the other hand, the B -site is surrounded by 6 oxygen that form an octahedron. The oxygen environment surrounding each cation is important as it contributes to the crystal field environment, that causes splitting of the spherical 7-fold multiplet of the A -site rare-earth cation. As previously mentioned, there are two distinct oxygen sites that surround the magnetic A -site cation. There are six oxygen atoms (O , $8b$) in a puckered ring surrounding the cation, and two oxygen atoms (O' , $48f$) that are aligned linearly with the A atom. These crystal field levels dictate the unique ground state and magnetic properties of the system. The point symmetry, coordinates and Wyckoff positions of each of these atoms is given below in Table 1.1 [38].

Atom	Point Group Symmetry	Site Coordinates	Wyckoff Position
A	D_{3d}	$(\frac{1}{2}, \frac{1}{2}, \frac{1}{2})$	$16d$
B	D_{3d}	$(0, 0, 0)$	$16c$
O	C_{2v}	$(x, \frac{1}{8}, \frac{1}{8})$	$48f$
O'	T_d	$(\frac{3}{8}, \frac{3}{8}, \frac{3}{8})$	$8b$

Table 1.1: Summary of the symmetry and crystallographic coordinates of the four distinct atoms in the pyrochlore lattice. The Wyckoff position is a labelling convention that relates to the space group of the lattice.

Notice that the only variable parameter is the x-coordinate of O, denoted x . This parameter dictates the shape of the oxygen polyhedra that surround the A and B cations. A more detailed discussion of this can be found in references [12] and [39].

This study aims to look at how a heterogeneous B -site can impact the predicted ground state of a pyrochlore with previously well studied parent compounds (with no B -site disorder). As such, it is also important for us to consider the way in which

B cations coordinate around an atom occupying the A -site. The figure below shows that B cations form a hexagonal ring as the next-nearest neighbour to the magnetic A cation.

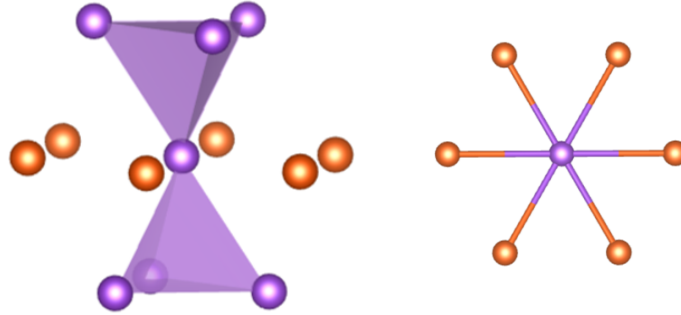


Figure 1.7: The central rare-earth atom (purple) is surrounded by next-nearest neighbour B -site cations (orange) that form a hexagonal ring about the central atom. The view from the side can be seen on the left, and the view looking down the $\langle 111 \rangle$ direction is on the right.

The above image is a bird's eye view along what is referred to as the $\langle 111 \rangle$ direction. This labelling convention is the Miller indices, a more detailed explanation of which can be seen in Section 2.2.1. For illustration, three planes of a cubic structure ($\{100\}$, $\{110\}$, and $\{111\}$) are shown in Figure 1.8.

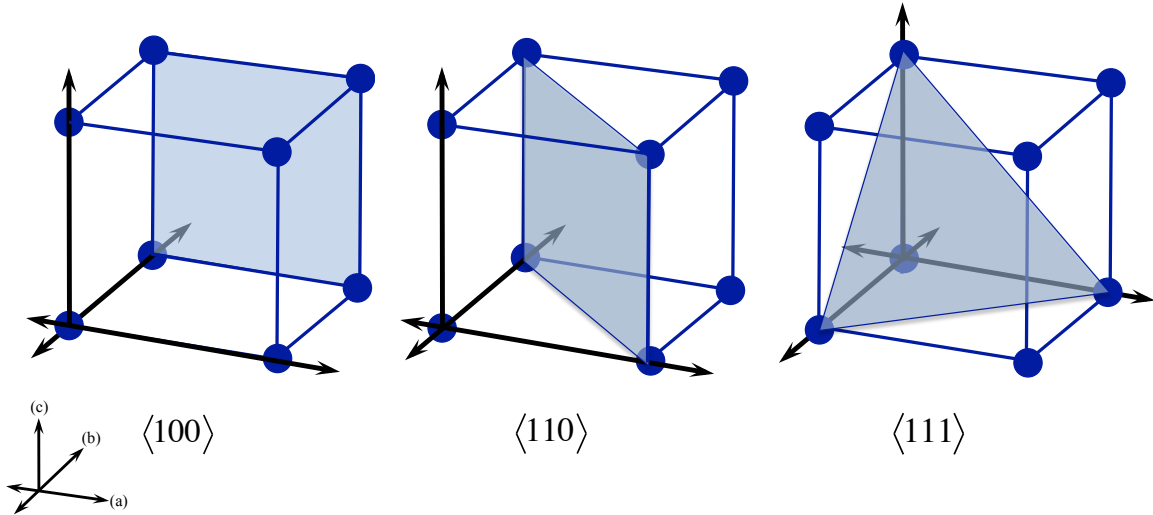


Figure 1.8: The $\langle 100 \rangle$ (left), $\langle 110 \rangle$ (centre), and $\langle 111 \rangle$ (right) crystallographic directions on a cubic lattice.

Labelling these planes within the pyrochlore lattice becomes relevant when we attempt to investigate the magnetism of the system with respect to its crystal structure. The $\langle 111 \rangle$ direction corresponds to one of the principle axis of the corner-sharing tetrahedra as shown in Figure 1.9. When we look at the pyrochlore structure from this perspective, alternating layers form a triangular, two-dimensional lattice alternating with a kagomé two-dimensional lattice (named for its resemblance to the Japanese kagomé basket).

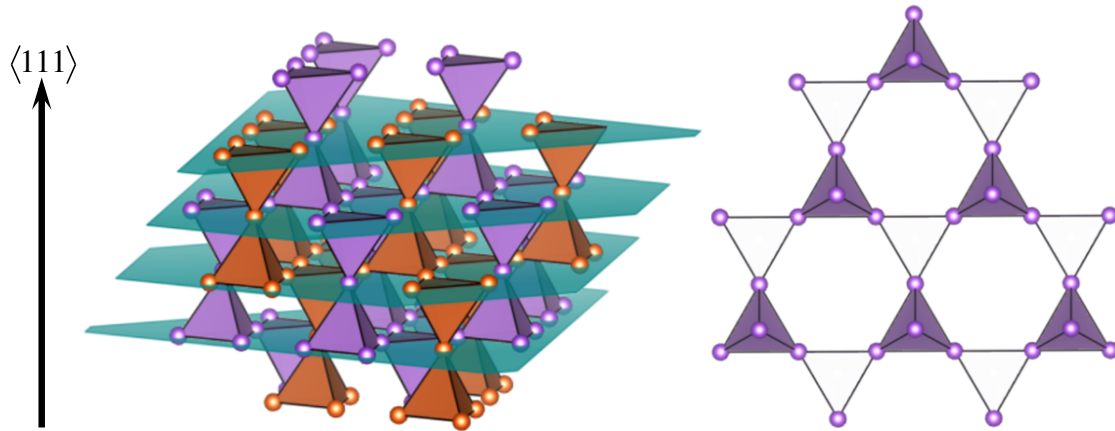


Figure 1.9: The $\langle 111 \rangle$ direction corresponds to the vertical axis of the corner sharing tetrahedra as indicated by the arrow on the left. When we consider the lattice from this perspective, a quasi-two-dimensional layered structure forms with alternating triangular and kagomé layers. These layers are indicated in teal on the left and the kagomé pattern as seen looking down the $\langle 111 \rangle$ direction is shown on the right.

Another relevant description of the pyrochlore lattice is to consider the $\langle 110 \rangle$ direction. For the purposes of this thesis work, investigation of magnetic response along this crystallographic direction is done to contrast against measurements performed along the $\langle 111 \rangle$. However, it should be noted that the tetrahedron's edges lay along the $\langle 110 \rangle$. The α - and β -chains refer to the tetrahedral edges that are parallel and perpendicular to the $\langle 110 \rangle$ direction respectively.

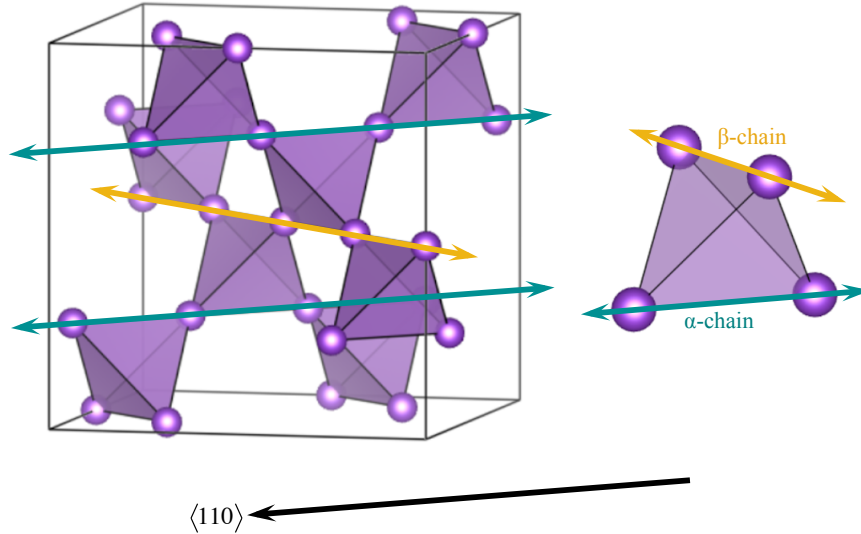


Figure 1.10: The $\langle 110 \rangle$ direction corresponds to the edge of the corner sharing tetrahedra. There are two distinct edges, ones that are parallel to the $\langle 110 \rangle$ direction (referred to as α -chains denoted in teal), and ones that are perpendicular to the $\langle 110 \rangle$ direction (referred to as β -chains denoted in orange).

1.3.2 Competing Interactions Within the Pyrochlore Lattice

Due to the symmetry of the magnetic tetrahedra, a practical way to discuss the anisotropy of a system is to define a local Z-axis for each atom, corresponding to the direction pointing from the magnetic ion to the center of the *A*-site tetrahedron. This leads to the three general cases represented in Figure 1.11. Heisenberg anisotropy refers to moments that have little to no anisotropy. XY anisotropy occurs when the moments are constrained to lie within the plane perpendicular to the local Z-axis. We will focus our attention on the third, most constrained type of anisotropy - where moments are constrained to lie along their local Z-axis. Within the pyrochlore lattice the Ising axis aligns along the $\langle 111 \rangle$ direction, which we refer to as the “easy axis” of the system.

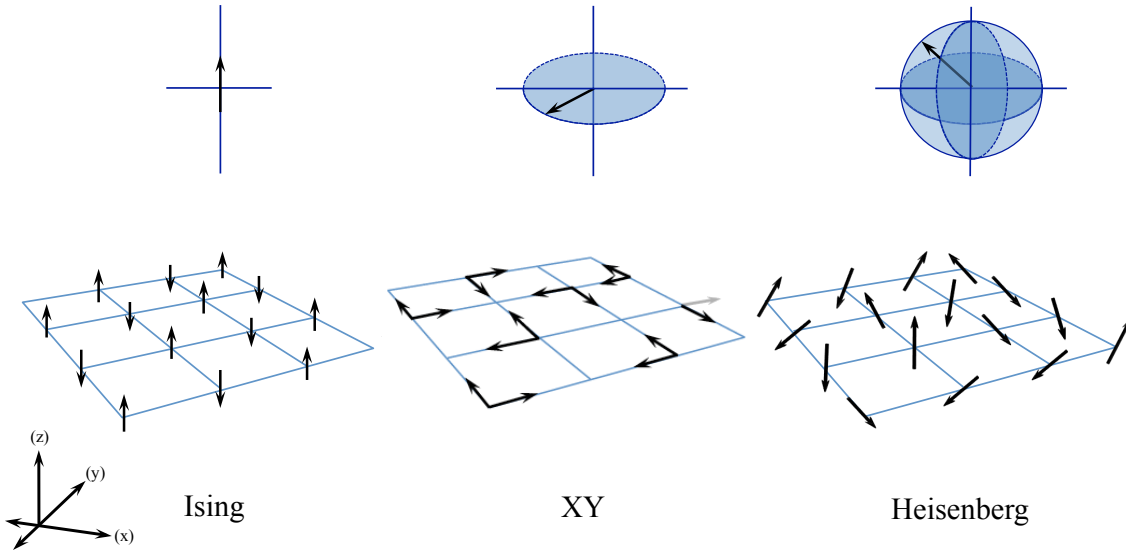


Figure 1.11: Ising (left), XY (centre), and Heisenberg (right) anisotropies are above. Possible configurations of this are shown on a 2D square lattice below. The spins could potentially adopt many different orientations whilst constrained to the XY plane or unconstrained in 3D (as in the Heisenberg case). Illustrated here is a possible spin configuration on a simple 2D square lattice. Note that in bottom centre, the spins are constrained to lay on the XY plane, i.e. that they could fluctuate in direction between the two arrows pictured on single a lattice site.

Putting everything together, we now have a framework in which to study the competing interactions within the pyrochlore lattice that give rise to exotic ground states. The geometry of the bipartite corner-sharing tetrahedral lattice does not allow for antiferromagnetic exchange interactions to be satisfied simultaneously, resulting in energetic compromises being made as the system adopts a magnetic ground state. The anisotropy then dictates the directionality of the magnetic moments with respect to the pyrochlore lattice. Finally, the combination of the type of exchange interaction that occurs between nearest neighbour magnetic moments will dictate the nature of the ground state adopted by the system. Although there is little difference in the

atomic radii, the number of 4f electrons differs for each rare earth cation producing different electron ground states when minimized as shown in Subsection 1.2.1. This leads to different anisotropies and exchange interactions for different lanthanide cations. The interplay between anisotropy and the sign of the exchange interaction leads to different ground states across the series. An example of these varying ordered states are several of the rare-earth titanates, $\text{RE}_2\text{Ti}_2\text{O}_7$. $\text{Sm}_2\text{Ti}_2\text{O}_7$ has Ising anisotropy and antiferromagnetic interactions, and adopts an “all-in all-out” configuration. This combination results in long range order that propagates throughout the system [40]. On the other hand, $\text{Dy}_2\text{Ti}_2\text{O}_7$ exhibits Ising anisotropy and ferromagnetic interactions, thereby adopting a “2-in 2-out” spin ice configuration, where two spins point to the center of the tetrahedron (as seen in Figure 1.12 below). [41].

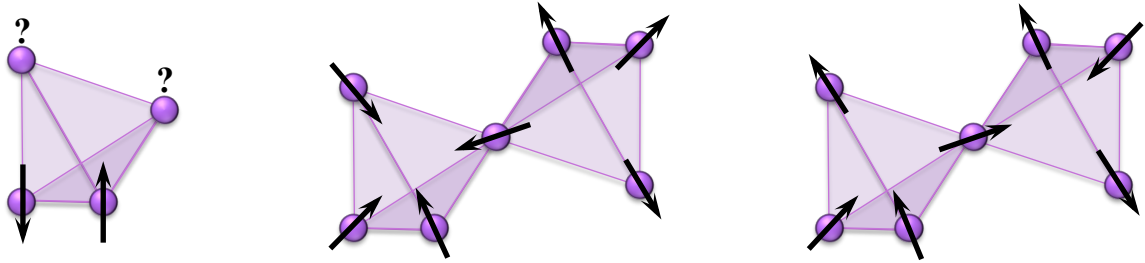


Figure 1.12: The antiferromagnetic global Ising orientation is frustrated on the lone tetrahedron (left). On two corner sharing tetrahedra (as seen in the pyrochlore lattice), antiferromagnetic Ising order adopts “all-in-all-out” orientation (centre). On two corner sharing tetrahedra, ferromagnetic Ising order adopts a “2-in-2-out” configuration (left). *Adapted from A. H. Hallas [3]*.

This particular form of short-range order (SRO) is referred to as “spin ice.” Spin ice ordering has garnered a large amount of interest within the community over the last several decades and will be described in detail in the following section.

1.4 Dysprosium Pyrochlores

One of the most cohesive relationships between experiment and theory is that of the spin ice ground state. The spin ice state has been observed several rare-earth pyrochlores (notably holmium pyrochlores), but we focus specifically on dysprosium-based pyrochlores for the duration of this thesis. Thus far, it has been observed experimentally through magnetization measurements [12, 2, 1], inelastic neutron scattering [12, 41], and ab initio calculations [12, 42] that dysprosium pyrochlores are examples of dipolar spin ices, where the ferromagnetic dipolar interactions dominate.

It may seem counterintuitive to consider the dipolar interactions within a magnetic system, as we typically expect frustration to arise due to nearest neighbour interactions. However, because of the large magnitude of the moment of the dysprosium cation (approximately $10\mu_B$ [43]), these magnetic moments are expected to exhibit effective classical Ising spin behaviour (as referenced in Section 1.3.2 above), which results in a large magnetic dipole interaction energy. Therefore, in order to properly study the spin ice state, we consider only the combined role of exchange (J_{NN}) and dipole-dipole interactions (D_{NN}) [43]. This gives us the expression for the effective interaction

$$J_{eff} = J_{NN} + D_{NN}, \quad (1.4.1)$$

which gives a Hamiltonian that can be used to describe the Ising pyrochlore magnet

$$H = -J \sum_{\langle i,j \rangle} \mathbf{S}_i^{Z_i} \cdot \mathbf{S}_j^{Z_j} + D r_{nn}^3 \sum_{j>i} \frac{\mathbf{S}_i^{Z_i} \cdot \mathbf{S}_j^{Z_j}}{|\mathbf{r}_{ij}|^3} - \frac{3(\mathbf{S}_i^{Z_i} \cdot \mathbf{r}_{ij})(\mathbf{S}_j^{Z_j} \cdot \mathbf{r}_{ij})}{|\mathbf{r}_{ij}|^5}. \quad (1.4.2)$$

where the spin vector $\mathbf{S}_i^{Z_i}$ labels the Ising moment and D is the estimate of the dipole energy scale $D = (\mu_0/4\pi)g^2\mu^2/r_{nn}^3$. The first term in this expression corresponds to

nearest neighbour exchange interactions, the second corresponds to nearest neighbour dipolar interactions, and the third corresponds to next-nearest neighbour dipolar interaction energy U (as seen previously in Equation 1.2.11) [42]. In many materials, the exchange interaction dominates, and dipolar interactions can be ignored. However, in the materials with weak exchange, the dipolar interaction energy scale can be the same order of magnitude as that of the exchange energy and must therefore be accounted for.

1.4.1 Spin Ice

Elaborating more on spin ice ordering, the spin orientation of “2-in 2-out” results in a macroscopically degenerate ground state analogous to that of water ice. In fact, this state is named for the fact that the entropy of the spin ice follows Pauling’s ice rules (described above in Section 1.1.1). It should be noted that the magnetic entropy of spin ice does not exactly match that of water ice due to the corner-sharing nature of the tetrahedra that is absent in the crystal lattice of water ice. This gives rise to an extra factor of $1/2$ and residual entropy of given by:

$$S_{magnetic} = \frac{Nk_B}{2} \ln \left(\frac{3}{2} \right) = \frac{R}{2} \ln \left(\frac{3}{2} \right), \quad (1.4.3)$$

where this residual entropy can be directly measured via heat capacity measurements.

The spin ice state has garnered much attention in the condensed matter community in recent years because the excitations of the “two-in two-out” spin ice phase can give rise to pseudo-magnetic monopoles. The existence of magnetic monopoles was predicted by Dirac in 1931 [44], but have never been observed in a laboratory setting. The lowest energy thermal excitation of the spin ice state can only result when

one of the spins on the tetrahedron flips, resulting in either a “three-in one-out” or a “three-out one-in” configuration. These spin configurations behave as an effective north/south pole pair, according to the direction of magnetic flux originating from each. The relaxation of this state gives rise to the separation of the free poles as the sink and source of flux move further and further apart from one another, resulting in “effective” or “pseudo”-magnetic monopoles [45].

1.4.2 Project Motivation

These so-called “classical” spin ice states seem to persist in various dysprosium pyrochlores and are robust in the face of chemical perturbation. $\text{Dy}_2\text{Ti}_2\text{O}_7$, $\text{Dy}_2\text{Sn}_2\text{O}_7$, and $\text{Dy}_2\text{Ge}_2\text{O}_7$ have all experimentally been shown to exhibit spin ice physics as discussed in references [28], [2], and [46] respectively. It is for this reason that novel dysprosium pyrochlores are excellent systems in which the spin ice state and its origin can be studied. The motivation of this project was therefore to investigate a dysprosium pyrochlore with a disordered B -site and to study the effect of this disorder on the predicted spin ice ground state magnetism. In an effort to answer these questions, $\text{Dy}_2\text{ScNbO}_7$, which was first synthesized by Zouari *et al.* [35] but had not been thoroughly investigated in this context, is the focus of this thesis work.

The B -site is occupied by non-magnetic cations that do not contribute to the magnetism of the sample. However, varying the B -site cation (and therefore changing the B -ionic radius), will result in changes to the size of the unit cell. This is summarized for existing dysprosium pyrochlores as well as for $\text{Dy}_2\text{ScNbO}_7$ in Table 1.2 below.

Spin Ices	a (Å)	$T_{transition}$ (K)
Dy ₂ Ti ₂ O ₇	10.10	1.25
Dy ₂ Sn ₂ O ₇	10.40	1.20
Dy ₂ Ge ₂ O ₇	9.93	0.83
Dy ₂ ScNbO ₇	10.34	0.86

Table 1.2: Summary of dysprosium pyrochlores with varying B -site transition metals with their lattice parameters and transition temperatures. Experimental evidence that the dysprosium titanate [1], stannate [2], and germanate [3] all adopt the spin ice ground state exists in the literature.

Also included in Table 1.2, are transition temperatures measured in the magnetization of each material. These interesting preliminary results, as well as the opportunity to investigate the spin ice state in the presence of charge disorder served as the motivation for this project. Our goal was to explore how the added disorder impacts the magnetic interactions that occur within Dy₂ScNbO₇ at low temperatures.

Chapter 2

Experimental Techniques

2.1 Sample Preparation

Sample preparation is an important facet of any condensed matter study. Sample quality can dramatically impact one's results, particularly when making any effort to investigate magnetic properties. One must carefully take steps to eliminate defects and impurities that can lead to the drawing of false conclusions about the physical properties of one's system.

2.1.1 Synthesis

The most common method of solid state synthesis is also among the simplest. Commonly referred to as the ceramic method, it involves the grinding of reactant solids and heating them (often at very high temperatures) until they react to form the desired product. Stoichiometric amounts of the the oxide form of the target reagents are ground together using a mortar and pestle in order to achieve a small, uniform

particle size and homogeneous mixing. The mixture is then pressed (often using using a hydraulic press) into either a pellet or rod (depending on the mass of the sample), and then heated at a high temperature (up to 2000°C) in a crucible. In general, solid state reactions occur slowly, as the reactions occur at the solid interface between reactants, and a large amount of energy is needed to overcome the lattice energy of their original ionic structure. Homogeneous mixing, small particle size and contact between crystalline faces all increase the rate at which ions can diffuse throughout the reaction matrix. Hence, the grinding and pressing of the powders are crucial steps.

2.1.2 Crystal Growth

The growth of high quality single crystals of novel materials is essential in understanding spatial information about the system. Knowledge of the spatial position of the magnetic ions of interest is imperative to making concrete conclusions regarding the physical behaviour that is observed. One method of obtaining large, high quality, single crystals is called the floating zone method. This method utilizes a temperature gradient - where light is focused by two parabolic, confocal mirrors into a small region that can reach temperatures often in excess of 2000°C. A rod of starting material is then simultaneously rotated and lowered into this region until it meets a lower “seed rod” and the material liquefies to form the so-called molten zone. As the rods are slowly lowered, the material crystallizes as it cools. A schematic diagram, as well as photographs of this melting process, can be seen in Figure [2.1](#).

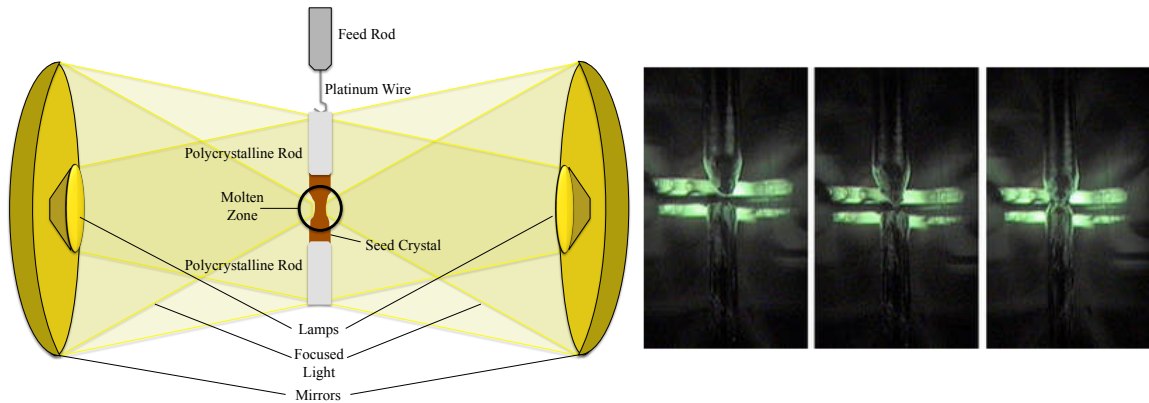


Figure 2.1: A schematic of the floating zone crystal growth technique where confocal mirrors focus light to a point, creating a molten zone as the feed rod is rotated and lowered through this point (left). Images of various stages of crystal growth (right).

This technique is well suited to growing large crystals (up to several centimetres long) required for neutron scattering. Additionally, the technique involves the polycrystalline rods being directly lowered into the molten zone, and with no alumina crucibles involved, there are fewer opportunities to introduce impurities into the single crystal product.

2.2 Structural Characterization

Establishing the quality of the sample is crucial prior to any measurements of physical properties. Impurities or structural deformities can have a dramatic impact on the physical properties of a system including (but by no means limited to) the thermodynamic, electronic, and/or magnetic properties. We characterize our sample using diffraction, a flexible tool for structural characterization of crystalline materials. Before describing the characterization methods used in this work we will first discuss the foundations of scattering as a tool for structural information.

2.2.1 The Principles of Diffraction

The diffraction of electromagnetic radiation has been investigated and utilized for various practical purposes since the 17th century [47]. The diffraction of light was first applied to the investigation of solid materials by the father and son duo William Henry, and William Lawrence Bragg. From Max von Laue's earlier work, it was known that a periodically repeating pattern of atoms present within a crystal could be used as a diffraction grating and that X-rays, with their wavelength on the same order of magnitude as the interatomic spacing of the crystal, would produce a diffraction pattern. Bragg treated the problem as incoming X-rays being reflected off of flat planes of crystals as seen in Figure 2.2.

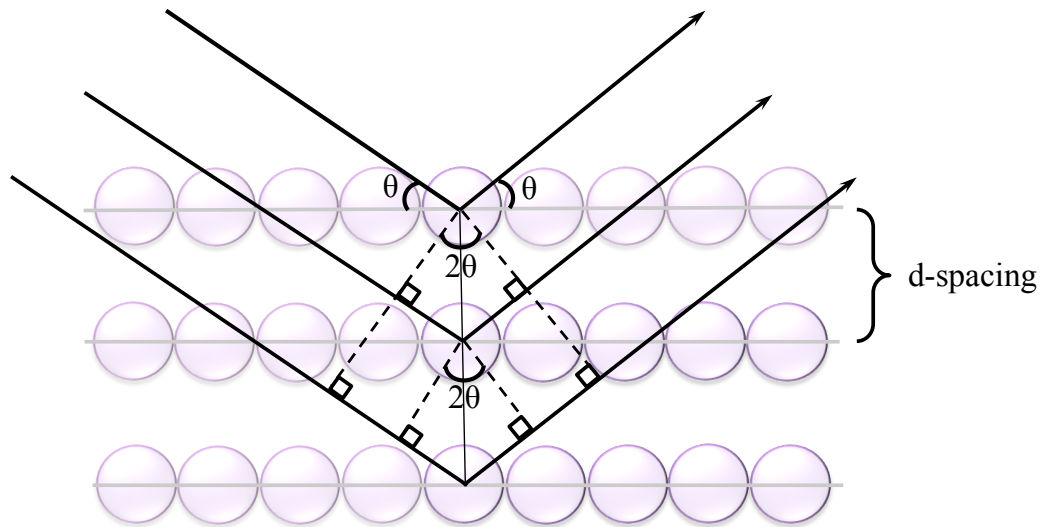


Figure 2.2: Representation of Bragg's Law for a single set of atomic planes separated by a distance d .

Bragg's condition is derived from a geometrical understanding of constructive interference between X-rays of certain wavelengths and incident angle of reflection off of two adjacent planes of atoms. This condition is summarized in the following equation

(which is referred to as Bragg's Law):

$$n\lambda = 2d\sin\theta, \quad (2.2.1)$$

where n is an integer. When the condition is satisfied for two adjacent atomic layers, it is satisfied for many subsequent layers, which gives rise to sharp maxima in the diffraction spectra that are colloquially referred to as Bragg peaks. The success of Bragg's work lay in his interpretation of determining d - the interplanar spacing to identify the nature of the crystal lattice. As the Bragg condition can be satisfied for any family of atomic planes present within the crystal, this provides an opportunity to connect Bragg's law to the stringent mathematical description of a crystalline lattice as a means for identification of the structural features of said lattice.

Crystallographers describe a crystal in terms of the Bravais lattice, which is used to describe the entire symmetry of the crystal. The Bravais lattice consists of all points with the position vector \mathbf{R} , which has the form

$$\mathbf{R} = m\mathbf{a}_1 + n\mathbf{a}_2 + o\mathbf{a}_3. \quad (2.2.2)$$

Where m , n , and o are integers and \mathbf{a}_i , $i = 1, 2, 3$, are lattice vectors. The Bravais lattice describes the periodic array of the repeated basis within the crystal. Lattice planes that exist within a crystal are rigorously defined as a plane containing at least three non-colinear points of a Bravais Lattice, and are denoted by their Miller indices (hkl) . The Miller indices in real space define a plane according to the following vector

representation of its x , y , and z intercepts:

$$(x, y, z) = (\mathbf{a}_1/h, \mathbf{a}_2/k, \mathbf{a}_3/l), \quad (2.2.3)$$

where \mathbf{a}_1 , \mathbf{a}_2 , and \mathbf{a}_3 are the real space lattice vectors. However, dealing with the Miller indices as a collection of planes is awkward and difficult to visualize. It has therefore become common practice to describe them in terms of the reciprocal lattice. The reciprocal lattice is defined by the following relationship

$$\mathbf{R} \cdot \mathbf{G} = 2\pi m, \quad (2.2.4)$$

where m is an integer. It can be seen from this relationship that \mathbf{G} is orthogonal to the plane of atoms that it is describing. \mathbf{G} is the reciprocal lattice vector given by

$$\mathbf{G} = h\mathbf{b}_1 + k\mathbf{b}_2 + l\mathbf{b}_3. \quad (2.2.5)$$

Which is a vector that connects the reciprocal lattice point to the origin. The lattice vectors in reciprocal space can be generated directly from counterpart real space vector according to the following:

$$\mathbf{b}_1 = 2\pi \frac{\mathbf{a}_2 \times \mathbf{a}_3}{\mathbf{a}_1 \cdot (\mathbf{a}_2 \times \mathbf{a}_3)} \quad \mathbf{b}_2 = 2\pi \frac{\mathbf{a}_3 \times \mathbf{a}_1}{\mathbf{a}_1 \cdot (\mathbf{a}_2 \times \mathbf{a}_3)} \quad \mathbf{b}_3 = 2\pi \frac{\mathbf{a}_1 \times \mathbf{a}_2}{\mathbf{a}_1 \cdot (\mathbf{a}_2 \times \mathbf{a}_3)}. \quad (2.2.6)$$

(This being the Fourier transform from real to reciprocal space).

Another relevant vector is called the scattering vector, \mathbf{Q} , and is defined by:

$$\mathbf{Q} = \mathbf{k} - \mathbf{k}', \quad (2.2.7)$$

where \mathbf{k} and \mathbf{k}' are the momenta of the incoming and outgoing wave vectors respectively. The momentum vectors are determined from the wavelength of the reflected wave as $\mathbf{k} = 2\pi/\lambda$. The importance of the \mathbf{Q} scattering vector lies in its definition of the “scattering triangle” as shown in Figure 2.3 below. A scattering event can only be detected if it lies on or near the scattering triangle.

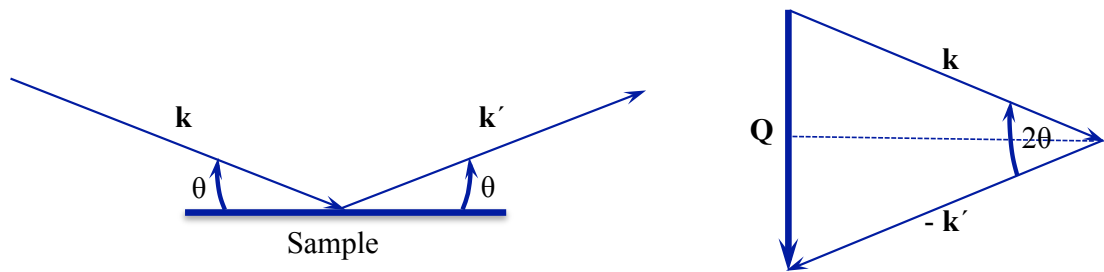


Figure 2.3: Geometry of the \mathbf{Q} -scattering vector via the from vector addition of incident (\mathbf{k}) and refracted (\mathbf{k}') wave vectors.

Additionally, the scattering vector is important to the definition of the Laue condition for scattering (the details of which are outside of the scope of this thesis and can be found in reference [14]). The Laue condition is satisfied if the scattering vector \mathbf{Q} is equal to a reciprocal lattice vector (defined as \mathbf{G} in equation 2.2.5 above). This will result in constructive interference and the appearance of scattering peaks [14].

The techniques described below are the applications of these principles relevant to this thesis work, particularly for the use of structural characterization/confirmation of the crystalline lattice structure

2.2.2 X-ray Diffraction

Electromagnetic radiation is a flexible tool that is used in the investigation of a material's crystal structure. Light that is most suitable for scattering from a crystalline lattice has wavelengths on the order of \AA , which is comparable in magnitude to the interatomic spacing. This is the case for X-ray radiation. One of the strengths of this technique is the ease with which we can produce high quality monochromatic X-ray sources

X-rays used for scattering are commonly produced by using accelerated electrons to excite a target, producing characteristic X-rays. Electrons can be produced by heating a metal filament, called the cathode. These electrons are then accelerated by a large potential difference until they strike a target, called the anode. The electrons hitting the anode lead to both a “white” spectrum of X-rays from the deceleration of electrons as they enter the metal target (Bremsstrahlung radiation), and high intensity peaks at wavelengths corresponding to characteristic radiation from electronic transitions in the anode. The Bremsstrahlung radiation can be filtered out, as it is desirable to use a fixed wavelength for most X-ray diffraction experiments and the highest intensities occur in the characteristic peaks. This filtering process is accomplished using a monochromator, a single crystal arranged such that the radiation incident on the sample comes from the Bragg scattering of the desired characteristic radiation.

Once the monochromatic beam of wavelength λ reaches the sample, the crystal will act as a diffraction grating, and the reflection of X-rays will occur in accordance with the Laue condition described in Section 2.2.1. Thus far, we have discussed crystal structures in terms of the Bravais lattice vector. However, it is important

to consider the case where there is more than one atom present within the unit cell and/or associated with each lattice point. These are described by basis vectors of the form:

$$\mathbf{r}_j = m_j \mathbf{x}_j + n_j \mathbf{y}_j + o_j \mathbf{z}_j, \quad (2.2.8)$$

where m_j , n_j , and o_j are integers, \mathbf{x}_j , \mathbf{y}_j , and \mathbf{z}_j are lattice vectors and \mathbf{r}_j is the vector from the defined origin of our lattice to the center of atom j . With these more complicated crystal structures, Some arrangements of atoms can lead to destructive interference, causing systematic absences (referred to as extinction) of Bragg peaks.

We can predict which peak extinction rules by defining a structure factor, F_{hkl} , which is calculated according to the following:

$$F = \sum_j f_j \exp(i\mathbf{G} \cdot \mathbf{r}_j), \quad (2.2.9)$$

where f_j is the atomic form factor which describes the spatial density distribution of the scattering object in reciprocal space. X-rays interact with the charge distribution surrounding atoms. Charge increases with increasing atomic number Z , leading to a form factor that increases $\propto Z^2$. Further details regarding the atomic form factor, can be found in reference [48].

The structure factor is proportional to the intensity of Bragg peaks via the following relationship:

$$I \propto |F_{hkl}|^2, \quad (2.2.10)$$

where I is peak intensity. Extinction rules can be calculated by using 2.2.9 to determine which combinations of h , k , and l give a structure factor of zero.

The primary technique used for characterizing sample structure in this thesis was

powder X-ray diffraction. A powder, or polycrystalline sample is a collection of many tiny single crystals. Common x-ray diffraction apparatus use a monochromatic (fixed wavelength) source of wavelength λ incident on a sample with a detector rotating about the sample at angle 2θ (as seen in Figure 2.4). Crystallites are assumed to be aligned randomly and peaks in intensity can be observed at detector angles for which Bragg's law (equation 2.2.1) is satisfied. The generalization of crystal orientation in Bragg's law means that all Bragg conditions for a given 2θ are satisfied simultaneously. Analysis of the resulting spectrum requires one to note that, for high symmetry systems not all Bragg reflections will be unique. For example, in a cubic system the (100), (010), and (001) planes all diffract X-rays at the same 2θ angle.

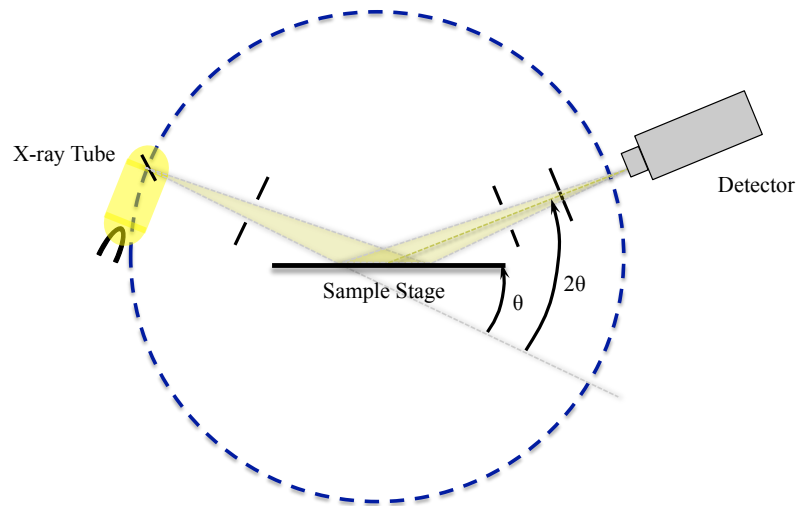


Figure 2.4: Geometry of an X-ray scattering experimental setup illustrating the origin of 2θ .

2.3 Neutron Scattering

Neutrons have properties that make neutron scattering an effective complement to X-rays as a probe of matter. They are neutrally charged, and therefore do not interact with the charge of electron orbitals that make up much of the volume of a solid and can penetrate deeply into a material. Due to the absence of charge interactions, the neutron's two leading interactions in matter (and therefore sources of scattering) are with the strong nuclear force in the nucleus, and the interaction between the neutron's small magnetic moment ($\mu_n \approx -1 \times 10^{-3} \mu_B$) and magnetism (nuclear or electronic).

The strength at which a neutron scatters from a given atom is given by the neutron form factor. This differs from the form factor in X-ray scattering significantly. The neutron atomic form factor is related to the strong nuclear force in an atom and the interaction (which can be repulsive or attractive) with the probe neutron. This leads to a form factor that can differ strongly between isotopes of the same element. Another difference in neutron form factors is the variation in Q . Due to the point-like nature of the nucleus, neutron atomic form factors are virtually independent in Q . This is a result of the nucleus being significantly smaller than the wavelength of the neutron. Neutrons with wavelengths comparable to interatomic distances have energies in the 1-100 meV range. The wavelength dependence of the energies is shown in the following expression:

$$E_{\text{photon}} = \frac{hc}{\lambda} \quad \text{and} \quad E_{\text{neutron}} = \frac{h^2}{2m\lambda^2}, \quad (2.3.1)$$

where h is Planck's constant, c the speed of light, m the mass of a neutron, and λ is the wavelength of the particle. This neutron energy has overlap between both

crystal electric field excitations in 4f electron systems and lattice vibrations (phonon excitations). These excitations can be probed via inelastic scattering as described in Section 2.3.1.

The technique used to produce neutrons for measurements included in Chapter 4 of this thesis is called spallation and was accomplished at the Spallation Neutron Source (SNS) at the Oak Ridge National Laboratory (ORNL). Nuclear spallation is accomplished when a high energy particle (usually produced by means of a linear accelerator) collides with a heavy nucleus that causes the release of many neutrons. A more detailed discussion of the production of neutrons and the operation of the ORNL facility can be found at [49].

The momentum, energy, and flux are all characterizing quantities of a neutron beam. It is convenient to define the scattering cross section (σ_{tot}). The scattering cross section represents how strongly the sample interacts with the scattering probe, and is expressed as the probability of a scattering even per unit area, relative to the flux of the incident neutron beam:

$$\sigma = \frac{N}{\Phi}, \quad (2.3.2)$$

where N is the total number of neutrons scattered per second, and Φ is the flux of the incident neutron beam. The scattering cross section can be written as the sum of its coherent and incoherent components given below:

$$\sigma_{total} = \sigma_{coherent} + \sigma_{incoherent}. \quad (2.3.3)$$

The coherent scattering consists of constructive interference between different atoms,

or magnetic moments which gives us information about the crystal structure or excitations like phonons, or crystal field excitations. The coherent component contains the structural information in the form of Bragg peaks that arise due to long range order, and diffuse scattering that arises due to short range order. Relevant to this work is the relationship between cross section and the probability of neutron absorption. Elements with large absorption cross sections are ill-suited to neutron scattering. The incoherent scattering is isotropic, and corresponds to the self correlation of a given site.

2.3.1 Inelastic neutron scattering

Neutron scattering experiments can be categorized as elastic (where the energy of the incoming neutron is the same as that of the outgoing neutron), or inelastic (where some amount of energy is either gained or lost by the probe with respect to the the sample). Inelastic scattering is used to probe excitations that occur within the system of interest.

A much more detailed description of inelastic, and inelastic magnetic scattering exists in References [50], and [51]. For the purposes of this work, the most relevant application of this technique is the measurement of magnetic crystal electric field (CEF) excitations. For CEF excitations from the ground state, there is a positive energy transfer that peaks about the difference in energy between the two CEF levels. This difference decreases in accordance with the magnetic form factor (with $|Q|$ dependence) squared. This is to be contrasted with excitations from lattice vibrations, which increase in intensity with higher Q .

2.4 Magnetization measurements

Often one of the first experimental probes used to determine the nature of magnetic interactions within a system is the measurement of the magnetization. Magnetization is the quantity that describes the degree to which a material is magnetized when placed in an applied magnetic field. Magnetization (M) is mathematically defined as $M = \mu/v$, that is the magnetic moment (μ) per unit volume (v). While a great deal of information can be garnered from both the magnitude and sign of M , the way magnetization varies with increasing applied magnetic field (H) also characterizes the magnetic properties of a material. This relationship is quantified by the proportionality constant, χ , given in the following expression:

$$\chi = \frac{\partial M}{\partial H}, \quad (2.4.1)$$

where χ is the magnetic susceptibility, M is the magnetization of the sample, and H is the applied field. Note that χ is a dimensionless quantity. This parameter quantifies the degree of magnetization response to an applied magnetic field.

There is a wealth of information to be gained by performing various measurements of χ . Susceptibility can be measured in either a direct current (DC) or an alternating current (AC). The concepts for both of these types of measurement are summarized below (and discussed in more detail in reference [15]). The processes of performing these experiments is also described below in Sections 2.4.1 and 2.4.2.

2.4.1 DC Susceptibility

The direct current (DC) susceptibility reported in this thesis was measured in large part so that the temperature dependence of χ^{-1} could be plotted. When the temperature is high enough that thermal energy is large compared to interaction energy, there is a linear relationship between χ^{-1} and temperature. This allows for the estimation of the strength and type of magnetic interactions via the Curie-Weiss law given in Equation 2.4.2:

$$\chi = \frac{C}{T - \theta_{CW}}, \quad (2.4.2)$$

where θ_{CW} is the Curie-Weiss temperature and C is the Curie-constant [52]. The high temperature paramagnetic regime should follow a linear relationship allowing for the easy calculation of θ_{CW} , and the Curie constant. The Curie-Weiss temperature indicates whether the net magnetic interactions within the material are ferromagnetic (a positive θ_{CW}), or antiferromagnetic (a negative θ_{CW}) [20]. Additionally, the Curie constant can be used to determine the effective moment (μ_{eff}) according to the following:

$$\mu_{eff} = \sqrt{\frac{3k_B C}{\mathcal{N}}}, \quad (2.4.3)$$

where k_B is the Boltzmann constant and \mathcal{N} is Avogadro's number [52].

It is equally as useful to measure the temperature dependence of the susceptibility ($\chi(T)$), which allows us to probe the magnetic ordering (i.e. AFM/FM).

2.4.2 AC Susceptibility

In comparison to DC susceptometry, where the magnetic moment of the sample remains constant for the duration of the experiment, alternating current (AC) susceptibility allows for the investigation of magnetization dynamics. A small, sinusoidally varying, AC driven magnetic field is superimposed upon the DC applied field. The form that this applied magnetic field takes is given in the following equation:

$$H(t) = H_{AC} \cos(\omega t) + H_{DC}, \quad (2.4.4)$$

where $\omega = 2\pi\nu$ is the angular frequency of the AC field, and H_{AC} and H_{DC} are the amplitudes of the AC magnetic field and the static magnetic field component respectively. For simplicity's sake, H_{DC} is often set to zero. The oscillating magnetic field causes the induced magnetization of the sample to exhibit a temporal dependence. At low temperatures, and within a specific frequency window, the local moments of the system are unable to cohere to the sinusoidal frequency of the driven AC field. As the sample response lags behind the applied magnetic field, a phase shift in the magnetization can occur, given by:

$$M(t) = M_{AC} \cos(\omega t - \phi), \quad (2.4.5)$$

where M_{AC} is the induced magnetization from the AC external field and ϕ is the phase shift. Using a trigonometric identity, in combination with our definition of susceptibility given in equation 2.4.4 above, equation 2.4.5 can be rearranged to give

the following expression:

$$M(t) = H_{AC}(\chi' \cos(\omega t) + \chi'' \sin(\omega t)). \quad (2.4.6)$$

This expression allows us to define two separate components of the AC susceptibility. That is, the in-phase (real), χ' , and the out-of-phase (imaginary), χ'' , components. The total susceptibility is expressed as:

$$\chi_{AC} = \chi' + i\chi'', \quad (2.4.7)$$

where χ' corresponds to dispersive processes and is defined as:

$$\chi' = \frac{M_{AC}}{H_{AC}} \cos(\phi), \quad (2.4.8)$$

and χ'' corresponds to dissipative (absorption) processes and is defined as:

$$\chi'' = \frac{M_{AC}}{H_{AC}} \sin(\phi). \quad (2.4.9)$$

Since ϕ generally depends on the driving frequency, AC susceptibility can be used as a direct probe of the dynamics of the system. We can then use this frequency dependence to extract the characteristic relaxation time τ , using the susceptibilities in the high and low ω limits. From this, it can be seen that the numerical value of τ is given by the maximum of the imaginary component of the AC susceptibility.

We used a Quantum Design MPMS™, which uses a **S**uperconducting **Q**uantum **I**nterference **D**evice (SQUID) to give precise measurements of magnetization. A

SQUID magnetometer is one of the most sensitive instruments available to measure the magnetization of a system by utilizing the Josephson Effect. The Josephson Effect describes the phenomenon of supercurrent being able to flow from one superconductor to another while they are separated by a small insulating layer. A detailed description of this effect can be found in reference [53]. Briefly, the Josephson effect occurs because Cooper pairs within one of the superconductors can tunnel through the insulating layer to the other superconductor.

There are two different types of SQUID devices. One type is a DC SQUID which contains two Josephson Junctions and is one of the most sensitive probes of magnetic flux. The other is an RF SQUID which consists of a superconducting loop that has one Josephson Junction (as seen in Figure 2.5). While RF SQUIDS tend to be somewhat less sensitive, they are less costly and easier to make in small batches. Hence, most commercially available SQUIDS are RF SQUIDS [53]. Functionally, a SQUID magnetometer operates based off of its ability to quantize magnetic flux. In an RF SQUID, the superconducting ring is coupled to an LC circuit with a radio frequency current. The loop experiences the flux produced by the current in the RF circuit (Φ_{RF}). The flux quantum enters and exits the loop as the amplitude of the AC current goes from negative to positive. The SQUID can detect small changes in magnetic flux that occur due to a magnetic sample (Φ_q) as a change in the total flux ($\Phi_{RF} + \Phi_q$) changes. This variation will cause the current induced in the SQUID loop to change, resulting in a variation in the voltage of the RF circuit via mutual inductance.

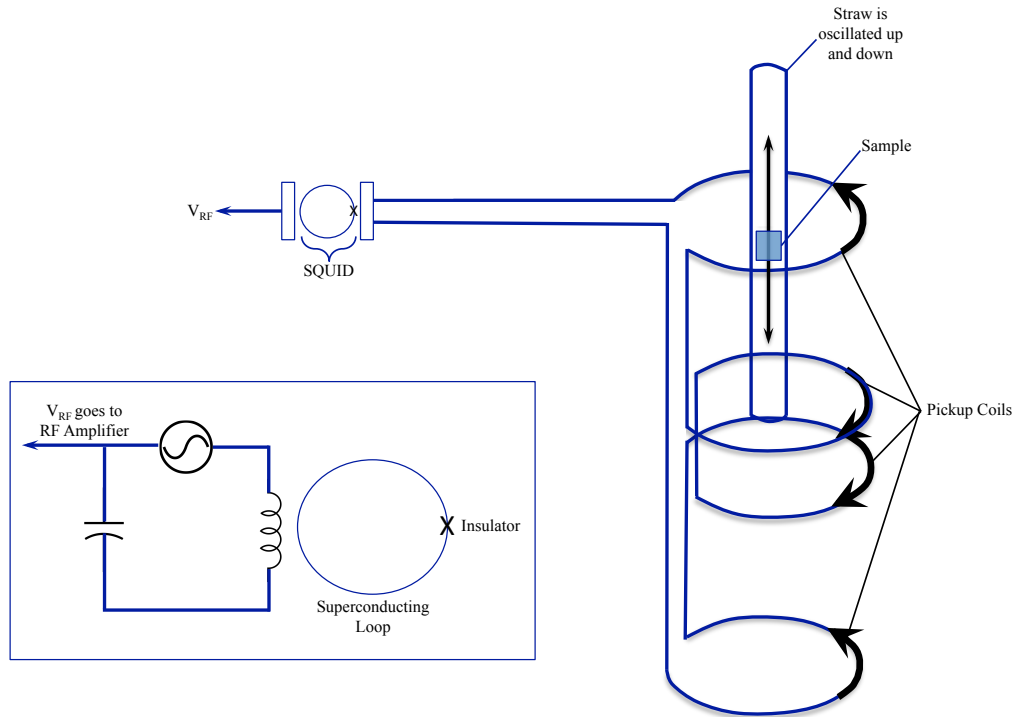


Figure 2.5: A schematic diagram of the sample moving through pickup coils (aka the gradiometer) which are coupled to an RF SQUID as seen in reference [54]. Inset shows a one-junction superconducting loop coupled to a LC circuit with a alternating current source of radio frequency, forming the basis of an RF SQUID (Figure adapted from [55]).

The most common practical application of the ability of a SQUID to determine small changes in magnetic flux is measuring the magnetization of a material. Practically, the sample is placed a distance away from from the SQUID to isolate the superconducting loop away from any magnetic field applied to the sample (either DC or AC depending on the type experiment) and from any temperature changes involved in the experiment. The separation between sample and SQUID is bridged by the use of a gradiometer - a set of four pickup coils that are electronically coupled via a flux

transformer to the SQUID. A representation of this can be seen in Figure 2.5.

The temperature regime of interest (particularly when probing materials containing rare earth cations), tends to be much lower than can be achieved without the use of cryogenics. In order for the SQUID to function, it (along with the superconducting magnet) is in a helium bath which is kept at 4.2 K. The sample space is a low pressure helium environment whose temperature can range from 1.8-400 K. This sample space is able to hold the Quantum Design ^3He insert. This is used to achieve temperatures lower than 1.8 K as the sample is put in a ^3He vapour by the insert. As liquid ^3He has a higher vapour pressure than ^4He , the pressure can be adjusted to achieve temperatures down to 400 mK. A detailed description of helium cryogenics can be found in reference [56].

2.5 Heat Capacity

Heat capacity reflects the ability of a system to absorb heat and as such is a useful tool in probing the various physical properties that are associated with a change in energy. It is a physical quantity that describes the thermal response of a material to the flow of heat. Heat capacity is a measure of the amount of energy required to change the temperature of a substance by a certain amount, and is mathematically described according to the following:

$$C = \frac{\delta Q}{\delta T}, \quad (2.5.1)$$

where δ denotes an inexact differential, and refers to the fact that Q , heat, is a path function [57].

From a practical standpoint, it is impossible to directly measure an inexact differential, and therefore it is required that some thermodynamic parameters are kept constant as heat capacity is measured. It is convenient when considering laboratory conditions to take volume to be constant, giving the following relation:

$$C_V = \left(\frac{\delta Q}{\delta T} \right)_V = \left(\frac{\partial U}{\partial T} \right)_V, \quad (2.5.2)$$

where, for a quasi-static process, the heat uptake (δQ) increases the internal energy (∂U) [9]. This allows us to glean information about the energy fluctuations occurring within a system in certain instances. Heat capacity data can therefore give a wealth of information about the interactions occurring within a solid. These data can then be transformed via Maxwell relations into expressions of varying utility [58].

The heat capacity of a system encapsulates contributions from all of the excitations of a system (magnetic, lattice, crystal electric fields, electronic, etc) and can be partitioned into terms that represent each of these contributions:

$$C_{total} = C_{electronic} + C_{lattice} + C_{CEF} + C_{mag}, \quad (2.5.3)$$

where C_{CEF} and C_{mag} are the crystal electric field and magnetic contributions to the heat capacity respectively. $C_{electronic}$ is the contribution to the heat capacity by the motion of electrons within the system, and is calculated to be $C_{electronic} = \gamma T$ at low temperatures. $C_{lattice}$ is the contribution of the acoustic phonons within the lattice to the heat capacity and is calculated as $C_{lattice} = \beta T^3$ to leading order at low

temperatures. This allows us to rewrite equation 2.5.3 as:

$$C_{total} = \gamma T + \beta T^3 + C_{CEF} + C_{mag}, \quad (2.5.4)$$

As this study focuses solely on insulators, γT is taken to be negligible. The crystal electric field excitations have a higher energy scale than magnetic contributions to the heat capacity and are therefore largely ignored (although there are issues with this approach that will be elaborated upon in Section 3.2.2). As such, heat capacity data can demonstrate details of the magnetism present within a material once the lattice contribution has been subtracted off.

Heat capacity can be measured by several methods. Early measurements in the beginning of the 20th century were accomplished via adiabatic calorimetry, that uses the simple measurement principle of the classical definition of heat capacity given in equation 2.5.1 where heat is input in incremental amounts to cause a subsequent rise in temperature that is then measured. Since then, advancements in the field of condensed matter physics have driven the improvement of techniques to measure heat capacity. The PPMS (Physical Property Measurement System) from Quantum Design utilizes an automated thermal relaxation technique. A platform composed of a thin silicon disk of temperature T_P , is connected to the sample puck (and a copper heat sink) by wires that serve the dual purpose of creating a thermal link between the platform and the heat bath (held at constant temperature T_0) with thermal conductance between the grease and the sample platform K_g , as well as an electrical connection that powers the platform's heater and thermometer. The sample is held on the platform by a thin layer of grease that both ensures good thermal contact, and that the sample is secure. A schematic of this experimental setup is included in

Figure 2.6.

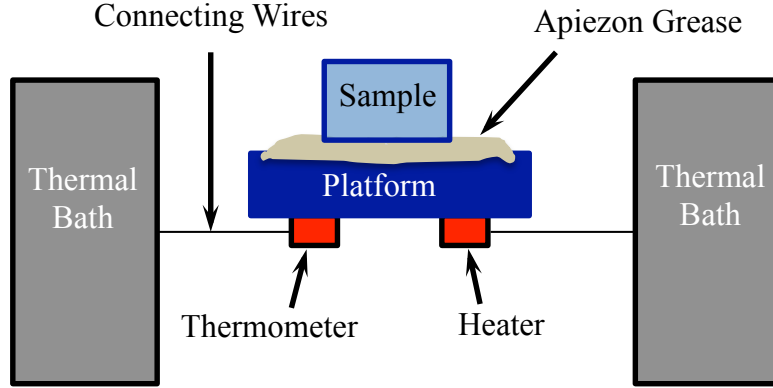


Figure 2.6: Schematic of the heat capacity mount for the Quantum Design Dynacool™ 9 T PPMS adapted from [59].

In a quasi-adiabatic approach, it is assumed that the platform and heat bath are in thermal equilibrium. The heat-balance condition is described by the coupled differential equations:

$$C_{platform} \frac{dT_P}{dt} = P(t) - K_w(T_P(t) - T_s) + K_g(T_s(t) - T_P(t)) \quad (2.5.5)$$

$$C_{sample} \frac{dT_s}{dt} = -K_g(T_s(t) - T_P(t)), \quad (2.5.6)$$

where C , P , K , and T denote the heat capacity, the power applied to the platform via the thin-film heater, the thermal conductance, and the absolute temperature. Meanwhile the subscripts p, w, s, and g refer to the platform, wire, sample, and grease, respectively.

The issue with solving the above equations is that, in reality, $T_P \neq T_S$. That is, the thermal contact between the platform and the sample may not be perfect, resulting in

a temperature difference even at equilibrium. It is therefore more accurate to describe the thermal decay of T_P involving the sum of two exponentials:

$$T_P(t) = T_0 + A\exp(-t/\tau_1) + B\exp(-t/\tau_2). \quad (2.5.7)$$

The Quantum Design PPMS then determines the heat capacity of the sample accurately using a two-tau model. It is the fitting of the time constants τ_1 , that describes the thermal relaxation between the sample and the platform, and τ_2 , which describes the thermal relaxation between the platform and the puck, that allows for the accurate calculation of the heat capacity. The time constants are given by:

$$\tau_1 = \frac{1}{\alpha - \beta} \quad \text{and} \quad \tau_2 = \frac{1}{\alpha + \beta}, \quad (2.5.8)$$

where

$$\alpha = \frac{K_w}{2C_p} + \frac{K_g}{2C_p} + \frac{K_g}{2C_s}, \quad (2.5.9)$$

and

$$\beta = \frac{\sqrt{K_g^2 C_s^2 + 2K_g^2 C_p C_s + K_g^2 C_p^2 + K_w^2 C_s^2 + 2K_w C_s^2 K_g - 2K_w C_s K_g C_p}}{2C_p C_s}. \quad (2.5.10)$$

2.6 Muon Spin Relaxation, Rotation, and Resonance

In 1974 Toshi Yamazaki, Ken Nagamine, Ken Crowe, and Jess Brewer coined the term μ SR to describe the experimental technique of studying the interactions of the

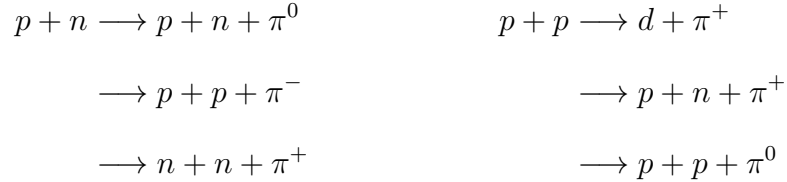
muon spin via the asymmetry of the particle’s decay. The acronym means “**M**uon **S**pin **R**elaxation, **R**otation, **R**esonance, **R**easearch or what have you” [60]. The mnemonic is meant to highlight the similarities to NMR and ESR techniques. In the years following, this large scale facility technique has become a powerful local probe of weak internal magnetic fields present within condensed matter systems. A particular strength of the technique is that, unlike NMR and ESR, μ SR measurements are meaningful in the absence of an external magnetic field, which allows for zero field measurements to be performed. The following is a description of the relevant properties of the muon, as well as a brief description of experimental details relevant to work done in this thesis.

2.6.1 Muon Properties and Production

A muon is an electron-like lepton (a charged, spin $\frac{1}{2}$ subatomic particle that does not undergo strong interactions) with an average lifetime of $2.2 \mu\text{s}$. Muons exist ambiently, primarily in the upper atmosphere where cosmic rays interact with gas particles. However, to achieve the flux of muons required to perform statistically significant analysis, we must produce them artificially. The method of muon production relevant to this work is via the decay of pions to produce so-called surface muons.

All muon experiments reported in this thesis were performed at TRIUMF in Vancouver, BC. There, H^- ions are injected into a large cyclotron and are accelerated to 500 MeV. A carbon foil is used to strip the electrons leaving behind high energy protons that are directed towards a low Z-number (in this case beryllium) target. When

protons collide with the target, pions are produced via the following decay channels:



Negative pions (at rest) are almost immediately absorbed by the target nuclei, and neutral pions have a lifetime of $(0.82 \pm 0.04) \times 10^{-16}$ s. Only positively charged pions will be considered from this point forward, as it is π^+ particles that produce μ^+ . These pions have a lifetime of approximately 26 ns and then decay via the following process:

$$\pi^+ \longrightarrow \mu^+ + \nu_\mu. \quad (2.6.1)$$

Low energy pions with insufficient energy to escape the beryllium target are considered to be at rest, and are referred to as surface pions. This is a three body decay process and as such, conservation of linear momentum results in the opposite travel direction of the resulting muon and neutrino, while conservation of angular momentum tells us that all muons are left handed (since all neutrinos are left handed). Additionally, since the decay process is solely governed by the weak nuclear interaction, each resulting particle is spin $\frac{1}{2}$ and spin polarized due to maximal parity violation. Consequently, muons produced via the decay of surface pions are then 100% spin polarized and have a kinetic energy of 4.119 MeV [60] in the rest frame of the pion.

As previously mentioned, muons produced at TRIUMF for use in μ SR are positively charged. Therefore, in some regards, a muon can be thought of as proton-like with a mass $\frac{1}{9}$ that of a proton. In other regards it can be thought of as a heavy

electron. The table below shows several properties of a positive muon in comparison to those of the electron and the proton.

	μ^+	e^-	p^+
Lifetime	2.19703(4) μs	$>4.6 \times 10^{26}$ years	$>2.1 \times 10^{29}$ years
Spin	1/2	1/2	1/2
Type	lepton	lepton	baryon
Mass [MeV/c ²]	105.65839(4)	0.5109991(2)	938.2723(3)
Magnetic Moment [μ_B]	4.8419710×10^{-3}	1.001165923(8)	1.521×10^{-3}
Gyromagnetic Ratio (γ) [(sT) ⁻¹]	8.516154×10^8	1.76086×10^8	2.67522×10^8
Larmor Frequency ($\gamma/2\pi$) [MHz/T]	135.54	28 024.95	42.58

Table 2.1: Comparison of selected properties of μ^+ with those of the electron and proton ([4], [5]).

Once muons are produced, dipole magnets are used to select muon momentum, and quadrupole magnets are used to focus the muon beam and direct the muons towards the material of interest. The muon is a local probe, and therefore it must be implanted into the sample such that it penetrates deeply enough into the material that it interacts with the local environment, but not so deeply that it passes through the sample. Surface muons in general have a stopping range of 140 mg/cm², which allows for the calculation of their stopping distance once the density of the sample has been taken into account. This stopping depth is approximately between 0.1 and 1 mm [61], and must be considered during sample preparation and mounting.

The muon will come to rest in an electrostatic potential energy minimum within the sample. Since the muon is positively charged, the most likely muon sites within a system are positioned near electrically negative species present within the sample (e.g. oxygen sites in the pyrochlore lattice). Once the muon is implanted into the sample, the muon will decay into a positron. This positron is preferentially emitted

along the direction of the muon spin at the time of decay (as seen in Figure 2.7). The positron and two neutrinos are emitted according to the decay pathway:



This process is a three-body final state decay, which means that, unlike for the decay of a pion seen earlier, the resulting positron will not have an exact energy or momentum but rather a distribution of energies and momenta. The positron is emitted preferentially along the direction in which the muon spin was oriented at the time of decay. However, they are not emitted precisely along the muon spin direction. The following probability function gives the distribution of emission directions:

$$W(\theta) = 1 + a \cos(\theta), \quad (2.6.3)$$

where θ is the angle between the muon spin and direction of positron emission, and a is the asymmetry factor that increases monotonically with the positron energy. The value of a is $a = 1$ gives a maximum energy of 52.83 MeV. The average value of $a = \frac{1}{3}$. How the angular probability distribution function $W(\theta)$ varies can be seen in Figure 2.7 [60].

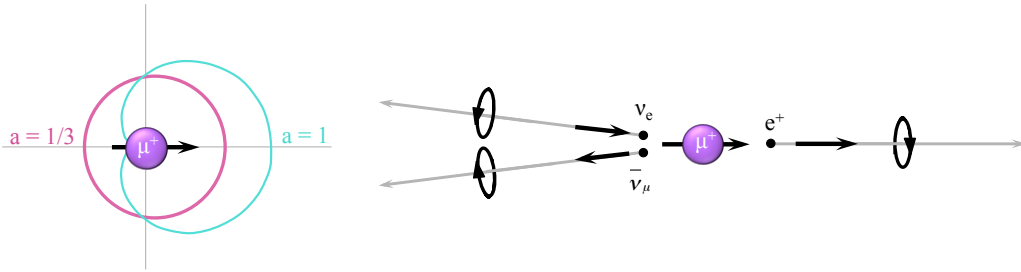


Figure 2.7: The image on the left shows the angular distribution of positrons that result from the decay of a muon, given in equation 2.6.3 above. The asymmetry parameter $a=1/3$ when all positron energies are sampled with equal probability (as seen in magenta) [61]. On the right is the decay of a muon into a positron, and two neutrinos. Black arrows show the momentum and handedness of each decay particle, while grey arrows show the direction of travel of each particle [62].

Since the muon is a spin-1/2 particle, once it comes to rest within the material, its magnetic moment will precess in the local magnetic environment with a frequency of $\omega_\mu = \gamma_\mu B_{loc}$. The spin direction of the muon will evolve within the sample, and the extent of this precession is revealed in the counting rates of the detectors. Unlike the neutrinos that are produced, the emitted positron can be easily detected via a scintillation detector. The detectors are attached to photomultipliers which are used to give statistics on the precession of the muon as a function of time. Detector counting rates are combined and measure a decay spectrum of the muon lifetime, which forms an asymmetry plot that is proportional to the spin polarization function. This polarization function is given by the ensemble average of the probability that a positron will be detected by a specific counter. This depends on several variables including the asymmetric muon decay pattern, the direction of the muon spin at the time of decay, and the position and shape of the counter.

As we are measuring a decay spectrum that pertains to the muon lifetime, it is

essential that the decay event is due to a known muon (i.e. that this process is electronically gated to prevent ambiguity between the decay of multiple muons). This comes from the fact that the statistics of our measurement and the precession are both time dependent. This allows us to match a decay event to a specific muon, giving confidence in the polarization function that is extracted. If there were multiple muons implanted within the sample simultaneously, the interpretation of our data would become meaningless as it would be impossible to discern which positron came from which muon. Therefore, it is vital that only one muon enter the sample at a time. Any events in which more than one muon exists within the sample simultaneously are discarded. This is achieved by use of a thin scintillation detector at the entrance of the sample cavity. Detection of a muon entering the sample starts a digital timer that stops when a positron is detected. This triggers the recording of a count/event as the time between the implantation of the muon and the detection of a positron. This allows for the construction of a histogram from which spatial and temporal information about the local magnetic fields present within the sample can be determined [63].

Analysis of this polarization function requires special consideration of the experimental geometry, as discussed in the following section.

2.6.2 Experimental Setup

During a μ SR experiment, the detector orientation, the applied magnetic field, and muon spin orientation are all variables over which the experimenter has some amount of control. As such there exists a labelling convention that has been devised to describe μ SR experiments using surface muons (which are initially spin polarized

antiparallel to their momentum vector). The standard array of scintillation detectors consists of six counters which are oriented as seen in the inset of Figure 2.8. They are labelled F (forward), B (backward), U (up), D (down), L (left), and R (right). The unrotated implanted muon polarization points towards the backward counter.

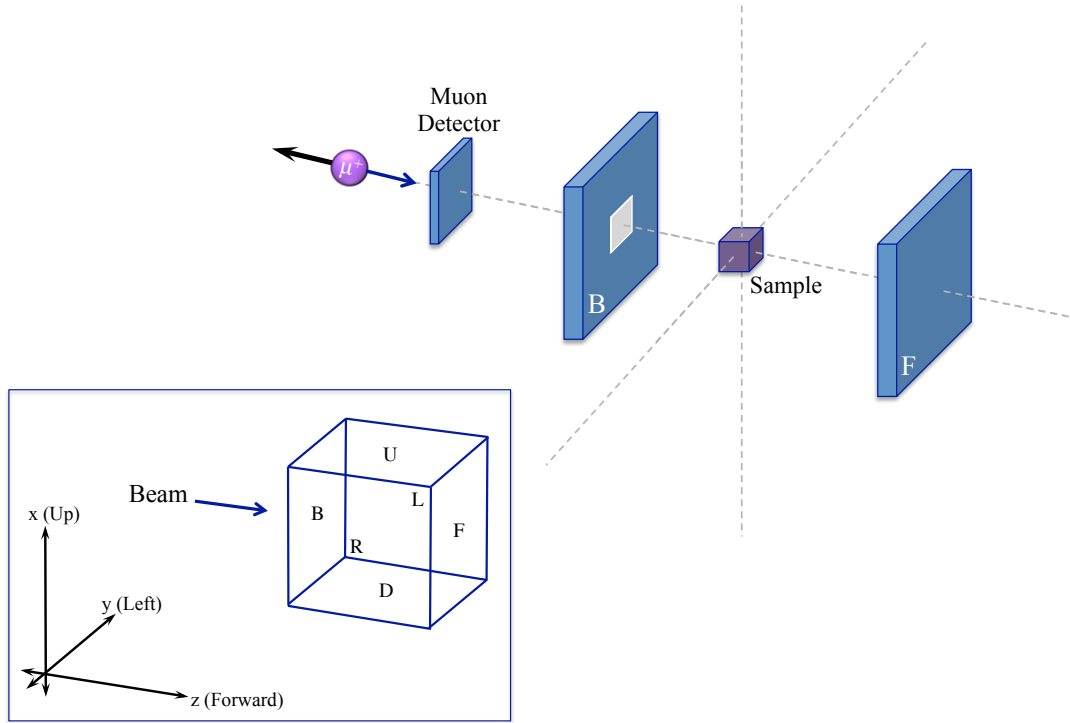


Figure 2.8: Geometry of the positron detectors surrounding the sample for a zero field muon relaxation measurement. The muon detector triggers a timer to measure the time between muon implantation and decay, forward and backwards detectors are used to detect positron emission. The blue arrow indicates the trajectory of the muon and the black arrow indicates the spin of the muon. The inset shows the coordinate system of all six detectors [61], [60].

The μ SR asymmetry spectra can be extracted from the time histogrammed decay positron spectra. The number of decay positrons, $N_i(t)$, can be determined according

to the equation below:

$$N_i(t) = N_i^0 e^{-t/\tau_\mu} [1 + A_i^0 P_i(t)] + B_i^0, \quad (2.6.4)$$

where N_i^0 is a normalization constant and A_i is the maximum precession amplitude (the intrinsic asymmetry of the positron detector). B_i^0 is a time independent random background that results from spurious “stop” signals detected by the positron detectors that do not correspond to the decay of the muon within the sample, and $P_i(t)$ is the time evolution of the muon spin polarization. The polarization function, $P_i(t)$, is given by:

$$P_i(t) = \cos(\omega_\mu t + \theta_i), \quad (2.6.5)$$

where ω_μ is the precession frequency of the muon and θ_i is the initial phase of the muon spin polarization vector.

Equation 2.6.4 can be applied to each counter in the forward-backward pair and the counts can be combined to obtain a total asymmetry function as follows:

$$N_F(t) = N_F^0 e^{-t/\tau_\mu} [1 + A_F^0 P_z(t)], \quad (2.6.6)$$

$$N_B(t) = N_B^0 e^{-t/\tau_\mu} [1 - A_B^0 P_z(t)], \quad (2.6.7)$$

$$A_F P_z(t) = \frac{\alpha N_F(t) - N_B(t)}{\alpha \beta N_F(t) + N_B(t)}, \quad (2.6.8)$$

where $\alpha = \frac{N_B^0}{N_F^0}$, and $\beta = \frac{A_B}{A_F}$. In this context, α is a parameter that corrects for the differences in the solid angle of opposing detectors, as well as difference in efficiency, beam intensity, and delivery. The β parameter corrects for the difference in counter

asymmetry based off of the construction of the counters. Changes in α are seen in the asymmetry spectra as y-offset, whereas changes in β result in a distortion of the vertical axis. While β is generally expected to be close to 1, this is not the case for thick samples. Unlike α , it is practically difficult to measure β .

The experimental geometries of a μ SR experiment are generally classified into transverse field (TF) measurements where the external magnetic field is applied perpendicular to the initial muon polarization, and longitudinal field (LF) measurements where the field is applied parallel to the initial muon spin. Measurements in which no external magnetic field is applied (ZF) are categorized as a subset of LF measurements. While TF measurements are useful in measuring volume fraction, or frequency shift, it is not of particular relevance to this work and will not be discussed further.

Longitudinal field μ SR experiments are often used to probe dynamics as the component of the muon spin polarization along the applied field can be measured. The asymmetric decay pattern of the muon dictates the probability with which a positron will pass through a given counter. Recording the ratio of the number of positrons detected in counters 180° out of phase with each other (the forward and backward counters in the case of LF measurements) as a function of time allows for the construction of the muon spin polarization function from the experimental asymmetry.

In LF measurements, the experimental asymmetry, as well as the relaxation of the muon spin are extracted in order to garner information about the dynamics of the local magnetic environment. A more in depth discussion about relevant models for fitting data to extract these parameters, and the use of LF μ SR measurements to probe static and dynamic magnetism is beyond the scope of this work and can be found in reference [64].

Chapter 3

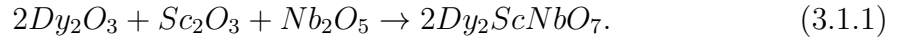
Bulk Property Measurements

3.1 Previous work

Previously unpublished results on $\text{Dy}_2\text{ScNbO}_7$ were the work of my undergraduate honours thesis. This section provides a brief overview of this work and its relevance to the body of this Master's thesis. The initial motivation for this project was alluded to in the above section 1.4, where the primary goal of this study was to investigate the effect of a disordered *B*-site in $\text{Dy}_2\text{ScNbO}_7$, and how this perturbation from the conventional dysprosium pyrochlore formula of $\text{Dy}_2\text{B}_2\text{O}_7$ affects the low temperature physics of the system. Where typically these types of systems adopt a spin ice ground state that is relatively robust to chemical perturbation, our intention was to investigate whether this held with added disorder on the *B*-site.

As with many condensed matter physics or solid state chemistry endeavours, the starting point of this project was the synthesis of a polycrystalline sample of $\text{Dy}_2\text{ScNbO}_7$. This was fairly easily accomplished using the ceramic method outlined

in 2.1.1 above. Each starting material was combined in stoichiometric amounts according to the following chemical equation:



These reagents were then ground and pressed into a rod using 65 MPa of pressure in the hydraulic press. The rods were then fired at 1400°C for 48 hours with intermittent re-grinding every 12 hours.

The crystal growth of Dy_2ScNbO_7 was initially attempted using the floating zone crystal growth technique described in Section 2.1.2 using a Quantum Design image furnace at The University of Winnipeg. Initial attempts were unsuccessful with large amounts of branching and an unstable floating zone. The first successful attempt at crystal growth was accomplished in collaboration with Duke University and the crystal can be seen below in Figure 3.1.

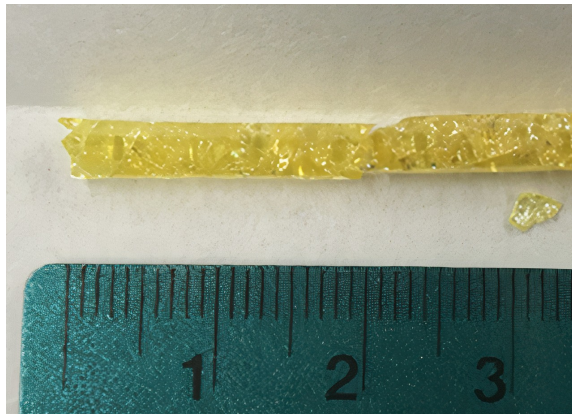


Figure 3.1: Large single crystal of Dy_2ScNbO_7 grown using the floating zone technique. While there are obviously multiple grains, it was possible to align several small pieces along various crystallographic axes. All measurements performed on “single crystal Dy_2ScNbO_7 ” were performed on this crystal.

The difficulties associated with growing a single crystal of Dy_2ScNbO_7 are a result

of the ratio of the *A*- and *B*-site cations being just on the edge of the zone of stability mentioned in Section 1.3. This problem was overcome by increasing speed at which the crystal was grown. Very fast growth rates are required to prevent undesirable branching and to achieve a high quality single crystal.

The ratio between the *A*- and *B*-site cation radii in this material lies close to the edge of stability for a pyrochlore. Therefore, an initial concern was that the crystal growth process, during which the material is subject to extreme conditions, would result in $\text{Dy}_2\text{ScNbO}_7$ adopting the defect fluorite structure. The defect fluorite structure is a parent of the pyrochlore in which there is no preference for either cation to occupy the *A*- or *B*-site.

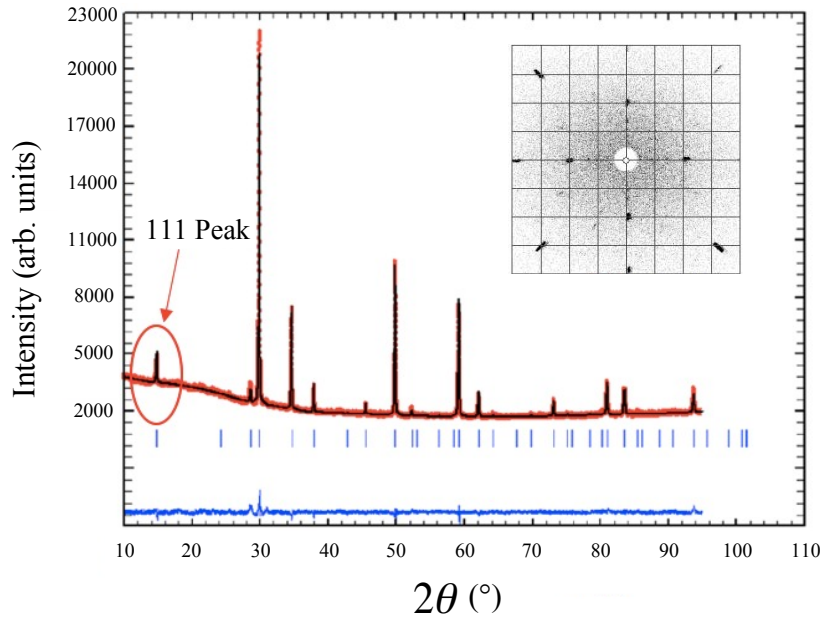


Figure 3.2: Rietveld refinement performed on the powder X-ray diffraction. This confirms the FCC pyrochlore structure by the emergence of several peaks indicating symmetry about the $[111]$ crystallographic axis (indicated in red). Inset is the Laue X-ray diffraction which confirms cubic symmetry.

The Laue diffraction pattern confirmed a cubic structure (seen in the inset of

Figure 3.2). Regrinding a small piece of the crystal allowed for us to take a powder X-ray diffraction scan of the material after undergoing the crystal growth process. The Rietveld refinement of said diffraction pattern showed that the crystal had indeed maintained the pyrochlore structure as seen in Figure 3.2 above. The determination of extinction rules from the structure factor of a face centered cubic lattice (as described in Section 2.2.2) tell us that we should observe the $\langle 111 \rangle$ peak which is present in the diffraction pattern in Figure 3.2 and is circled on the image above in red.

One of the first measurements performed on the polycrystalline sample of $\text{Dy}_2\text{ScNbO}_7$ were DC Magnetometry measurements. DC magnetization allows us to determine the type of interactions which occur between magnetic moments as well as probing the degree of frustration, and determining whether any phase transitions occur. The temperature dependence of the real susceptibility was measured over the temperature range of 1.8-100 K as seen on the left of Figure 3.3. Over this range, paramagnetic behaviour was confirmed as the susceptibility was inversely proportional to the temperature. This implies that there is no magnetic ordering in this temperature regime. The susceptibility measurement taken with a 5 T applied magnetic field saturates at 0.1 Oe which can also be seen below in Figure 3.3.

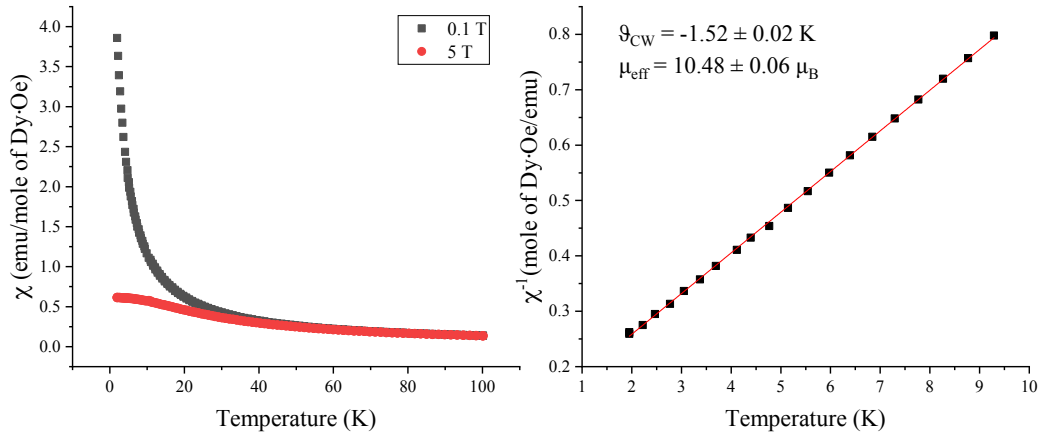


Figure 3.3: DC susceptibility of polycrystalline $\text{Dy}_2\text{ScNbO}_7$, measured in a Quantum Design PPMS using the VSM attachment. Data collected in 0.1 T applied field are in black, data collected in an applied field of 5 T are in red (left). A linear Curie-Weiss fit without diamagnetic corrections is shown in red. Fitting the low temperature region of the inverse susceptibility allowed for the determination of Curie-Weiss temperature as well as the effective magnetic moment (right).

The inverse of the susceptibility was plotted and a low temperature linear regression (seen in red in Figure 3.3 on the right) was performed to obtain an expression that follows the Curie-Weiss Law (Eq. 2.4.2). The low temperature regime was specifically used to avoid possible crystal electric field contributions to the magnetization. The linear trend of χ^{-1} indicates that the system exhibited Curie-Weiss behaviour over the fitted range. From the Curie-Weiss law, we were able to extract the Curie-Weiss temperature ($\theta_{CW} = -1.52 \pm 0.02$ K) and the Curie constant ($C = 13.61 \pm 0.05$ mol·Oe/emu·K). The small negative θ_{CW} indicated net antiferromagnetic interactions within $\text{Dy}_2\text{ScNbO}_7$. The Curie constant was used to determine the net magnetic moment of Dy^{3+} within the $\text{Dy}_2\text{ScNbO}_7$ pyrochlore lattice where $\mu_{eff} = 10.48 \pm 0.06 \mu_B$. This is slightly reduced from the theoretically predicted μ_{eff} of a free Dy^{3+} ion ($10.6 \mu_B$).

Additional DC magnetometry measurements were performed at McMaster University using an RF SQUID as described in Section 2.4.2. Here the real susceptibility was measured twice - once where the applied field of 20 Oe was applied after cooling to base temperature (zero field cooling, or ZFC), and once where the small applied magnetic field of 20 Oe was applied before the cooling process (field cooled or FC). ZFC/FC susceptometry was used to determine the temperature dependence of the magnetic ordering. ^3He was used to measure down to 0.3 K. Bifurcation between the ZFC/FC magnetization indicated irreversibility at 0.86 K which can be observed in Figure 3.4 below, and is generally a sign of glassiness.

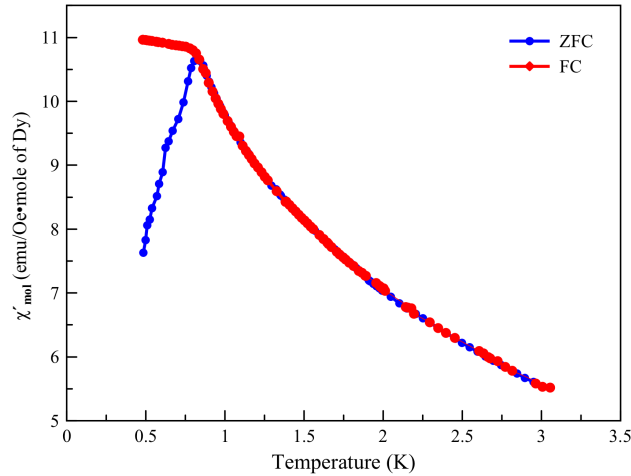


Figure 3.4: Zero field cooled (ZFC) and field cooled (FC) DC susceptibility of polycrystalline $\text{Dy}_2\text{ScNbO}_7$. Note the obvious temperature dependence that varies between the FC and ZFC data. Splitting occurs at approximately 0.86 K indicating a collective transition of some type.

This result of such a low temperature transition was interesting as it was anomalously low compared to other dysprosium pyrochlores of similar B -site cation radii (as discussed in Section 1.4). The sharp feature observed in the ZFC measurement

is more indicative of some type of long range ordering rather than that expected for the spin ice state. These data were some of the first evidence that $\text{Dy}_2\text{ScNbO}_7$ does not exhibit classical spin ice behaviour at low temperatures.

Preliminary AC susceptibility measurements were also performed on polycrystalline $\text{Dy}_2\text{ScNbO}_7$ using the RF SQUID at McMaster University (the details describing such measurements can be found below). The frequency dependence of the AC Susceptibility was only measured at three temperatures that were inside of our window of measurement. In any measurement performed at a temperature higher than 0.9 K, the imaginary component of the susceptibility (χ'') peaked at higher frequencies than we were able to observe. Therefore a statistically significant Arrhenius type analysis could not be performed. This did, however, tell us that $\text{Dy}_2\text{ScNbO}_7$ had much faster spin dynamics compared to other analogous dysprosium pyrochlores, that had E_a up to several Kelvin with observable maxima of χ'' .

Heat capacity measurements seemed to be among some of the most compelling results, as the integration of the magnetic component of the heat capacity divided by temperature was performed to extract the magnetic entropy of the system. Early heat capacity measurements were performed on polycrystalline $\text{Dy}_2\text{ScNbO}_7$ over a temperature range from 1.8-60 K. The entropy exceeded the value predicted for a spin ice from Pauling's Ice rules [11]. However, it fell short of $R\ln 2$, which is the expected value for a doubly degenerate ground state system exhibiting long range order. This value is theoretically predicted as Dy^{3+} is a Kramers ion.

Finally, diffuse neutron scattering measurements were performed at Chalk River as can be seen in in Figure 3.5 below. Measurements were taken on polycrystalline $\text{Dy}_2\text{ScNbO}_7$ in an annular can in order to decrease neutron absorption. The figure

below shows the scattering data after background subtraction.

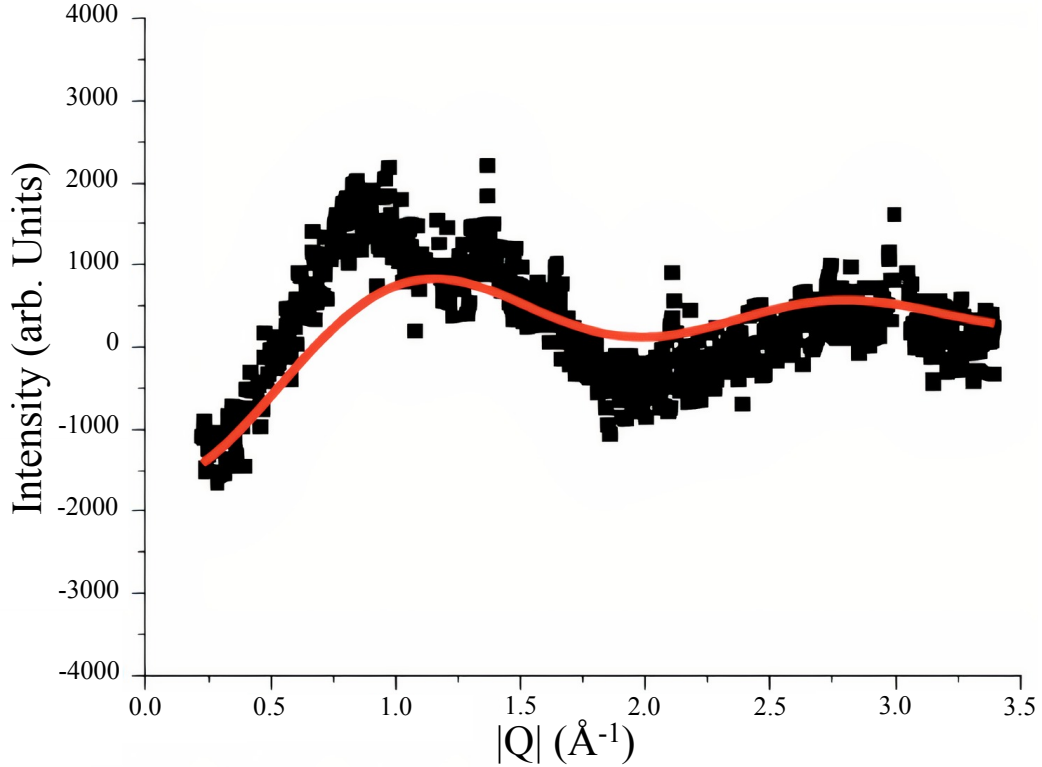


Figure 3.5: Magnetic diffuse neutron scattering performed on polycrystalline $\text{Dy}_2\text{ScNbO}_7$ at 400 mK, in an annular can, on C2 at Chalk River, ON. The $|Q|$ dependence of the scattering intensity shown is the result of a high temperature subtraction with a preliminary $\sin(QR)/QR$ fit in red.

These preliminary data contradicted other indicators that $\text{Dy}_2\text{ScNbO}_7$ adopts long range order. Diffuse scattering tells us that some short range order does possibly exist in the system. An attempt to fit the correlations present in the data using

$$I \propto \langle \mathbf{S}_i \cdot \mathbf{S}_j \rangle \frac{\sin(QR)}{QR}, \quad (3.1.2)$$

where S_i and S_j are spin vectors, can be seen in red in Figure 3.5. Clearly this is not a particularly good fit. Additionally, several features of the subtracted data, like

the negative amplitude and apparent splitting of the first peak, left us with more questions than answers and a myriad of future work left to be done on $\text{Dy}_2\text{ScNbO}_7$.

3.2 Bulk properties and Phase Diagram Construction

Continuing the investigation of this mixed B -site dysprosium pyrochlore, this thesis work aims to further explore the magnetic properties of $\text{Dy}_2\text{ScNbO}_7$ in order to fully understand the effect of B -site disorder on its ground state physics of a dysprosium pyrochlore. In an effort to better understand $\text{Dy}_2\text{ScNbO}_7$, bulk property measurements were compared and contrasted to two extreme cases of materials in this family. It is widely agreed upon that $\text{Dy}_2\text{Ti}_2\text{O}_7$ displays spin-ice phenomenology as mentioned in Section 1.4. We consider $\text{Dy}_2\text{Ti}_2\text{O}_7$ to lie on the “fully ordered” end of our dysprosium pyrochlore spectrum (from a strictly structural perspective), where the A - and B -sites are nominally free of defects. On the opposite end, we have the “fully disordered” $\text{Dy}_2\text{Zr}_2\text{O}_7$ which adopts the defect fluorite structure and the disorder refers to the lack of distinction between an A - and B -site on a corner-sharing tetrahedral lattice. A physical parameter to immediately compare between these three materials is the Curie-Weiss temperature, which is extracted from the DC magnetization. The θ_{CW} of $\text{Dy}_2\text{Ti}_2\text{O}_7$ is 0.2 K [1], whereas $\text{Dy}_2\text{ScNbO}_7$ and $\text{Dy}_2\text{Zr}_2\text{O}_7$ have a θ_{CW} of -1.52 ± 0.02 K and -3.2 K respectively [65]. A small, positive Curie-Weiss temperature ($\theta_{CW} > 0$) indicates net ferromagnetic interactions and a small, negative Curie-Weiss temperature ($\theta_{CW} < 0$) indicates net antiferromagnetic interactions. Therefore we can conclude that the dominant interactions in $\text{Dy}_2\text{Ti}_2\text{O}_7$ are ferromagnetic, while the

dominant interactions of both $\text{Dy}_2\text{ScNbO}_7$ and $\text{Dy}_2\text{Zr}_2\text{O}_7$ are antiferromagnetic.

This section discusses the acquisition and analysis of much higher quality and a larger quantity of AC susceptibility measurements performed on the single crystal of $\text{Dy}_2\text{ScNbO}_7$ shown in Section 3.1. We examine how these data compare to analogous measurements of the aforementioned dysprosium pyrochlores to help us better understand the spin dynamics of this sample. These AC susceptibility curves, as well as the construction of a heat capacity phase diagram in which the temperature and field dependence of the heat capacity are measured along several different crystallographic axes, make up a significant portion of this thesis work.

3.2.1 AC Susceptibility

Real Susceptibility

AC susceptibility measurements included in this thesis work was performed using a Quantum Design MPMSTM Superconducting QUantum Interference Device (SQUID) located at McMaster University. This instrument is an Radio Frequency (RF) SQUID with a gradiometer. AC data was acquired using the Quantum DesignTM AC and Helium-3 inserts. Plotting the real susceptibility as a function temperature $\chi'(T)$ (as seen in Figure 3.6), qualitatively appears to indicate spin glass behaviour. As the excitation field frequency becomes smaller, the peak in $\chi'(T)$ increases in amplitude, becomes sharper, and moves to a lower temperature. All of these signatures are typical features of dynamic spin glasses [21] and can be seen in the figure below.

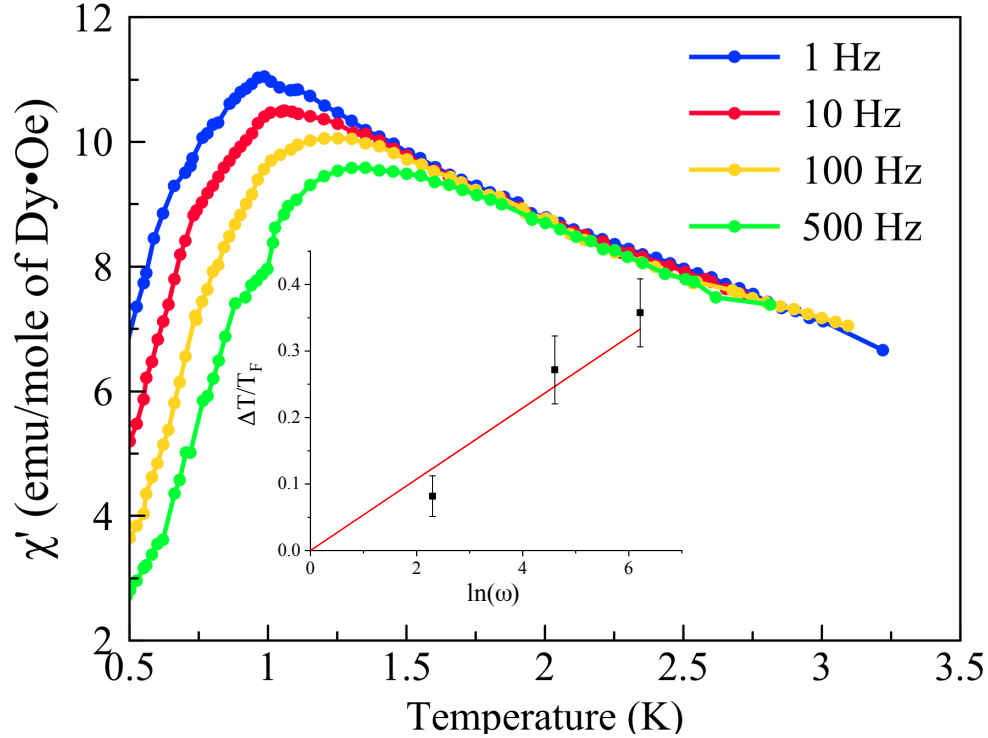


Figure 3.6: Temperature dependence of the real component of the AC Susceptibility of a single crystal $\text{Dy}_2\text{ScNbO}_7$. The measurement was performed at several different frequencies. Inset is the graphical depiction of the Mydosh Parameter [21]

In contrast to $\text{Dy}_2\text{Ti}_2\text{O}_7$, which is similar in peak shape but a much lower intensity, $\chi'(T)$ of $\text{Dy}_2\text{Ti}_2\text{O}_7$ goes to zero below 0.5 K which is indicative of complete spin freezing below that temperature. However, as can be seen in Figure 3.6, $\chi'(T)$ of $\text{Dy}_2\text{ScNbO}_7$ does not go to zero over the measured temperature interval. This implies the opposite - that there is incomplete spin freezing below this temperature with spin fluctuations that persist to very low temperatures (which is seen in many geometrically frustrated materials [65]).

On the other hand, $\chi'(T)$ of $\text{Dy}_2\text{Zr}_2\text{O}_7$ appears to be more similar to that of $\text{Dy}_2\text{ScNbO}_7$. There is the same trend peaks of increasing in amplitude, becoming

sharper, and moving to a lower temperature with increasing frequency. While both $\text{Dy}_2\text{Zr}_2\text{O}_7$ and $\text{Dy}_2\text{ScNbO}_7$ qualitatively appear to exhibit characteristic features of a spin glass in the frequency dependence of $\chi'(T)$, a quantitative analysis paints a slightly different picture. The Mydosh parameter is a measure of the frequency dependence of temperature shift and is expected to be 0.004-0.018 for conventional spin glass systems [21]. The Mydosh parameter (ϕ) is given by the following equation:

$$\phi = \frac{\Delta T_F}{T_F \ln(\omega)}, \quad (3.2.1)$$

and is extracted from $\chi'(T)$ by plotting the logarithm of frequency measured against $\frac{\Delta T_F}{T_F}$. T_F is the temperature at which the maximum in $\chi'(T)$ occurs for the lowest measured frequency i.e. the temperature of χ'_{max} measured at 1 Hz. The Mydosh parameter of $\text{Dy}_2\text{Zr}_2\text{O}_7$ is $\phi = 0.28$ which is several orders of magnitude larger than expected for conventional spin glasses. For $\text{Dy}_2\text{ScNbO}_7$, $\phi = 0.05$, which gives some evidence that the system is not conventionally glassy (or that the frequency dependence of $\chi'(T)$ is at the very least stronger than for that of conventional spin glasses), despite the initial qualitative interpretation to the contrary.

Imaginary Susceptibility

The frequency dependence of the imaginary component of the AC susceptibility is shown in Figure 3.7. From initial measurements referenced in Section 3.1 above, it was thought that the $\chi''(f)$ exhibited the characteristic response of a spin ice where the maximum $\chi''(f)$ shifts to higher frequencies with an increase in temperature. However, once more data points were acquired for $\text{Dy}_2\text{ScNbO}_7$ at lower temperatures, it becomes apparent that the imaginary component of the susceptibility deviates

from that expected for a spin ice in several ways. While there is an outward shift in frequency of the maxima, the transformation of peak shape and amplitude at increasing temperature points are dissimilar to that of known spin ices. In contrast, the peaks in the $\chi''(f)$ of $\text{Dy}_2\text{Ti}_2\text{O}_7$ are symmetrical and fairly narrow, with the peak height decreasing monotonically as the temperature increases. This is observed in both $\text{Dy}_2\text{Ti}_2\text{O}_7$ [1] and $\text{Dy}_2\text{Sn}_2\text{O}_7$ [2], which are well studied spin ice materials. The peak height of susceptibility $\chi''(f)$ of $\text{Dy}_2\text{ScNbO}_7$ initially increases at temperatures from 0.55-0.65 K, and then decreases in amplitude from 0.65-0.85 K (all of which can be seen in Figure 3.7).

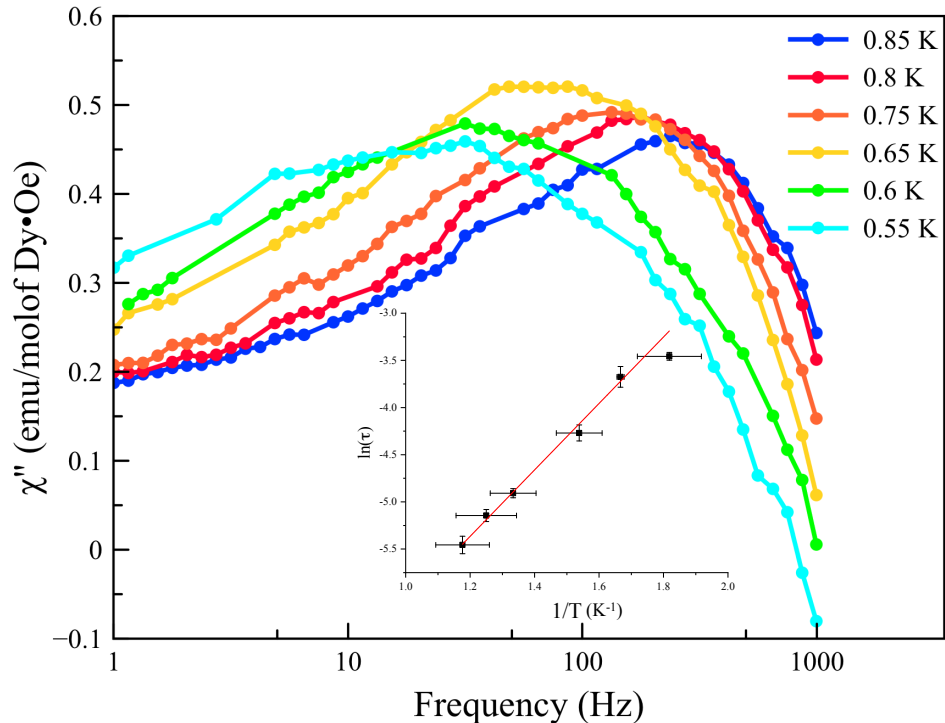


Figure 3.7: Frequency dependence of the imaginary component of the AC susceptibility of single crystal $\text{Dy}_2\text{ScNbO}_7$. Measurements were taken at several different temperatures. Inset is the graphical depiction of the Arrhenius analysis performed.

The broad nature of the peaks in $\chi''(f)$ of $\text{Dy}_2\text{ScNbO}_7$ implies a wider range of relaxation times that results from inhomogeneity in the local environment of the spins. This is consistent with the added disorder of a mixed B -site and is not unexpected. As of the writing of this thesis, the frequency dependence of the AC susceptibility of $\text{Dy}_2\text{Zr}_2\text{O}_7$ has not been reported and we are therefore unable to make a direct comparison of this particular type of measurement.

The inset in Figure 3.7 above shows the Arrhenius analysis that was performed by calculating the characteristic relaxation time, τ , from the maximal frequencies of $\chi''(f)$. Arrhenius's law is an empirical expression that describes an exponential relationship between the temperature and the rate constant of a system. Arrhenius behaviour is often used to describe the temperature dependence of chemical reaction rates, but can also be used to describe the temperature dependence of magnetic relaxation, as is relevant to our study. The rate constant values extracted from the above data can be plotted according to the following Arrhenius expression:

$$\ln(\tau) = \frac{-E_a}{R} \frac{1}{T} + \ln(A), \quad (3.2.2)$$

where R is the ideal gas constant. The resulting slope from plotting the logarithm of τ against $1/T$ gives the activation energy, E_a . In this case E_a refers to the energy scale for magnetic phenomena [1]. The slope given by the linear regression shown in Figure 3.7 gives an $E_a = 29.2 \pm 0.1$ K. When Arrhenius analysis is performed for this temperature regime in $\text{Dy}_2\text{Ti}_2\text{O}_7$ and $\text{Dy}_2\text{Zr}_2\text{O}_7$, $E_a \approx 10$ K and 8 K respectively [1], [65]. While E_a itself gives a sense of the energy scale of the system, it is interpreted in $\text{Dy}_2\text{Ti}_2\text{O}_7$ as the energy cost of flipping small spin clusters. The discrepancy between the energy scales in $\text{Dy}_2\text{Ti}_2\text{O}_7$ and $\text{Dy}_2\text{ScNbO}_7$ could be due to differences in magnetic

defect formation in the two systems. It is important to note, that while we speculate on the differences in energy scales between the two systems, the temperature dependence of τ in $\text{Dy}_2\text{Ti}_2\text{O}_7$ had been determined over a much larger temperature range than was possible to measure for $\text{Dy}_2\text{ScNbO}_7$, making direct comparisons difficult.

3.2.2 Heat Capacity

A great deal of information about the magnetism in a system can be learned by isolating the magnetic contribution to the heat capacity. In order to isolate the magnetic heat capacity, $\text{Eu}_2\text{ScNbO}_7$ (synthesized using the same ceramic technique outlined above) was used as a model for the other components of the heat capacity. Eu^{3+} is predicted to be a magnetic singlet, and as such, the heat capacity of $\text{Eu}_2\text{ScNbO}_7$ is used as a non-magnetic analogue to that of $\text{Dy}_2\text{ScNbO}_7$. Subtracting the respective heat capacities leaves only the magnetic contribution to the heat capacity remaining. There is some debate in the community regarding whether Eu^{3+} is a good candidate for a lattice standard due to possible crystal field contributions (as seen in $\text{Eu}_2\text{Ti}_2\text{O}_7$ [66]). However these concerns are not relevant over our temperature range of interest. It should also be noted that the polycrystalline form of the lattice standard was measured down to 2 K and a T^3 fit was extrapolated down to zero. These data were then subtracted from that taken for $\text{Dy}_2\text{ScNbO}_7$ to isolate the purely magnetic contribution to the heat capacity.

The heat capacity data presented in this thesis work was measured on a small pieces of the single crystal of $\text{Dy}_2\text{ScNbO}_7$ shown above in Section 3.1. Several different crystal segments were aligned along the $\langle 111 \rangle$ and $\langle 110 \rangle$ crystallographic axes. As described in Section 1.3.2, these axes are particularly relevant when investigating

pyrochlores with unknown magnetic properties and determining nature of short term correlations present within the material.

Measurements along both the $\langle 111 \rangle$ and $\langle 110 \rangle$ crystallographic directions where the temperature dependence of C_{mag}/T is shown in Figure 3.8. There is virtually no difference between the two sets of heat capacity measurements in zero applied field as is expected. Each exhibits a broad lambda-like anomaly, although the $\text{Dy}_2\text{ScNbO}_7$ anomaly is at a higher temperature (≈ 1.2 K) than that seen in analogous $\text{Dy}_2\text{Ti}_2\text{O}_7$ heat capacity measurements, and falls off almost completely by 10 K. Upon applying an increasingly large applied external magnetic field, the amplitude of the peak decreases while the temperature at which heat capacity reaches a maximum increases in a non-linear fashion. This response to an applied magnetic field implies that the feature is magnetic in origin.

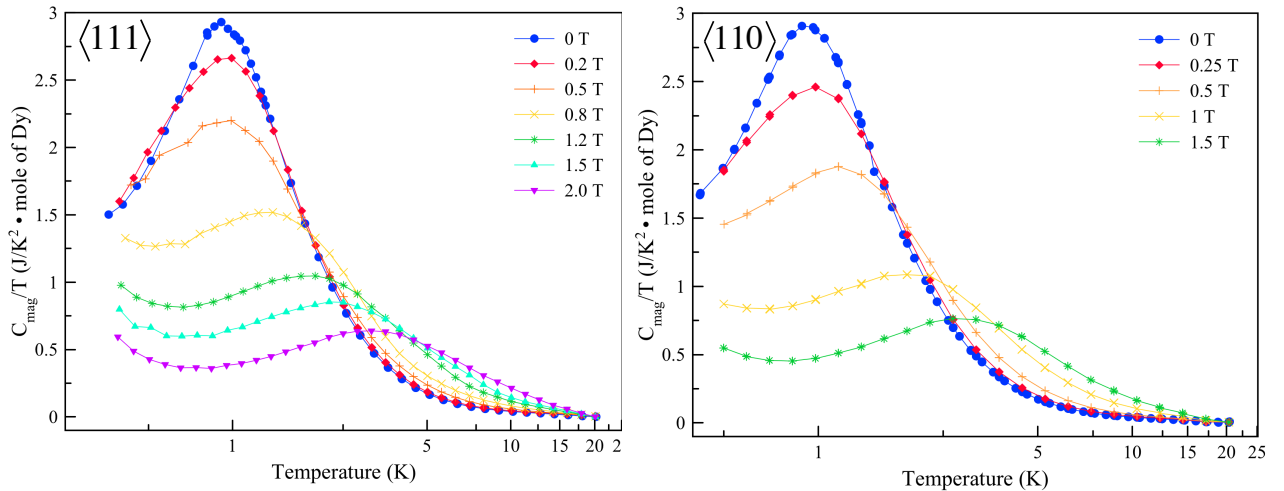


Figure 3.8: Low temperature heat capacity divided by temperature after performing a lattice subtraction. Measurements were performed on a single crystal of $\text{Dy}_2\text{ScNbO}_7$ aligned along the $\langle 111 \rangle$ (left) and $\langle 110 \rangle$ (right) crystallographic directions with varying magnetic fields. An obvious broad peak can be seen shifting right with increasing magnetic field.

Additionally, a new feature between 0.5 and 1 T develops in the form of an upturn at low temperatures. This feature appears even as the heat capacity peaks continue to shift towards higher temperatures with an increasing magnetic field. Though it is difficult to conclusively plot $C_v \cdot T^2$ vs. T^5 due to the fact that the anomaly occurs close to the minimum of our measured temperature range, it is likely that this feature is nuclear in origin. A nuclear Schottky is not unexpected as two dysprosium isotopes, ^{161}Dy and ^{163}Dy with nuclear magnetic moment, $I=5/2$ with quadrupole and hyperfine interactions as discussed in reference [67]. This supposed nuclear contribution could result in increased error in the determination of peak position used to construct the phase diagram in Figure 3.9 below.

The objective of measuring the heat capacity with a magnetic field applied along various crystallographic axes is to probe the magnetic anisotropy present within the material. Dysprosium pyrochlores tend to exhibit Ising anisotropy, which is described in Section 1.4. This is where the net magnetic moment of one tetrahedron in the crystal lattice points along the principal axis (along the $\langle 111 \rangle$ direction) as seen in Figure 1.9, described in Section 1.3.1. If Ising anisotropy were present in $\text{Dy}_2\text{ScNbO}_7$, we would expect to see signature features in the heat capacity where the field is applied along the $\langle 111 \rangle$ direction (to be expanded upon later in this section). Plotting the peak position as a function of temperature and applied magnetic field does show that there is some distinction between the magnetism along the $\langle 111 \rangle$ and the $\langle 110 \rangle$ directions. The peak position moves towards increasing temperature with an increase in applied magnetic field as can be seen in Figure 3.9 below. It should be noted that unlike what is reported for $\text{Dy}_2\text{Ti}_2\text{O}_7$, the relationship between field and temperature is non-linear. The disparity in field dependence between the $\langle 111 \rangle$ and $\langle 110 \rangle$ data

could indicate that there is some directionality to the magnetic interactions. However, this difference is small, and error in determining the peak position due to possible nuclear contributions to the heat capacity, make it difficult to definitively identify the nature of said directionality. Whether these are indicative of a mixture of Ising and some degree of paramagnetism, or some other type of magnetic exchange remains to be seen.

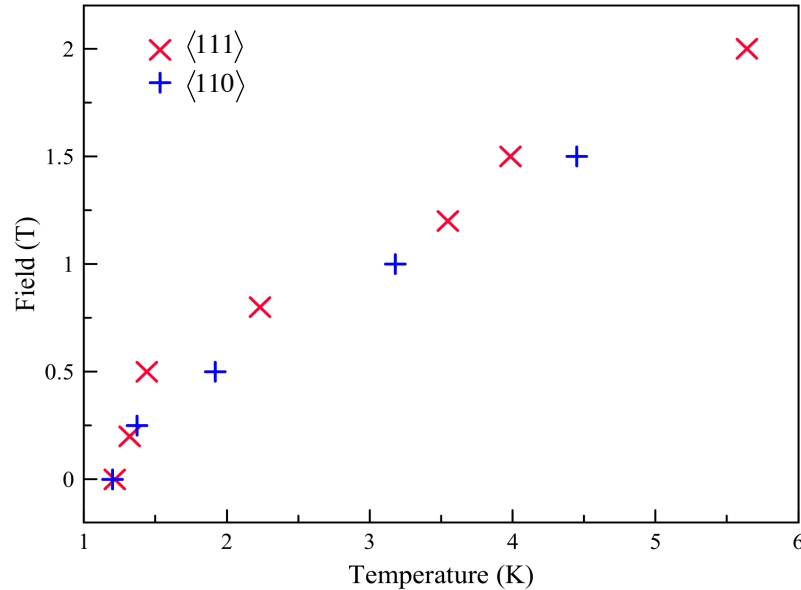


Figure 3.9: Phase diagram of the maximum heat capacities measured as a function of field and temperature along both the $\langle 111 \rangle$ and $\langle 110 \rangle$ crystallographic directions.

In fact, when comparing the heat capacity of $\text{Dy}_2\text{ScNbO}_7$ to that of $\text{Dy}_2\text{Ti}_2\text{O}_7$, the lack of Ising anisotropy becomes evident. A pyrochlore which exhibits Ising anisotropy can adopt what is known as the kagomé ice state, where the spins orient with a 1-in and 3-out configuration. The one spin oriented “in”, which is parallel to the $\langle 111 \rangle$ direction, while the remaining spins are perpendicular to the $\langle 111 \rangle$ in the kagomé lattice, where alternating layers form a pseudo-2D triangular lattice.

Evidence for this spin orientation is seen in heat capacity measurements performed on single crystals of $\text{Dy}_2\text{Ti}_2\text{O}_7$ where the applied magnetic field is along the $\langle 111 \rangle$ direction. Two distinct peaks develop at low temperatures, one being an anomaly that is present at low temperatures in the absence of an applied magnetic field (peak 1), and is thought to correspond to the spins parallel to said field. The other is a peak that develops with increasing applied field and comes to a sharp peak at 1 T (peak 2). Peak 2 is thought to correspond to the three frustrated spins that sit on the kagomé ice lattice, in the quasi-2D planes that exist as shown in Figure 1.9. The development of this additional peak can be seen on the right in Figure 3.10 below.

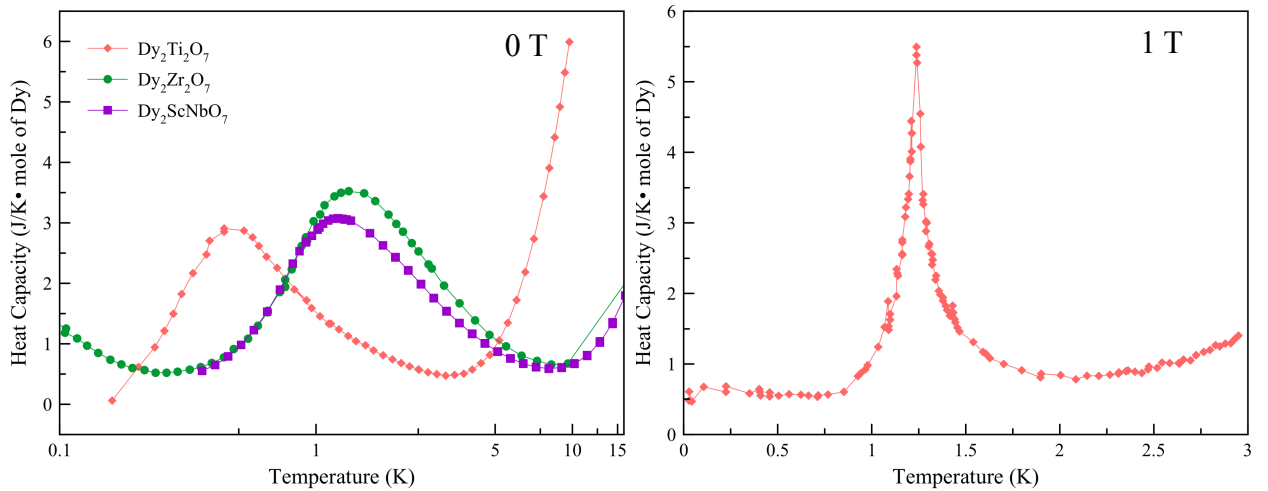


Figure 3.10: The heat capacity of $\text{Dy}_2\text{ScNbO}_7$ in zero applied magnetic field, plotted with analogous measurements for $\text{Dy}_2\text{Ti}_2\text{O}_7$ (data from [68]) and $\text{Dy}_2\text{Zr}_2\text{O}_7$ (data from [65]) (left). The second peak that forms in the heat capacity of $\text{Dy}_2\text{Ti}_2\text{O}_7$ with increasing applied magnetic field as a result of the kagomé ice phase [68]. The peak is maximal in a 1 T applied field (right).

The second peak is noticeably absent in the $\langle 111 \rangle$ heat capacity of $\text{Dy}_2\text{ScNbO}_7$. This further suggests that the predominant type of magnetic interactions are non-Ising within the system, and that no kagomé ice state forms with increasing applied

magnetic field along the $\langle 111 \rangle$ direction. In fact, the heat capacity measurements taken during this thesis work resemble the heat capacity of $\text{Dy}_2\text{Zr}_2\text{O}_7$, where we see a broad peak at ≈ 1.2 K is similar to the peak seen in zero field of $\text{Dy}_2\text{ScNbO}_7$. The zero field heat capacity of $\text{Dy}_2\text{Zr}_2\text{O}_7$, $\text{Dy}_2\text{ScNbO}_7$, and $\text{Dy}_2\text{Ti}_2\text{O}_7$ are overlaid for comparison on the left in Figure 3.10 below. It should be noted that the only heat capacity measurements for $\text{Dy}_2\text{Zr}_2\text{O}_7$ that have been reported at the time of writing this thesis are all performed on polycrystalline samples. It is therefore impossible to compare the directional dependence of the heat capacity in an applied magnetic field to that of $\text{Dy}_2\text{Ti}_2\text{O}_7$ and $\text{Dy}_2\text{ScNbO}_7$.

Heat capacity measurements can also be used to investigate the entropy of a system. The following relationship allows for the determination of the entropy from the heat capacity data via the following:

$$\Delta S = \int_{T_0}^{T_f} \frac{C_V}{T} dT, \quad (3.2.3)$$

where T_0 and T_f denote starting and end points of the interval over which the integration is performed. The magnetic contribution to the entropy can be extracted by subtraction the lattice contribution as described above, and then integrating C_{mag}/T over the measured temperature interval. The result of this for both the $\langle 111 \rangle$ and $\langle 110 \rangle$ heat capacities can be seen below in Figure 3.11. In the absence of residual entropy (as would be expected if the system adopted a long range ordered ground state), since the dysprosium cation exhibits a Kramers doublet [52], the entropy is expected to saturate at $R\ln 2$ (approximately 5.67 J/K·mol of Dy). The calculated entropy for a classical spin ice is $R(\ln 2 - 1/2\ln 3/2)$ (approximately 4.08 J/K·mole of Dy) from the Pauling entropy of a classical dipolar spin ice [28]. Both of these are

marked in black on Figure 3.11. A more detailed explanation of the calculation of these predicted residual entropy values was given in Sections 1.1 and 1.4.1.

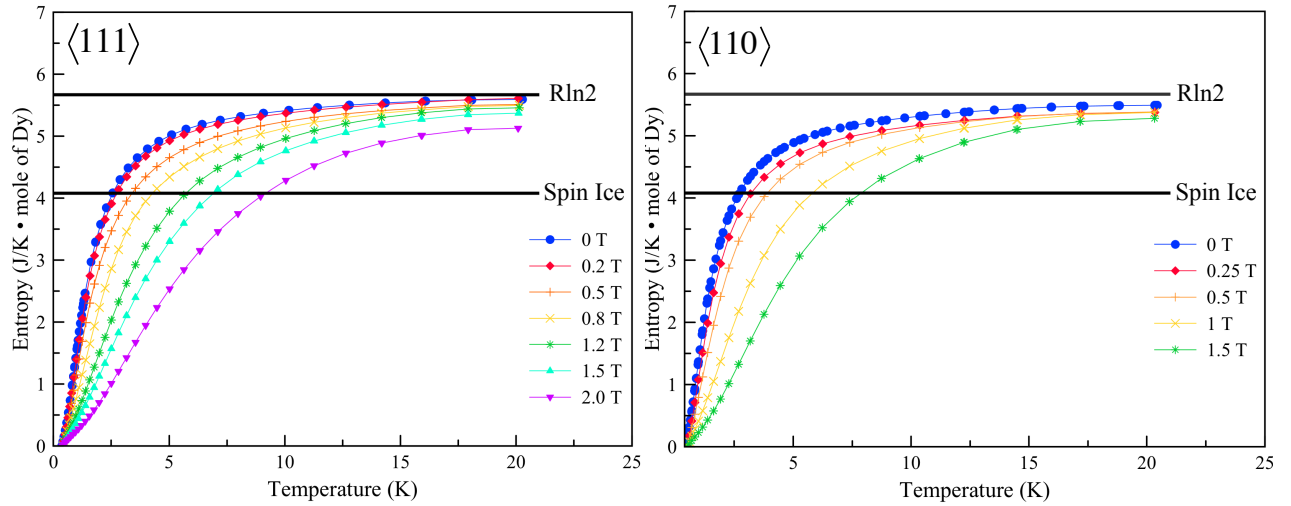


Figure 3.11: The magnetic entropy extracted from the aforementioned heat capacity with external magnetic fields applied along the $\langle 111 \rangle$ (left) and $\langle 110 \rangle$ (right) directions. The predicted entropies for both the spin ice state and the ordered state are included in black.

The entropy calculated for both sets of heat capacity data saturates to near $R\ln 2$ if the integration is taken to 20 K. However, the magnetic feature of interest in the 0 T data exists to 10 K. At the 10 K point $\approx 90\%$ of the expected entropy. In reality, this could be even lower as there is evidence to suggest low lying crystal electric fields (which will be discussed in Section 4.1) which may contribute to the entropy in this temperature regime. Regardless, the residual entropy is still much less than predicted for a spin ice.

Once again, the comparison of the entropy of $\text{Dy}_2\text{Ti}_2\text{O}_7$, $\text{Dy}_2\text{Zr}_2\text{O}_7$, and $\text{Dy}_2\text{ScNbO}_7$ assists with the interpretation of our results. The magnetic entropy of $\text{Dy}_2\text{Ti}_2\text{O}_7$ predictably adheres to the spin ice rules, saturating to ≈ 4.08 J/K-mole of Dy. $\text{Dy}_2\text{Zr}_2\text{O}_7$

on the other hand, is slightly above $R\ln 2$ (which could very well be due to scaling differences or in the lattice subtraction). These entropies are plotted in comparison to $\text{Dy}_2\text{ScNbO}_7$ in Figure 3.12 below.

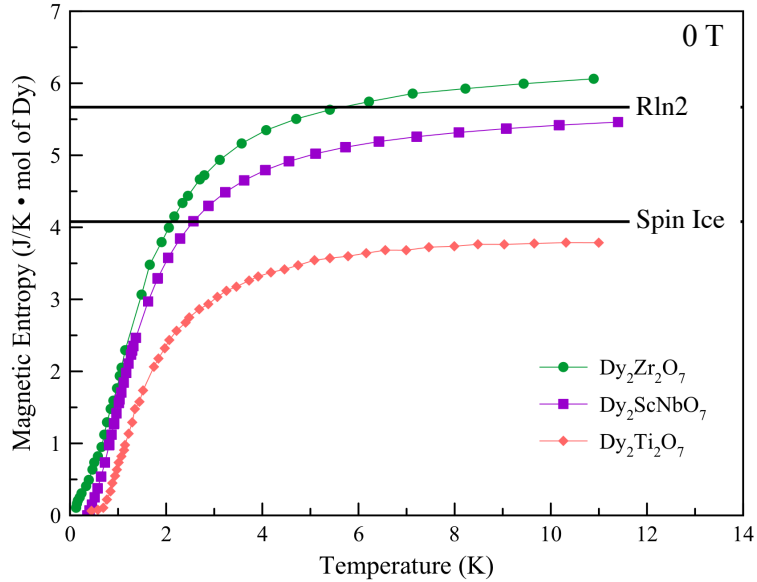


Figure 3.12: The magnetic entropy of $\text{Dy}_2\text{ScNbO}_7$ plotted with the magnetic entropies of $\text{Dy}_2\text{Ti}_2\text{O}_7$ and $\text{Dy}_2\text{Zr}_2\text{O}_7$ (data from Ramon *et al.*[65]).

Here we can see that the entropy of $\text{Dy}_2\text{ScNbO}_7$ is between the entropy of the other systems, albeit with significantly less residual entropy than expected for a spin ice, resulting in a much closer resemblance to the entropy of $\text{Dy}_2\text{Zr}_2\text{O}_7$ than that of $\text{Dy}_2\text{Ti}_2\text{O}_7$. This once again gives us further evidence that the disordered dysprosium pyrochlore does not adopt the spin ice ground state.

3.3 Muon Spin Relaxation Measurements

As previously discussed, the spin dynamics of $\text{Dy}_2\text{ScNbO}_7$ appear anomalously fast in comparison to other analogous dysprosium pyrochlores (unlike $\text{Dy}_2\text{ScNbO}_7$, are

known to exhibit the spin ice ground state), which can be seen in the AC susceptibility ($\chi''(f)$) data in Section 3.2.1. This is especially apparent when comparing to analogous $\text{Dy}_2\text{Ti}_2\text{O}_7$ T_0 data. In fact, the dynamics are so fast that they are largely outside of the frequency window available to us via AC susceptibility. In an effort to better understand the dynamics of the system, μSR was used to investigate a higher frequency window ($\approx 10^4 - 10^{12}$ Hz) as the time scale of μSR is shorter than that of AC susceptibility (which has a frequency window of $\approx 10^{-1} - 10^4$ Hz) [61]. All measurements reported in this section were performed at TRIUMF, a particle accelerator on the University of British Columbia campus located in Vancouver, BC (technical details of this technique were described in Section 2.6). The low temperature, zero field data was taken at the M15 beamline, using a dilution refrigerator cryostat. A single crystal of $\text{Dy}_2\text{ScNbO}_7$ was sliced into flat pieces and then mounted to the silver cold-finger using Apiezon grease to ensure good thermal contact. The high temperature, a 4 kG applied external field data was taken at the M20 beamline, using a helium gas flow cryostat and a low background sample holder. All data analysis was performed using Musrfit [69].

While μSR is a powerful technique in the detection of weak local magnetic fields, the study of rare earth magnetism is notoriously difficult using this technique due to extremely large internal magnetic fields. $\text{Dy}_2\text{ScNbO}_7$ has an effective Dy^{3+} magnetic moment of $10.48 \mu_B$, resulting in a fast relaxation rate. Rapid depolarization occurs and there appears to be an effectively instantaneous drop in the asymmetry as can be seen below on the left of Figure 3.13. Looking at the early time interval it can be seen that the evolution of the asymmetry is actually continuous (as seen in the inset on the left of Figure 3.13) and an attempt was made to fit this data to a simple exponential

function. Measurements were taken at various applied magnetic fields up to 4 T, and various temperatures up to 4 K. Adjusting these parameters made little difference in this rapid relaxation response. Measurements taken with zero applied magnetic field at both base temperature achievable by the DR (0.027 K) and 2 K are shown to illustrate the lack of temperature dependence. Our measurements do not provide any evidence for long range order down to low temperatures, but do demonstrate the existence of large quasi-static magnetic moments.

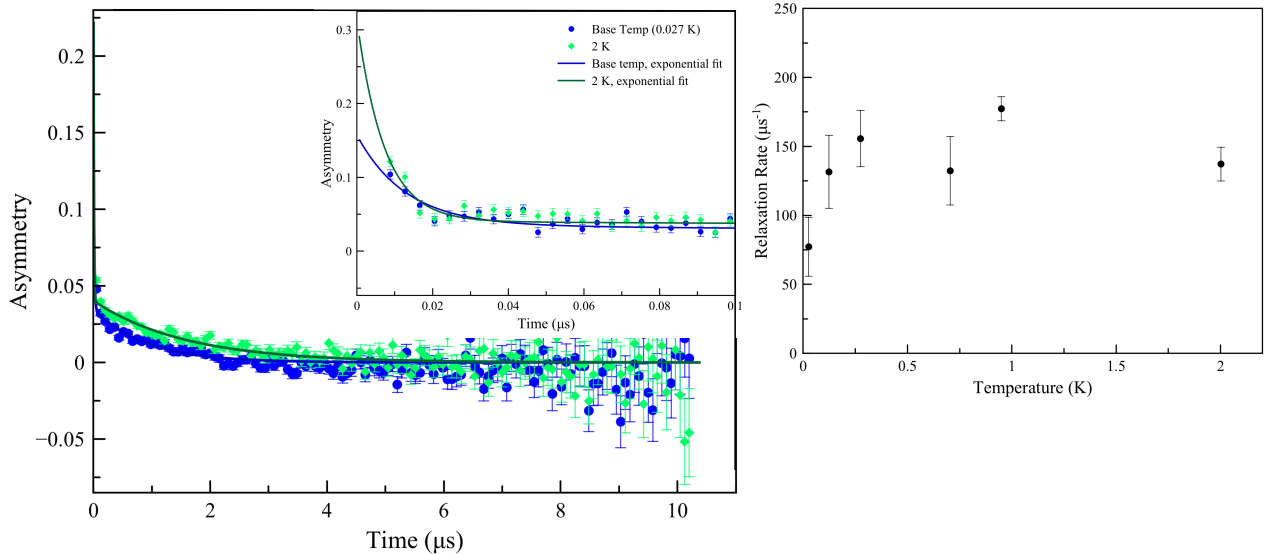


Figure 3.13: Muon spin relaxation data taken at 0.027 K (in blue) and 2 K (in red) on the M15 beamline at TRIUMF, in the absence of an applied external magnetic field. On the left the asymmetry of muon decay as a function of time is shown, with the first 0.1 μs shown in the inset. Data was fit with a simple exponential function. On the right is the relaxation rate extracted from the exponential fit function.

The asymmetry spectra were modeled using a simple exponential function of the form $a(t) = a_0 e^{-\lambda t}$ where a_0 is the amplitude of the initial asymmetry and λ is the relaxation rate. The temperature dependence of the relaxation rate is plotted on the right of Figure 3.13. It can be seen that, within error, there is no statistically

significant trend as temperature goes from 0.027-2 K. It is important to note that, while it was technically possible to model the asymmetry, the exponential was fit over a time period of $0.1 \mu\text{s}$ and parameters extracted from such a fit should be scrutinized critically.

At higher temperatures, and with a 4 kG applied longitudinal magnetic field, we had more success with identifying the relaxation of $\text{Dy}_2\text{ScNbO}_7$. While the spin dynamics remain fast between 3 and 100 K, the relaxation became slower and easier to resolve as seen in Figure 3.14 below. A much more convincing simple exponential fit was modelled to the data as can be seen over the first μs of data collected in the inset of Figure 3.14 on the left.

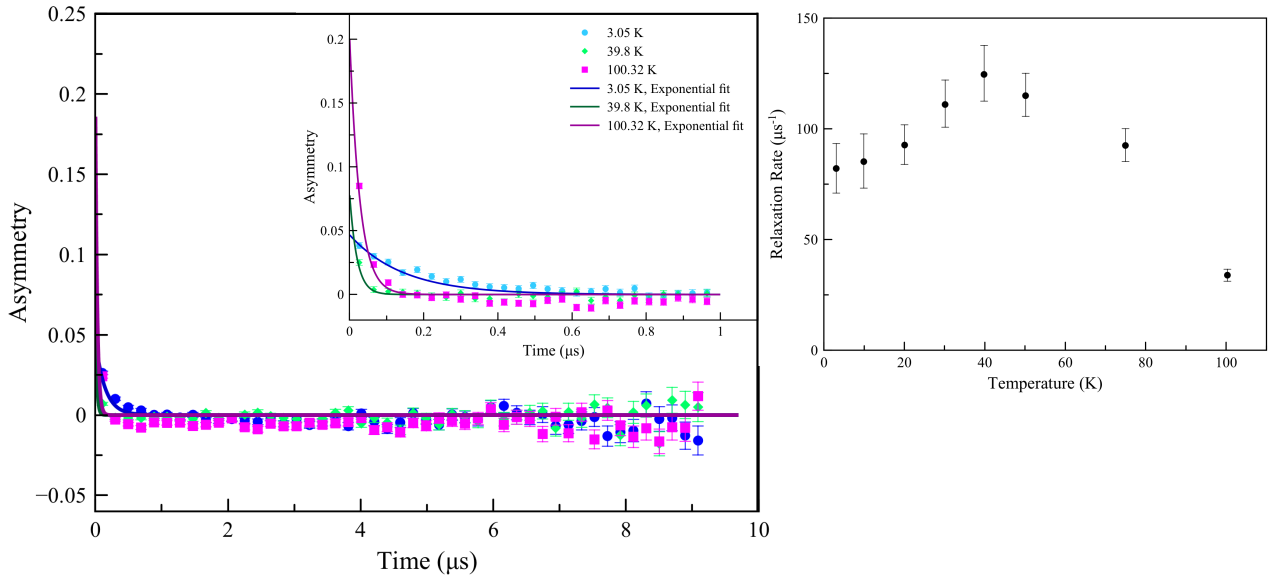


Figure 3.14: Muon spin relaxation data taken from 3-100 K in a 4 kG external applied magnetic field on the M20 beamline at TRIUMF. On the left, the asymmetry of muon decay as a function of time is shown, with the first $1 \mu\text{s}$ shown in the inset. Data was fit with a simple exponential function. On the right is the temperature dependence of the relaxation rate extracted from the exponential fit function.

The relaxation as a function of temperature is plotted on the right of Figure 3.14. Here we see an increase in relaxation with increasing temperature up to a peak value of ≈ 40 K, after which the relaxation rate decreases. It can be seen in the data on the left that the data taken at ≈ 40 K relax faster than data taken at ≈ 3 K and ≈ 100 K. This upturn in the relaxation rate very likely corresponds to a low lying, broad crystal field excitation at approximately 5 meV which corresponds to ≈ 50 K. The crystal electric field (CEF) level would affect the relaxation rate as the CEF has a direct effect on the size of the magnetic moment of the Dy^{3+} cation.

While these two features do not directly correspond due to the width of the CEF, which leaves a fairly large margin for error, making an energy scale comparison gives good agreement between the μSR and neutron scattering measurements. These CEF measurements will be discussed in more detail in Chapter 4.

3.4 General Remarks

While this project has been several years in the making, the work outlined in this chapter has resulted in the emergence of a more cohesive picture. The initial motivation of this project was to investigate a relatively unexplored dysprosium pyrochlore system and to understand how a disordered B -site would affect the ground state physics of the system. We initially thought that, like other dysprosium pyrochlores ($\text{Dy}_2\text{Ti}_2\text{O}_7$ or $\text{Dy}_2\text{Sn}_2\text{O}_7$), our material would exhibit short range order at low temperatures, adopting the spin ice ground state. However, initial physical characterization of $\text{Dy}_2\text{ScNbO}_7$ did not support this. AC susceptibility measurements showed anomalously fast spin dynamics, and DC magnetometry measurements gave a Curie-Weiss

temperature of -1.52 ± 0.02 K, indicating net antiferromagnetic interactions occurring within the sample. Additionally, heat capacity measurements yielded a magnetic entropy that exceeded that predicted for a spin ice, while still falling short of the expected $R \ln 2$. Early diffuse neutron scattering experiments on samples prepared with naturally occurring dysprosium were difficult to conclusively model.

The body of this thesis work is comprised of our attempts to resolve the conflict between our expectations for a dysprosium pyrochlore and the results of characterizing the mixed B -site $\text{Dy}_2\text{ScNbO}_7$. Where other materials in the ScNb family like $\text{Nd}_2\text{ScNbO}_7$ [70], and $\text{Gd}_2\text{ScNbO}_7$ [71], all show similarities to their parent compounds (those of which have no disorder on the B -site), this is not at all the case with $\text{Dy}_2\text{ScNbO}_7$. Other “parent” dysprosium pyrochlores, including $\text{Dy}_2\text{Ti}_2\text{O}_7$, $\text{Dy}_2\text{Sn}_2\text{O}_7$, and $\text{Dy}_2\text{Ge}_2\text{O}_7$ all exhibit spin ice physics - indicating that the spin ice state is resistant to chemical perturbation (particularly those which result in differing lattice parameters). However, the spin ice state appears to be fragile in the presence of a disordered B -site.

The temperature dependence of the real component of the AC susceptibility shows a glassy response to change in frequency - similar to that of the disordered $\text{Dy}_2\text{Zn}_2\text{O}_7$. However, performing a quantitative analysis shows that the frequency dependence is much greater than expected for a conventional spin glass. Furthermore, an Arrhenius analysis shows the energy barrier of relaxation in $\text{Dy}_2\text{ScNbO}_7$ is 2-3 times larger than that of either $\text{Dy}_2\text{Ti}_2\text{O}_7$ [72], or $\text{Dy}_2\text{Zr}_2\text{O}_7$ [65]. This could indicate that excitations in the mixed B -site pyrochlore differ from that of either comparison system.

While the μSR does not indicate long range order down to lowest temperatures, we see that out to 20 K, our magnetic entropy extracted from heat capacity measurements

saturates to $R\ln 2$, indicating a lack of residual entropy tied up in a disordered ground state. While at first these two results seem to contradict each other, we must consider the fact that the magnetic contribution to the heat capacity is located primarily below 10 K. At this temperature, the magnetic entropy has not fully recovered $R\ln 2$ entropy. This, in combination with several low-lying crystal field excitations that could be contributing to the heat capacity, could result in an over estimation of the magnetic entropy. This could mean that there could be more residual entropy in the ground state of $\text{Dy}_2\text{ScNbO}_7$ than is obvious from these data shown in Figure 3.11. The idea that Ising interactions are not dominant in this sample comes from the lack of directional dependence seen in heat capacity measurements where an external magnetic field is applied along the $\langle 111 \rangle$ and $\langle 110 \rangle$ axes of the crystal. Along the $\langle 111 \rangle$, we expect to see a second peak at low temperatures form as a result of the kagomé ice state which is completely absent in our measurements.

The result of this work seems to indicate that not only does the disordered B -site not exhibit a spin ice ground state, but that the mixed B -site seems to destroy the Ising anisotropy expected for this dysprosium containing species. There could still be clusters of spin ice present within the material in which the net moment of that region remains Ising, but we are unable to irrefutably confirm this at this time. As it appears that this disorder dismantles the Ising state, this result could be extremely relevant to other pyrochlore systems that exhibit disorder of any kind including mixed A - or B -sites, pyrochlores with non-oxygen stoichiometry, or those with stuffing. The Ising anisotropy or lack thereof is discussed further in Chapter 4.

Chapter 4

Preliminary Neutron Scattering and Future Work

4.1 Crystal Electric Field Measurements

While there have been several neutron scattering/spectroscopy experiments performed in an effort to reveal the ground state physics of $\text{Dy}_2\text{ScNbO}_7$, the interpretation and analysis of these data is largely outside of the scope of this thesis and can be found in the doctoral thesis of Cole Mauws from the University of Manitoba [73]. However, it is prudent to briefly discuss a few qualitative observations of the low energy crystal electric field (CEF) data. Inelastic neutron scattering measurements were performed on the Wide Angular-Range Chopper Spectrometer (ARCS), off of the SNS at ORNL.

A difficulty in performing neutron scattering experiments on any material containing naturally occurring Dy^{3+} is the large absorption cross section of 994 barns ($1 \text{ barn} = 1 \times 10^{-24} \text{ cm}^2$), meaning that scattering neutrons off of a dysprosium containing species to be difficult, as most incident neutrons are absorbed by the sample. In

comparison, the other ions present in the sample of absorption cross section of 27.5, 1.15, and 0.00019 barns for Sc, Nb, and O respectively [74]. It is therefore important to consider the portion of the beam that actually passes through the sample. The percentage of transmitted beam is

$$\frac{I}{I_0} = e^{-N\sigma x}, \quad (4.1.1)$$

with I_0 and I the incident and transmitted intensities respectively, N is the number of nuclei per unit volume, σ_a is the neutron absorption cross section, and x is the thickness of the sample [75]. From this expression, we reduced the effect of neutron absorption by dysprosium in two different ways. The first was by loading the polycrystalline samples into an annular can to reduce the thickness of the sample, and increase the percentage of the incident beam that is transmitted. The second way in which we attempted to reduce neutron absorption was by synthesizing an isotopically enriched sample, $^{162}\text{Dy}_2\text{ScNbO}_7$ (prepared according to the synthesis described in Section 3.1). In comparison to naturally occurring dysprosium, ^{162}Dy has a scattering cross section of 194 barns [74]. A description of the instrumentation and specifics of ARCS can be found in reference [49].

The primary finding that will be discussed in this section is the dramatic difference in the low energy excitations of $\text{Dy}_2\text{ScNbO}_7$ (as seen in Figure 4.2 and $\text{Dy}_2\text{Ti}_2\text{O}_7$ (seen in Figure 4.1). We see this in the CEF measurements of $\text{Dy}_2\text{Ti}_2\text{O}_7$ where the first excited state is at ≈ 20 meV seen in the figure below.

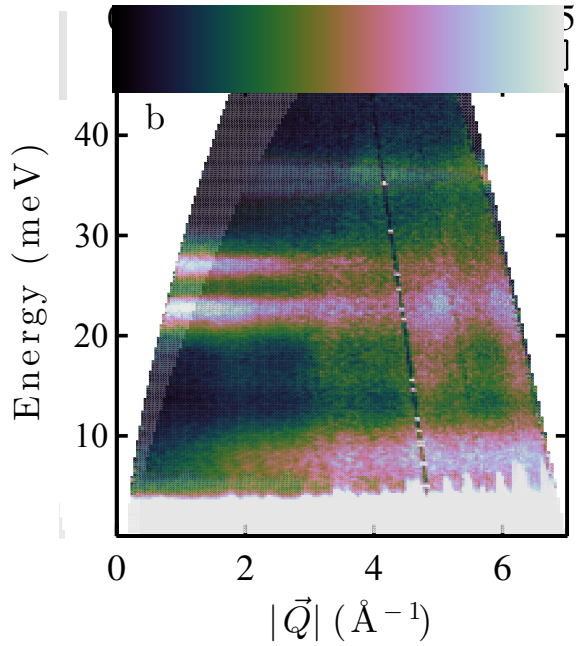


Figure 4.1: Inelastic neutron spectrum of polycrystalline $\text{Dy}_2\text{Ti}_2\text{O}_7$ at $T = 5$ K. Intensities are represented in colormaps of arbitrary scale. Excitations with highest intensity at lowest momentum transfers $|\mathbf{Q}|$ are magnetic excitations from the CEF ground state to excited CEF states. Intensities at large $|\mathbf{Q}|$ are due to scattering by phonons. Figure used with permission from [76].

In contrast, the low energy CEF of $^{162}\text{Dy}_2\text{ScNbO}_7$ shows a broad, low energy feature centered around ≈ 5 meV as seen in Figure 4.2. This feature is consistent with some of our earlier measurements (the μSR data seen in Figure 3.14 in particular). However, this is quite unexpected for a dysprosium pyrochlore.

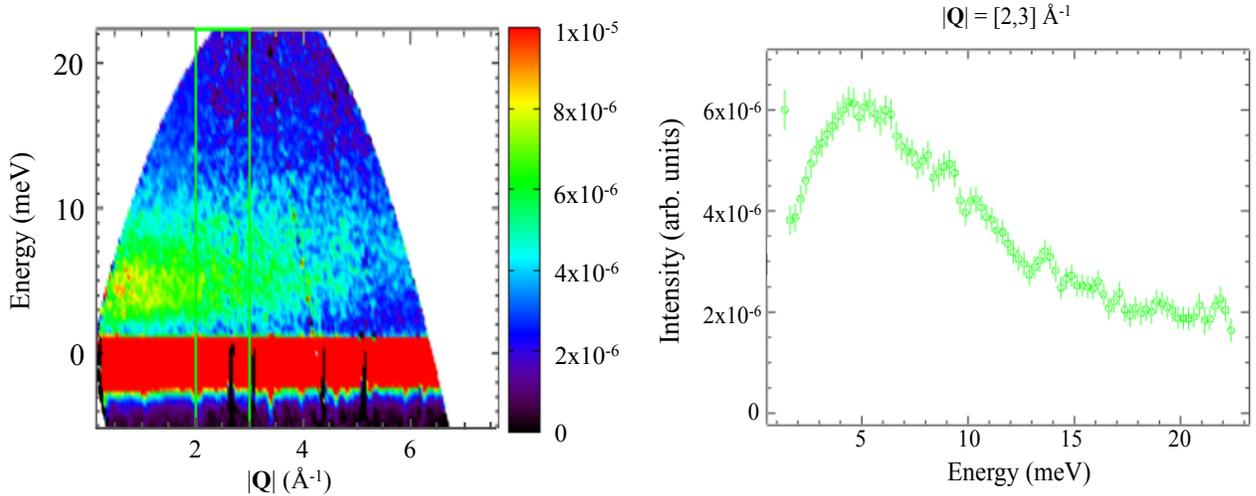


Figure 4.2: Inelastic neutron scattering data of polycrystalline $^{162}\text{Dy}_2\text{ScNbO}_7$ at $T = 5$ K (left) and CEF of $^{162}\text{Dy}_2\text{ScNbO}_7$ using $E_i=25$ meV, and $T = 5$ K with $\mathbf{Q}=[2,3]$ (right).

It is our working theory that the disorder of the B -site (where there is not a uniform distribution of Sc^{3+} and Nb^{5+} surrounding the A -site Dy^{3+} cation) results in many different CEF bands of slightly different energies that overlap to form a broad peak. Additionally, we believe that the disorder of the B -site destroys the Ising anisotropy - which results in such drastic differences between the CEF measurements of the two systems shown above.

4.2 Future Work

Although the research performed and written about in this thesis has shed some light on the mystery that is $\text{Dy}_2\text{ScNbO}_7$, there remain many loose ends left to tie up in the investigation of this material. Diffuse neutron scattering measurements have been taken using polarized neutrons in an effort to resolve between the chemical and

magnetic disorder of the system. The analysis of these results is outside of the scope of this thesis and can be found in the doctoral thesis written by Cole Mauws from the University of Manitoba [73]. Qualitatively, these data are also not what we expect for a spin ice. Additional inelastic neutron scattering measurements would also be necessary to fully understand $\text{Dy}_2\text{ScNbO}_7$. In order to attempt modelling the crystal field data higher energy crystal field levels are required.

Another fruitful direction in which to take this project would be to use the parameters outlined in Section 3.1 and attempt to grow a single crystal of isotopically enriched $^{162}\text{Dy}_2\text{ScNbO}_7$. This crystal could then be used to perform diffuse neutron scattering with polarized neutrons in an effort to fully characterize the magnetic ground state of the system.

While the polycrystalline, isotopically enriched, $^{162}\text{Dy}_2\text{ScNbO}_7$ has been prepared for neutron scattering measurements, it would be useful to perform some bulk measurements, particularly heat capacity in order to confirm that the low temperature feature is nuclear in origin. At the very least, bulk measurements (both heat capacity and AC susceptibility) down to dilution refrigerator temperatures are required in an effort to further study the low temperature behaviour of the system and determine the origin of low temperature features beyond our current conjecture.

Finally, probing higher temperature regions of the bulk properties of $\text{Dy}_2\text{ScNbO}_7$ could also prove interesting. In the absence of Ising anisotropy, the temperature dependence of the relaxation taken from our AC susceptibility measurements is likely very different from that of $\text{Dy}_2\text{Ti}_2\text{O}_7$. Higher temperature measurements would also serve as a way to understand how higher energy crystal energy levels affect the bulk properties of the system.

Chapter 5

Conclusion

Disorder has been studied by physicists and chemists for hundreds of years. More recently, we are able to use precise heat capacity measurements to extract the macroscopic entropy of a system in order to quantify the disorder of a microscopic system. This study aimed to investigate the effect of disorder in a well-known crystalline lattice referred to as the pyrochlore. With the elemental composition $A_2B_2O_7$, this bipartite, corner-sharing, tetrahedral lattice is an excellent model for the study of magnetic interactions in the face of geometric frustration. Frustration in this context arises when geometric lattice constraints do not allow for competing interactions to be simultaneously satisfied and therefore adopt exotic ground states. Of particular relevance to this study are dysprosium pyrochlores ($Dy_2B_2O_7$). Due to their easy axis anisotropy and ferromagnetic exchange interactions, Dy-pyrochlores typically behave as dipolar, or classical spin ices - with entropy analogous to water ice. In order to determine the effect of disorder in Dy-pyrochlores, a stoichiometric mixture of Sc^{3+}/Nb^{5+} was used to occupy the B -site of the pyrochlore lattice.

The synthesis and crystal growth of Dy_2ScNbO_7 was accomplished in previously

unpublished work, and although $\text{Dy}_2\text{ScNbO}_7$ lays on the edge of stability, structural characterization confirmed that the system did indeed adopt the pyrochlore structure. Preliminary physical characterization results showed that, unlike analogous Dy-pyrochlores, $\text{Dy}_2\text{ScNbO}_7$ has net antiferromagnetic interactions, faster spin dynamics than $\text{Dy}_2\text{Ti}_2\text{O}_7$, or $\text{Dy}_2\text{Sn}_2\text{O}_7$, and reduced residual entropy compared to $\text{Dy}_2\text{Ti}_2\text{O}_7$. None of these results indicate the predicted spin ice ground state, requiring further investigation of the mixed B -site pyrochlore. We considered two comparison materials in $\text{Dy}_2\text{Ti}_2\text{O}_7$, and $\text{Dy}_2\text{Zr}_2\text{O}_7$ as examples of the least to most disordered pyrochlore lattices (as $\text{Dy}_2\text{Zr}_2\text{O}_7$ adopts the defect fluorite structure).

Our work began with performing AC susceptibility measurements on a fragment of single crystal $\text{Dy}_2\text{ScNbO}_7$. The temperature dependence of the susceptibility showed what is commonly considered to be a glassy response, although quantitative analysis of these data showed that the frequency dependence is much more dramatic than for conventional spin glasses. An Arrhenius analysis was performed on the frequency dependence of the imaginary susceptibility and it was found that the energy barrier of the material was larger than for either of our comparison Dy-pyrochlores. Heat capacity measurements along the $\langle 111 \rangle$, and $\langle 110 \rangle$ were similar to each other, with a complete absence of signature peaks that would indicate a kagomé ice state as is seen for $\text{Dy}_2\text{Ti}_2\text{O}_7$. The heat capacity measurements were the first data taken that alluded to the lack of Ising anisotropy within our system.

Muon spin relaxation measurements were performed, and analysis was attempted. However, as the moment of Dy^{3+} is so large, acquiring a signal was difficult. The mixed B -site pyrochlore relaxed so fast that extracting a characteristic relaxation time at low (dilution refrigerator) temperatures in the absence of an applied magnetic

field was difficult. Finally, crystal electric field measurements obtained using inelastic neutron scattering confirmed that the system does indeed lack Ising anisotropy. The disordered B -site of $\text{Dy}_2\text{ScNbO}_7$ appears to result in many nearly degenerate low-lying crystal fields that form one broad peak at ≈ 5 meV. This feature was confirmed in the μSR measurements performed at temperatures of an analogous energy scale in a 4 kG applied magnetic field.

While the actual ground state of $\text{Dy}_2\text{ScNbO}_7$ remains unknown, it has become clear that the disordered B -site destroys the single ion anisotropy of the dysprosium cation. From the heat capacity and inelastic neutron scattering we see that the system is not Ising, nor does it have ferromagnetic exchange interactions. These two characteristics render $\text{Dy}_2\text{ScNbO}_7$ to be unique from other Dy-pyrochlores. Further investigation is required to elucidate the magnetic ground state of this system as described in detail in Section [4.2](#).

Bibliography

- [1] J. Snyder, B. G. Ueland, J. S. Slusky, H. Karunadasa, R. Cava, and P. Schiffer. Low-temperature spin freezing in the $\text{Dy}_2\text{Ti}_2\text{O}_7$ spin ice. *Physical Review B*, 69(064414), 2004.
- [2] Kazuyuki Matsuhira, Makoto Wakeshima, Yukio Hinatsu, Chihiro Sekine, Carely Paulsen, Toshiro Sakakibara, and Seishi Takagi. Slow dynamics of dypyrochlore oxides $\text{Dy}_2\text{Sn}_2\text{O}_7$ and $\text{Dy}_2\text{Ir}_2\text{O}_7$. *Journal of Physics: Conference Series*, 320(1), 2011.
- [3] Alannah M. Hallas, Jonathan Gaudet, and Bruce D. Gaulin. Experimental insights into the ground-state selection of quantum XY pyrochlores. *Annual Review of Condensed Matter Physics*, 9:105–124, 2017.
- [4] Peter J. Mohr, Barry N. Taylor, and David B. Newell. CODATA recommended values of the fundamental physical constants: 2010. *Reviews of Modern Physics*, 83, 2012.
- [5] J. Beringer *et al.* Review of particle physics. *Physical Review D*, 86(010001), 2012.

-
- [6] Rudolf Clausius and Walter R. Browne. *The Mechanical Theory of Heat*. London: Macmillan, 1879.
- [7] Mariana Sanchez and Roger Bowley. *Introductory Statistical Mechanics*. Clarendon Press Oxford, second edition, 1999.
- [8] Thomas Engel and Philip Reid. *Thermodynamics, Statistical Thermodynamics, and Kinetics*. Pearson Education, Inc, fourth edition, 2010.
- [9] Ken A. Dill and Sarina Bromburg. *Molecular Driving Forces: Statistical Thermodynamics in Biology, Chemistry, Physics, and Nanoscience*. Garland Science, Taylor Francis Group, second edition, 2010.
- [10] Andrew Cooksy. *Thermodynamics, Statistical Thermodynamics, Kinetics*. Pearson Education, Inc, 2014.
- [11] Linus Pauling. The structure and entropy of ice and other crystals with some randomness of atomic arrangement. *Journal of American Chemical Society*, 57(12):2680–2684, 1935.
- [12] Jason S. Gardner, Michel J. P. Gingras, and John E. Greedan. Magnetic pyrochlore oxides. *Reviews of Modern Physics*, 83(53), 2010.
- [13] William Gilbert. *On the loadstone and magnetic bodies and on The great magnet the earth*. Bernard Quaritch, 1893.
- [14] Neil W. Ashcroft and N. David Mermin. *Solid State Physics*. Saunders College Publishing, 1976.

-
- [15] B. D. Cullity and C. D. Graham. *Introduction to Magnetic Materials*. IEEE Press, second edition, 2009.
- [16] Daniel Fleisch. *A Student's Guide to Maxwell's Equations*. Cambridge University Press, first edition, 2008.
- [17] J. J. Sakurai and Jim Napolitano. *Modern Quantum Mechanics*. Addison-Wesley, second edition, 1994.
- [18] David J. Griffiths. *Introduction to Quantum Mechanics*. Cambridge University Press, second edition, 2005.
- [19] Robert M. White. *Quantum Theory of Magnetism: Magnetic Properties of Materials*. Springer, third edition, 2007.
- [20] John T. Chalker. *Introduction to Frustrated Magnetism*, chapter 1. Springer, 2011.
- [21] J. A. Mydosh. *Spin Glasses: an experimental introduction*. Taylor Francis Inc., 1993.
- [22] P. W. Anderson. Resonating valence bonds: A new kind of insulator. *Materials Research Bulletin*, 8:153–160, 1972.
- [23] P. W. Anderson. Ordering and antiferromagnetism in ferrites. *Physical Review Letters*, 102(4), May 1956.
- [24] C. R. Wiebe and A. M. Hallas. Frustration under pressure: Exotic magnetism in new pyrochlore oxides. *APL Materials*, 3(0415189), 2015.

- [25] N. P. Raju, M. Dion, M. J. P. Gingras, T. E. Mason, and J. E. Greedan. Transition to long-range magnetic order in the highly frustrated insulating pyrochlore antiferromagnet $\text{Gd}_2\text{Ti}_2\text{O}_7$. *Physical Review B*, 59(22), 1999.
- [26] J. N. Reimers, J. E. Greedan, and M. Sato. The crystal structure of the spin-glass pyrochlore $\text{Y}_2\text{Mo}_2\text{O}_7$. *Journal of Solid State Chemistry*, 72(2), 1988.
- [27] H. J. Silverstein, K. Fritsch, F. Flicker, A. M. Hallas, J. S. Gardner, Y. Qiu and G. Ehlers, A. T. Savici, Z. Yamani, K. A. Ross, B. D. Gaulin, M. J. P. Gingras, J. A. M. Paddison, K. Foyevtsova, R. Valenti, F. Hawthorne, C. R. Wiebe, and H. D. Zhou. Novel liquid-like correlations in single crystalline $\text{Y}_2\text{Mo}_2\text{O}_7$: an unconventional spin glass. *Physical Review B*, 89(054433), 2014.
- [28] A. P. Ramirez, A. Hayashi, R. J. Cava, R. Siddharthan, and B. S. Shastry. Zero-point entropy in the “spin ice”. *Nature*, 399:333–335, 1999.
- [29] M. J. Harris, S. T. Bramwell, D. F. McMorrow, T. Zeiske, and K. W. Godfrey. Geometric frustration in the ferromagnetic pyrochlore $\text{Ho}_2\text{Ti}_2\text{O}_7$. *Physical Review Letters*, 79(13), 1997.
- [30] Hiroki Kadowaki, Yoshinobu Ishii, Kazuyuki Matsuhira, and Yukio Hinatsu. Neutron scattering study of dipolar spin ice $\text{Ho}_2\text{Sn}_2\text{O}_7$: Frustrated pyrochlore magnet. *Physical Review B*, 65(144421), 2002.
- [31] H. D. Zhou, C. R. Wiebe, J. A. Janik, L. Balicas, Y. J. Yo, Y. Qui, J. R. D. Copley, and J. S. Gardner. Dynamic spin ice: $\text{Pr}_2\text{Sn}_2\text{O}_7$. *Physical Review Letters*, 101(227204), 2008.

- [32] Y. Tokiwa, J. J. Ishikawa, S. Nakatsuji, and P. Gegenwart. Quantum criticality in a metallic spin liquid. *Nature Materials*, 13:356–359, 2014.
- [33] R. Moessner and J. T. Chalker. Properties of a classical spin liquid: The heisenberg pyrochlore antiferromagnet. *Physical Review Letters*, 80(13), 1998.
- [34] M. B. Sanders, J. W. Krizan, K. W. Plumb, T. M. McQueen, and R. J. Cava. $\text{NaSrMn}_2\text{F}_7$, $\text{NaCaFe}_2\text{F}_7$, and $\text{NaSrFe}_2\text{F}_7$: novel single crystal pyrochlore antiferromagnets. *Journal of Physics: Condensed Matter*, 29(4), 2016.
- [35] S. Zouari, R. Ballou, A. Cheikh-Rouhou, and P. Strobel. Synthesis and structure of new pyrochlore-type oxides $\text{Ln}_2\text{ScNbO}_7$ ($\text{Ln} = \text{Pr, Nd, Eu, Gd, Dy}$). *Materials Letters*, 62(21-22), August 2008.
- [36] S. J. Gomez, P. M. Sarte, M. Zelensky, A. M. Hallas, B. A. Gonzalez, K. H. Hong, J. Pace, S. Calder, M. B. Stone, Y. Su, E. Feng, M. D. Le, C. Stock, J. P. Attfield, S. D. Wilson, C. R. Wiebe, and A. A. Aczel. Absence of moment fragmentation in the mixed B-site pyrochlore $\text{Nb}_2\text{GaSbO}_7$. *Physical Review B*, 103(214419), 2021.
- [37] P. M. Sarte, K. Cruz-Kan, B. R. Ortiz, K. H. Hong, M. M. Bordelon, D. Reig i Plessis, M. Lee, E. S. Choi, M. B. Stone, S. Calder, D. M. Pajerowski, L. Mangin-Thro, Y. Qiu, J. P. Attfield, S. D. Wilson, C. Stock, H. D. Zhou, A. M. Hallas, J. A. M. Paddison, A. A. Aczel, and C. R. Wiebe. Dynamical ground state in the xy pyrochlore $\text{Yb}_2\text{GaSbO}_7$. *NPJ Quantum Materials*, 6(42), 2021.

- [38] Theo Hahn, editor. *International tables for crystallography. Volume A, Space-Group Symmetry*. Kluwer Academic, 2002.
- [39] Brenden J. Kennedy, Brett A. Hunter, and Christopher J. Howard. Structural and bonding trends in tin pyrochlore oxides. *Journal of Solid State Chemistry*, 130(SC977277):58–65, 1997.
- [40] C. Mauws, A. M. Hallas, G. Sala, A. A. Aczel, P. M. Sarte, J. Gaudet, D. Ziat, J. A. Quilliam, J. A. Lussier, M. Beringer, H. D. Zhou, A. Wildes, M. B. Stone, D. Abernathy, G. M. Luke, B. D. Gaulin, and C. R. Wiebe. Dipolar-octupolar Ising antiferromagnetism in $\text{Sm}_2\text{Ti}_2\text{O}_7$. *Physical Review B*, 98(100401), 2018.
- [41] T. Fennell, O. A. Petrenko, B. Fak, S. T. Bramwell, M. Enjalran, T. Yavors'kii, M. J. P. Gingras, R. G. Melko, and G. Balakrishnan. Neutron scattering investigation of the spin ice state in $\text{Dy}_2\text{Ti}_2\text{O}_7$. *Physical Review B*, 70(134408), 2004.
- [42] Byron C. den Hertog and Michel J. P. Gingras. Dipolar interactions and origin of spin ice in Ising pyrochlore magnets. *Physical Review Letters*, 84(15), 2000.
- [43] John. E. Greedan. Geometrically frustrated magnetic materials. *Journal of Materials Chemistry*, 11(1):37–53, 2001.
- [44] P.A.M Dirac. Quantized singularities in the electromagnetic field. *Proceedings of the Royal Society of London A*, 133(69), 1931.
- [45] Claudio Castelnovo, Roderich Moessner, and Shivaji L. Sondhi. Magnetic monopoles in spin ice. *Nature*, 451:42–45, 2007.

- [46] H. D. Zhou, J. G. Cheng, A. M. Hallas, C. R. Wiebe, G. Li, L. Balicas, J. S. Zhou, J. B. Goodenough, J. S. Gardener, and E. S. Choi. Chemical pressure effects on pyrochlore spin ice. *Physical Review Letters*, 108(207206), 2021.
- [47] Francesco Maria Grimaldi. *Physico-Mathesis De Lumine, Coloribus, Et Iride, Aliisque Adnexis Libri Duo*. Kessinger Publishing LLC, 1665.
- [48] Philip Hofmann. *Solid State Physics*. Wiley-VCH, second edition, 2015.
- [49] Wide angular-range chopper spectrometer, <https://neutrons.ornl.gov/arcs>.
- [50] Yurii A. Izyumov and Ruslan P. Ozerov. *Magnetic Neutron Diffraction*. Plenum Press, 1970.
- [51] Yu. A. Izyumov, V. E. Naish, and R. P. Ozerov. *Neutron Diffraction of Magnetic Materials*. Springer US, 1991.
- [52] C. Kittel. *Introduction to Solid State Physics*. Wiley and Sons, 8th edition, 1996.
- [53] Aaron Kraft, Christoph Rupprecht, and Yau-Chuen Yam. *Superconducting Quantum Interference Device (SQUID)*. UBC Physics, 2017.
- [54] Quantum Design. *Magnetic Property Measurement System: AC Option User's Manual*, second edition, November 1999.
- [55] M. Buchner, K. Hfler, B. Henne, V. Net, and A. Ney. Tutorial: Basic principles, limits of detection, and pitfalls of highly sensitive squid magnetometry for nanomagnetism and spintronics. *Journal of Applied Physics*, 124(161101), 2018.
- [56] Steven W. Van Sciver. *Helium Cryogenics*, volume second. Springer, 2021.

- [57] Thomas Engel and Philip Reid. *Thermodynamics, Statistical Thermodynamics, Kinetics*. Pearson, third edition, 2012.
- [58] David Chandler. *Introduction to Modern Statistical Mechanics*. Oxford University Press, 1987.
- [59] Quantum Design. *Physical Property Measurement System: Heat Capacity Option User's Manual*, 11th edition, January 2004.
- [60] J. H. Brewer and R. Cywinski. μ SR: an introduction. In S. L. Lee, S. H. Kilcoyne, and R. Cywinski, editors, *Muon Science: Muons in Physics, Chemistry and Materials*, Proceedings of the Fifty First Scottish Universities Summer School in Physics. Taylor Francis and Group, 1998.
- [61] Jeff E. Sonier. Muon spin muon spin rotation/relaxation/resonance (μ sr), April 2002.
- [62] G. H. Eaton and S. H. Kilcoyne. Muon production: past, present, and future. In S. L. Lee, S. H. Kilcoyne, and R. Cywinski, editors, *Muon Science: Muons in Physics, Chemistry and Materials*, Proceedings of the Fifty First Scottish Universities Summer School in Physics. Taylor Francis and Group, 1998.
- [63] Alain Yaouanq and Pierre Dalmas De Réotier. *Muon Spin Rotation, Relaxation and Resonance: Applications to Condensed Matter*. Oxford University Press, 2011.
- [64] Y. J. Uemura. μ SR relaxation function in magnetic materials. In S. L. Lee, S. H. Kilcoyne, and R. Cywinski, editors, *Muon Science: Muons in Physics,*

Chemistry and Materials, Proceedings of the Fifty First Scottish Universities Summer School in Physics. Taylor Francis and Group, 1998.

- [65] J. G. A. Ramon, C. W. Wang L. Ishida, P. L. Bernardo, M. M. Leite, F. M. Vichi, J. S. Gardener, and R. S. Freitas. Absence of spin-ice state in the disordered fluorite $\text{Dy}_2\text{Zr}_2\text{O}_7$. *Physical Review B*, 99(214442), 2019.
- [66] P. Dasgupta, Y. M. Jana, A. Nag Chattopadhyay, R. Higashinaka, Y. Maeno, and D. Ghosh. Low-temperature measurements of magnetic susceptibility and specific heat of $\text{Eu}_2\text{Ti}_2\text{O}_7$ —an xy pyrochlore. *Journal of Physics and Chemistry of Solids*, 68, 2007.
- [67] P. Henelius, T. Lin, M. Enjalran, Z. Hao, J. Altosaar, F. Flicker, T. Yavors'kii, and M. J. P. Gingras. Refrustration and competeing orders in the prototypical $\text{Dy}_2\text{Ti}_2\text{O}_7$ spin ice material. *Physical Review B*, 93(024402), 2016.
- [68] Ryuji Higashinaka, Hideto Fukazawa, Kazuhiko Deguchi, and Yoshiteru Maeno. Low temperature specific heat capacity of $\text{Dy}_2\text{Ti}_2\text{O}_7$ in the Kagomé ice state. *Journal of the Physical Society of Japan*, 73(10), 2004.
- [69] A. Suter and B.M. Wojek. Musrfit: A free platform-independent framework for sr data analysis. *Physics Procedia*, 30(69), 2012.
- [70] Cole Mauws, Nathaniel Hiebert, Megan Rutherford, Haidong D. Zhou, Qing Huang, Matther B. Stone, Nicholas P. Butch, Yixi Su, Eun Sang Choi, Zahra Yamani, and Christopher Wiebe. Magnetic ordering in the Ising antiferromagnetic pyrochlore $\text{Nd}_2\text{ScNbO}_7$. unpublished, June 2019.

- [71] C. Mauws, J. Beare, M. R. Rutherford, Y. Su, S. Sharma, M. Nugent, M. K. Lee, L. J. Chang, S. R. Dunsiger, J. S. Gardener, G. M. Luke, and C. R. Wiebe. Palmer-chalker cooperative paramagnetic state in the $\text{Gd}_2\text{ScNbO}_7$ pyrochlore. unpublished, May 2021.
- [72] D. Pomaranski, L. R. Yaraskavitch, S. Meng, K. A. Ross, H. M. L. Noad, H. A. Dabkowska, B. D. Gaulin, and J. B. Kycia. Absence of Pauling’s residual entropy in thermally equilibrated $\text{Dy}_2\text{Ti}_2\text{O}_7$. *Nature Physics*, 9(353-356), 2013.
- [73] Cole Mauws. *Frustrated Magnetism in Charge Disordered $\text{Ln}_2\text{ScNbO}_7$ Pyrochlores*. PhD thesis, University of Manitoba, 2021.
- [74] Varley F. Sears. Neutron scattering lengths and cross sections. *Neutron News*, 3(3):26–37, 1992.
- [75] Roger Pynn. *An Introduction to Neutron Scattering*, chapter 2. Springer.
- [76] M Ruminy, E Pomjakushina, K Iida, K Kamazawa, D T Androja, U Stuhr, and T Fennell. Crystal field parameters of the rare earth pyrochlores $\text{r}_2\text{ti}_2\text{o}_7$ (r = tb, dy, ho). *Physical Review B*, 94(024430), 2016.